Data Analysis for the Reaction $^{14}\mathrm{N}(\alpha, p)$ in TACTIC and Details about a Specific Isotope

Mohamad Kourmo

MSc by Research

University of York

School of Physics, Engineering and Technology

February 2026

Abstract

Recently, gaseous detectors have played a crucial role in astrophysics, particularly in laboratory-based experiments that simulate nuclear reactions occurring in stars. Detecting protons and α particles helps improve our understanding of stellar nucleosynthesis, the process responsible for the formation of chemical elements in the universe. In this research, a ^{14}N beam was directed onto a ^{4}He target gas, enabling direct measurements of the nuclear reaction. This approach allowed for particle identification and provided valuable insights into the production of specific isotopes.

These measurements provide important constraints on nucleosynthesis processes and reaction cross sections relevant to the formation of elements in stars and supernovae. The experiment was carried out using the TRIUMF Annular Chamber for Tracking and Identification of Charged Particles (TACTIC), which is specifically designed to study α-induced charged-particle reactions at low center-of-mass energies. The measurements were based on detecting and identifying charged particles through their energy-loss patterns in the detector gas, enabling the analysis of reaction products over a broad energy range.

High beam intensities ($> 10^6$ pps) and charged-particle detection techniques were employed to determine the reaction yield, cross section, and center-of-mass energies at low energies. The experimental data obtained from the $^{14}\mathrm{N} + {}^{4}\mathrm{He}$ reaction were analyzed, and the resulting cross sections were compared with those reported in previous experimental studies of similar reactions.

Keywords: Gas detector, ^{14}N–He–CO_2 gas mixture, cross section, low energy.

To my parents and Loran, Arman, Louvian

Acknowledgements

In the beginning, I would like to state that all the work presented in this thesis was carried out by myself, with invaluable input, support, and scientific insight from the Astrophysics Group. Their dedication to science and their willingness to share knowledge greatly enriched the quality of this research.

I would like to express my deepest gratitude and appreciation to my supervisor, Prof. Alison Laird, who believed in my potential and generously offered me the opportunity to pursue this project under her supervision. Her guidance, encouragement, and expertise have been essential throughout every stage of this work. Without her support, this thesis could not have been completed, and I would not have been able to achieve the progress and accomplishments reflected here.

I am also sincerely thankful for her understanding of the health and family challenges I faced during this journey. Her patience and compassion made it possible for me to continue my work despite the difficulties.

My appreciation extends to the members of the nuclear physics group and my colleagues in the office for their support, discussions, and collaboration. The environment they fostered made this work both challenging and rewarding.

I am profoundly grateful to my children (Loran, Arman, and Louvain), who were always eager to see the latest updates and often wished to talk to Alison out of curiosity. Their unwavering encouragement and belief in me, along with their joy and kindness, have been a constant source of strength and motivation.

Last but not least, I would like to acknowledge everyone who, in ways large or small, contributed to the completion of this thesis.

Declaration of Authorship

I declare that this thesis is a presentation of original work and I am the sole author. This work has not previously been presented for a degree or other qualification at this University or elsewhere. All sources are acknowledged as references.

Contents

List of Figures

List of Tables

Chapter 1

Nuclear Reactions

1.1 Introduction

Nuclear astrophysics is the study of the processes that synthesize elements. This research project aims to provide information on the production of specific isotopes which can provide crucial constraints on these processes, synthesizing the elements inside stars and supernovae. Simulations and measurements were performed to optimize experimental configurations for such studies. In this thesis, five chapters are presented to provide an overview of the background, methodology, and results of this research. In chapter one, 'introduction,' we provide a background of the previous studies and some main nuclear reactions, transmission through the barrier, which will help us to understand the following steps. In the chapter two "Gas Detectors", explains the main steps and the target of employing those detectors in kind of such studies.

In Chapter 3, the geometry and operating principles of the TACTIC detector and their role in this study are described. Additional details of the simulation have been included to provide a more comprehensive description of the TACTIC detector and to give a clearer overall picture of the experimental setup. Chapter 4 presents the results of the analysis, including particle identification, cross-section measurements, and centre-of-mass energy reconstruction.

In the final chapter, "Conclusion," we compare our results and present our perspective on possible improvements to this subject.

1.1.1 Nuclear Reaction

A nuclear reaction can happen when a charged particle from the accelerator or even radioactive source collides with bulk matter. The first nuclear reaction observed by Rutherford in which a charged particle induced a nuclear transformation as shown in this reaction in 1919 [1]:

$$\alpha + {}^{14}\mathrm{N} \rightarrow {}^{17}\mathrm{O} + p \tag{1.1}$$

in a different way the above reaction can be written as

$$^{14}\mathrm{N}(\alpha, \mathrm{p})^{17}\mathrm{O} \tag{1.2}$$

This way is more convenient because it provides a natural way to describe a broad category of reactions that share common characteristics. Generally, the equation 1.2 can be written as

X(a,b)Y and then we can observe some properties: If the outgoing particle is of the same species as the target particle, the reaction is classified as scattering. The process is elastic if both the projectile and the target remain in their ground states after the interaction, and inelastic if one or more of the particles is left in an excited state.

1.1.2 Energetics of Nuclear Reactions:

For the charged particles and elements in the reaction, the outcome reaction has different masses with respect to the recoils and ejectile, In nuclear reactions, total energy rest mass and kinetic energy are conserved and written as:

$$m_x c^2 + T_x + m_a c^2 + T_a = m_Y c^2 + T_Y + m_b c^2 + T_b \tag{1.3}$$

Where T is the kinetic energy, m is the rest masses. The Q value which defined as a radioactive decay involved in the equation (1.3) and can be expressed in several ways depending on mass

$$Q = (m_{\text{initial}} - m_{\text{final}})c^2 \tag{1.4}$$

or depend on kinetic energy

$$Q = T_{\text{final}} - T_{\text{initial}} \tag{1.5}$$

The Q value could have three probabilities,

1- If $Q > 0$, when $m_{\text{initial}} > m_{\text{final}}$, the reaction is called *exoergic*.

2- If $Q < 0$, when the $m_{\text{initial}} < m_{\text{final}}$ the reaction called endoergic. In this case the initial kinetic energy converted into nuclear masses or binding energy.

3- Or $Q = 0$

As is clear, the Q value depends on the nuclear masses. However, the direct determination of nuclear masses is challenging because experimental measurements typically yield atomic masses, which include the effects of the bound electrons. However, the atomic masses can be calculated from this formula:

$$m_a(A,Z) = m_{\text{nuc}}(A,Z) + Zm_e - B_e(Z) \tag{1.6}$$

Where m_e is the electron mass and B_e is the binding energy in the atom. While the electron binding energy is much smaller than the nuclear mass differences, its contribution can be neglected. On the other hand, while nuclear reactions conserve total charge, atomic masses can be used in place of nuclear masses because the same number of electron rest masses is present on both sides of the reaction equation. In this case, the mass excess can be expressed as:

$$\Delta E \equiv (m_a - Am_u)c^2 \tag{1.7}$$

Where A is the mass number of the total atom, and m_u is the atomic mass unit u.

1.1.3 Reaction cross section:

Cross section σ is the probability of the reaction in nuclear physics to take place. Typically, in experimental nuclear physics, if the incident beam energy I_b with an areal density I_t/A suggesting that the target is larger than the beam area see Fig 1.1, then the reaction cross section could be defined as :

$$\sigma = \frac{\frac{I_r}{t}}{\left(\frac{I_b}{t}\right)\left(\frac{I_t}{A}\right)} \tag{1.8}$$

where $\frac{I_r}{t}$ defined as a number of reactions per unit time, or defined as reaction yield (Y) per unit time. The differential cross section can be expressed as:

$$\frac{d\sigma}{d\Omega} = \frac{\frac{I_r}{t}}{\left(\frac{I_b}{t}\right)\left(\frac{I_t}{A}\right)} \cdot \frac{1}{\Delta\Omega} \tag{1.9}$$

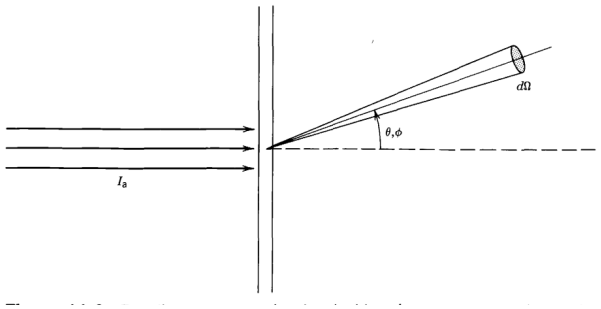

Figure 1.1: Reaction geometry showing incident beam, target, and outgoing beam. [1]

The $\frac{d\sigma}{d\Omega}$ is identified as the differential cross section, and its calculation provides essential information about the angular distribution of the reaction products. In our calculation, we do not use the differential cross section but rather the total cross section. Therefore, in this case we must replace $d\Omega = \sin\theta\, d\theta\, d\phi$. The final form of the cross section can then be written as:

$$\sigma = \int \frac{d\sigma}{d\Omega} d\Omega \tag{1.10}$$

1.1.4 Elastic scattering

When a beam interacts with a target, two broad categories of processes can occur: **elastic** and **inelastic scattering**, both of which may be detected depending on the experimental setup. At higher energies the situation can become more complex, as additional reaction channels may open, producing secondary particles.

This section focuses on **elastic scattering**, which is a fundamental nuclear process in which two nuclei interact and deflect each other without altering their internal structure. Both kinetic energy and momentum are conserved.

In experiments involving the reaction ^{14}N + α, discussed in more detail later, the reaction products retain their identities, and the scattering angles together with the associated energy-loss patterns provide information about the underlying nuclear potential and interaction dynamics. Within the TACTIC Time Projection Chamber (TPC), elastic α^+ ^{14}N scattering is identified through the characteristic ionization tracks created by the recoiling nitrogen nucleus and the

outgoing alpha particle. Their energy deposition (ΔE) and total kinetic energy (E) follow well-defined kinematic correlations.

Precise measurement of these tracks—both spatially and energetically—enables accurate reconstruction of the scattering kinematics. This makes elastic scattering an essential calibration tool for the detector, as well as a valuable probe of nuclear structure and reaction mechanisms relevant to astrophysical processes.

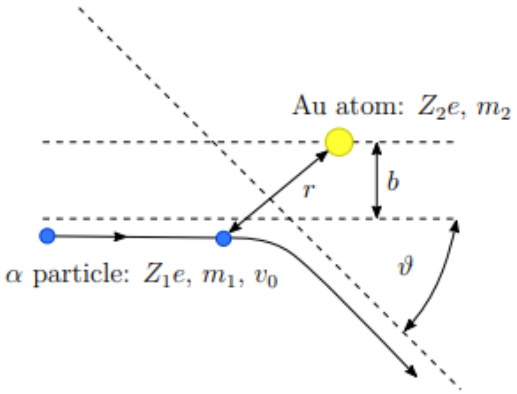

Figure 1.2: The figure shows the elastic scattering for the Rutherford experiment. [2]

Let us consider an α particle with mass m_1 and charge Z_1e ($Z_1 = 2$), moving with velocity v_0 and kinetic energy E_0, toward a target nucleus Au [2] with mass m_2 and charge Z_2e ($Z_2 = 79$). The potential can then be expressed as:

$$V(r) = \frac{Z_1 Z_2 e^2}{4\pi\varepsilon_0}\frac{1}{r} = \frac{Z_1 Z_2 \xi^2}{r} \tag{1.11}$$

where

$$\xi^2 = \frac{e^2}{4\pi\varepsilon_0} = 1.44\,\mathrm{eV\,nm} \tag{1.12}$$

In repulsive Coulomb potential, the α particle is considered to follow a hyperbolic orbit [11]. Then, the scattering angle is given by the following relation :

$$\tan\left(\frac{\vartheta}{2}\right) = \frac{Z_1 Z_2\,\xi^2}{m_1 v_0^2 b} = \frac{Z_1 Z_2\,\xi^2}{2E_0\,b}. \tag{1.13}$$

where the parameter b determines the associated scattering angle ϑ . The α transfer energy to the Au nucleus during the interaction as shown in figure 1.2 and called E_1 and can be calculated from the conservation laws of energy and momentum [12].

1.1.5 Astrophysical Reaction Rates

Astrophysical reaction rates are a key ingredient in models of stellar nucleosynthesis and energy generation [13]. They describe the frequency of nuclear reactions in a stellar plasma and are obtained by folding nuclear reaction cross sections with the Maxwell–Boltzmann energy distribution (1.14) of interacting particles. Since these reactions occur at very low energies,

often below the Coulomb barrier, both experimental measurements and theoretical predictions are particularly demanding.

$$r \propto \frac{1}{T^{3/2}} \int_0^\infty \sigma(E)\, E\, e^{-E/(kT)}\, dE \tag{1.14}$$

In stellar environments, only a narrow range of interaction energies contributes significantly to a given reaction rate. This energy range, commonly referred to as the Gamow window [14, 15], results from the competition between the thermal particle distribution and the energy dependence of the nuclear cross section. Although simple approximation formulas for the Gamow window are widely used, they are not always reliable, especially for intermediate and heavy nuclei. In such cases, the relevant energy range can shift by several MeV, which has important consequences for experimental strategies and theoretical extrapolations.

Most astrophysically relevant nuclear reactions proceed via the formation of a compound nucleus. When the nuclear level density at the compound formation energy is high, the reaction can be treated statistically using the Hauser–Feshbach model. In this approach, the cross section depends on averaged transmission coefficients (1.15) that are related to the particle and gamma decay widths of the compound nucleus. The cross section is given by an incoherent sum over resonant intermediate states. Each resonance contributes according to its spin degeneracy and its coupling strength to the entrance channel a and the exit channel b, with the contribution normalized by the total decay width of the resonance. This reflects the probability for the system to be formed in a given resonant state and subsequently decay into the specified final channel.However, when the level density is low, individual resonances or non–statistical mechanisms become important, and the statistical model may overestimate reaction probabilities.

$$\sigma \propto \sum_n (2J_n + 1)\, \frac{\Gamma'_{a,n}\, \Gamma_{b,n}}{\Gamma_{\mathrm{tot},n}} \tag{1.15}$$

The sensitivity of reaction cross sections to nuclear input parameters is strongly energy dependent. In many situations, the smallest width involved in the reaction governs both the energy dependence of the cross section and its sensitivity to nuclear properties. Sensitivity studies therefore provide valuable guidance for identifying which measurements are most relevant for constraining astrophysical reaction rates.

Stellar reaction rates differ from laboratory rates because nuclei in stars are thermally excited [14, 16]. These stellar enhancement effects can be substantial, particularly for photodisintegration reactions [17, 18], where transitions from excited states dominate the stellar rate. As a result, laboratory measurements often represent only a small fraction of the true stellar reaction rate. Capture reactions with positive Q-values are therefore generally preferred for experimental studies, as they are closer to the stellar conditions and allow the use of detailed balance to infer inverse reaction rates.

For nuclei far from stability, especially those with low particle separation energies, direct reaction mechanisms such as direct capture can contribute significantly to the total reaction rate. Although direct capture cross sections are difficult to predict due to uncertainties in nuclear structure, averaged models have been developed to provide more robust estimates. Modern reaction codes combine modified statistical models with direct reaction contributions, leading to improved predictions for astrophysical applications.

In conclusion, the determination of reliable astrophysical reaction rates requires a careful combination of experimental data and theoretical modelling. A detailed understanding of

relevant energy ranges, reaction mechanisms, and stellar effects is essential for accurate nucleosynthesis calculations and for interpreting observations of stellar and explosive astrophysical environments.

Chapter 2

Gaseous Detectors

In the last few decades, gas detectors have played an essential role in high-energy and nuclear physics experiments, while the main idea began with Rutherford and Geiger [19]. The operation of gaseous detectors depends on the effects resulting from the passage of a charged particle through a gas. As the particle moves, it primarily induces ionization and excitation of gas molecules along its path. The electron-ion pairs produced in the gas simultaneously form the detector's electrical signal.

The gaseous counter concept existed in the form of a cylindrical tube filled with gas (or a gas mixture) at a certain pressure. It had a thin wire of about 0.45 mm diameter stretched along its axis. A negative voltage was then applied to achieve gas amplification of several thousand. At the time, alpha particles were detected as sparks — the first spark detector for these particles. Later, Geiger modified his setup to use a pinhead source, which enabled him to count electrons by substituting the anode wire [20]

The development of the Geiger–Müller [21] counter in 1928 resulted in stronger pulses that were not exclusively dependent on primary ionization. This was accomplished by preventing continuous discharge with high-value resistors of around $10^8\,\Omega$, which led to a dead time of about 10^{-4} seconds. When Tuve supplemented the working gas with alcohol in 1935, he achieved a noteworthy breakthrough by suppressing internal gas discharges. This method was particularly useful in cosmic radiation physics because it made it possible to employ lower load resistances, which in turn allowed for faster pulse rates.

In 1968, Charpak [4] invented the proportional ionization chamber, which was eventually transformed into a drift chamber [22, 23], marking the beginning of the practical development of gaseous detectors. Advances in electronics, especially in radiation resistance, cost reduction, and miniaturization, were responsible for this change and subsequent improvements. Regarding simulation programs such as Garfield++ [24] and [25], they have been essential in improving our understanding of detector mechanisms and achieving better results.

2.0.1 Operating Regions of Gaseous Detectors

The simple idea depends on when charged particles travel through the gas, they form pairs of electrons and ions along their path. These electrons are attracted to positively charged electrodes, where they usually undergo avalanche amplification. Below is a brief overview of the various aspects of ionization, following some established approaches. The figure 2.1 shows the region of the operation, where electrons and ions are driven toward their respective col-

lection electrodes by the detector's internal electric field. The field is insufficiently strong to prevent the recombination of electron-ion pairs when the applied voltage is low. By lowering recombination, raising the voltage eventually results in the ion saturation region, where all the ions are gathered. The voltage eventually reaches the threshold where gas multiplication begins as it keeps rising. After this, the accumulated charge is amplified, producing a greater pulse amplitude. This multiplication is linear within a specific range of electric field strength, which means that the collected charge is exactly proportional to the initial number of ion pairs created by the incoming radiation. The operational mode of standard proportional counters is defined by this linear response range, where the collected charge is proportional to the number of initial ion pairs. Non-linear effects start to show up if the voltage rises above this threshold. The limited proportionality region results from the electric field being distorted by the accumulation of slowly moving positive ions. This space charge effect takes over as the voltage rises, interfering with gas multiplication and resulting in the total loss of information about the initial ion pairs. The Geiger-Mueller region of operation begins at this point.

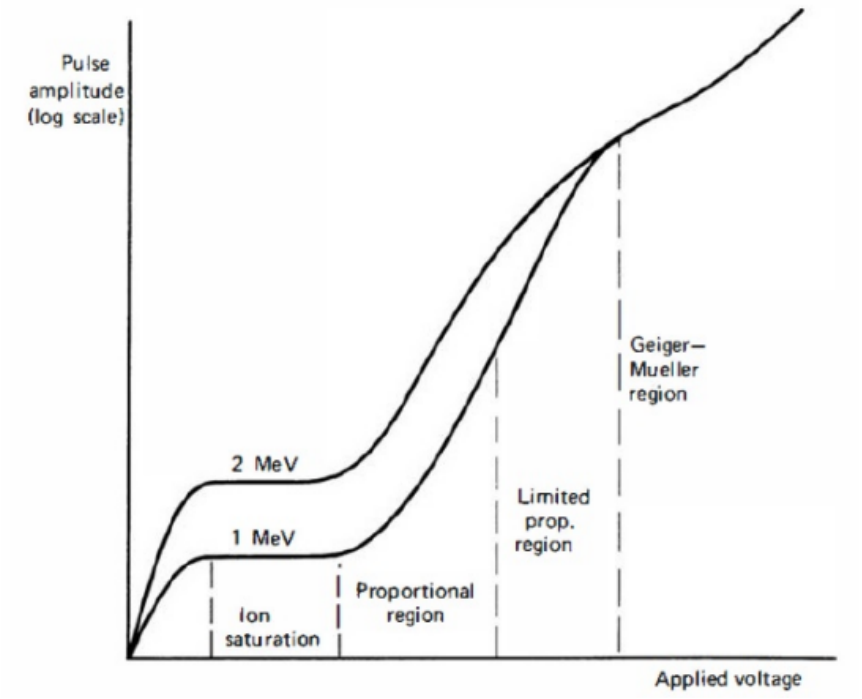

Figure 2.1: The different regions of operation of gas-filled detectors. The observed pulse amplitude is plotted for events depositing two different amounts of energy within the gas. [3]

2.0.2 Diffusion, Charge Transfer, and Recombination

The atoms, molecules, and positive ions move along free paths under the conditions of constant thermal motion 2.2, typically on the order of 10^{-6}–10^{-8} m. Free electrons and positive ions in a gas diffuse from high-density regions due to thermal motion, with electrons diffusing more rapidly because of their higher thermal velocity. A cluster of free electrons spreads out over time following a Gaussian distribution. Let σ denote the standard deviation, which can be expressed as

$$\sigma = \sqrt{Dt} \tag{2.1}$$

Where D is the diffusion coefficient and can be predicted from kinetic gas theory. In gas mixtures, charge transfer occurs when ions swap electrons with neutral molecules, with the positive charge favoring species that have the lowest ionization energy. Free electrons can attach to neutral molecules in some gases, forming negative ions. Oxygen easily forms negative ions, while gases like nitrogen and noble gases allow electrons to remain free. Positive ions recombine with free electrons or negative ions, neutralizing their charge and reducing the detectable ionization signal.

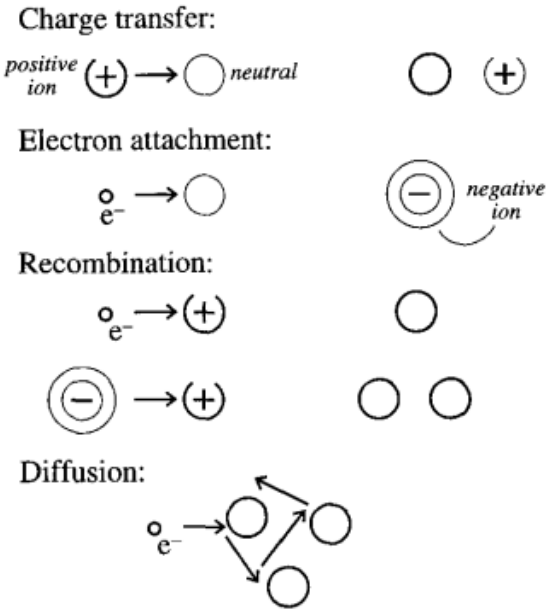

Figure 2.2: Process of interactions of charged species in a gas that can influence the behavior of gas-filled detectors. [3]

Because the collision frequency is proportional to the product of the particle densities, the recombination rate can be written as:

$$\frac{dn^+}{dt} = \frac{dn^-}{dt} = -\alpha n^+ n^- \tag{2.2}$$

where

$$\begin{aligned} n^+ &= \text{number density of positive species,} \\ n^- &= \text{number density of negative species,} \\ \alpha &= \text{recombination coefficient.} \end{aligned}$$

Recombination between positive and negative ions is much more frequent than between positive ions and free electrons, especially in gases that easily form negative ions.

2.0.3 W- Value

The output of the detector depends on both the distribution of ionization and the total amount of ionization produced. As a charged particle traverses the gas, it loses energy primarily through ionization, creating electron–ion pairs that form the basis of the detector signal. However, energy can also be lost through another mechanism, known as the excitation process, in which an electron is promoted to a higher energy level. The W-value is defined as the average energy required to produce a single electron–ion pair in a gas. This value is greater than the ionization energy because not all of the incident particle's energy is used for ionization; a portion is also consumed in excitation and other non-ionizing interactions within the gas. Table 2.1 shows the various W-values calculated using Garfield.

Table 2.1: First ionization potentials and W-values of various gases and gas mixtures. Gas mixture percentages mentioned are by mass. [10]

Gas	First ionisation potential (eV)	W-value (eV)
Ar	15.7	26.3
He	24.5	42.7
CO_2	13.7	33.0
CH_4	15.2	28.0
i-C_4H_{10}	10.6	23.0
Air	–	35.1
Ar:CH_4 90:10	–	26.5
He:CO_2 90:10	–	39.2
He:CO_2 97:3	–	42.5

2.0.4 Energy loss with the Bethe formula

When a charged particle enters a gas or gas mixture, it loses energy while traversing the medium. This energy loss can be described by the Bethe formula, as shown below:

$$-\frac{dE}{dX} = \frac{4\pi e^4 z^2}{m_0 v^2} NB \tag{2.3}$$

$$B = Z\left[\ln\frac{2m_0v^2}{I} + \ln\left(1-\frac{v^2}{c^2}\right) - \frac{v^2}{c^2}\right] \tag{2.4}$$

where:

- v is the velocity of the ion,
- ze is the charge of the ion,
- N is the number density of the absorber atoms,
- Z is the atomic number of the absorber atoms,
- m_0 is the electron rest mass,

- e is the electronic charge,
- I is the mean excitation potential of the absorber,
- c is the speed of light.

I is the average excitation and ionization potential of the absorber. At lower energies ($<$ 10 keV), the Bethe equation is no longer applicable because the assumptions used in its derivation are no longer valid. In this energy region, the energy loss is dominated by two mechanisms: electronic stopping and nuclear stopping.

In the case of mixed gases, as will be discussed later, if the stopping powers of the individual elements are known, Bragg's rule suggests that the total stopping power of the mixture can be approximated by summing the constituent stopping powers weighted by their stoichiometric ratios [26]. However, the accuracy of this approximation may be affected by molecular bonding within the mixed gases.

Ziegler and Manoyan [27] have developed simulation software that helps to better understand the interactions between ions and matter.

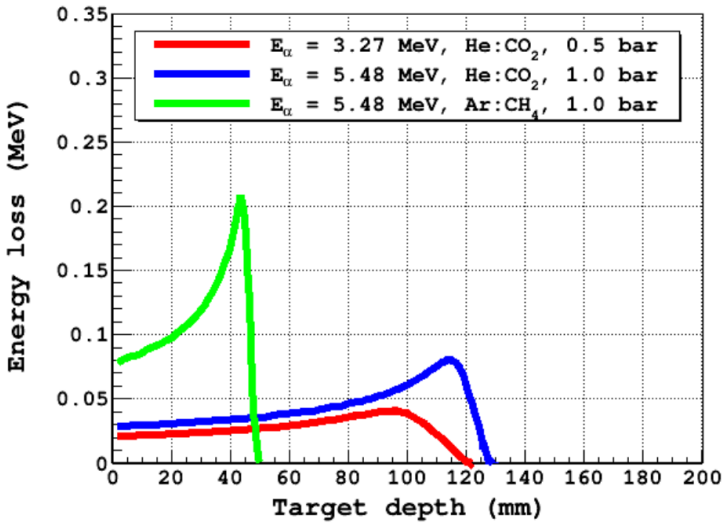

Figure 2.3: The figure shows the energy loss versus depth (or range) curves for 3.27 MeV and 5.48 MeV α particles in He:CO_2 (90:10) and Ar:CH_4 (90:10) gas mixtures, calculated using SRIM. [4]

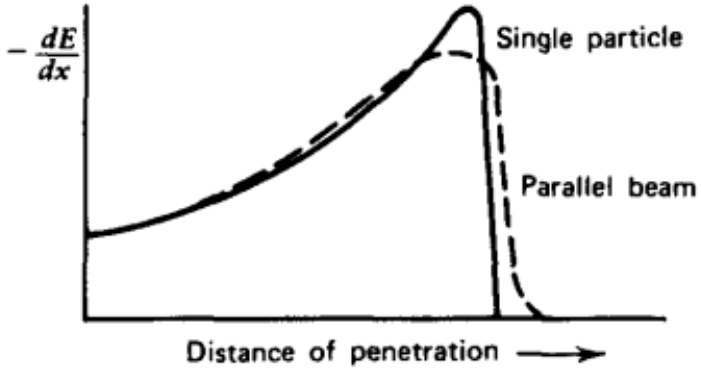

Figure 2.4: These curves exhibit a characteristic pattern: a relatively flat plateau followed by a peak in energy loss—the Bragg peak—after which the energy loss rapidly decreases because after the Bragg peak, the charged particle has lost almost all of its kinetic energy and eventually comes to a stop. Since it can no longer continue through the material or produce further ionization, the amount of energy deposited per unit distance falls rapidly to zero. The figure shows the Bragg peak for single and parallel beams, illustrating how the energy loss behaves in each case.

2.0.5 Movement of Electrons and Ions

Drift Velocities

In a gas subjected to a uniform electric field, electrons and ions drift while colliding with gas molecules, eventually reaching a constant drift velocity u that is much lower than their instantaneous velocity c between collisions. Electrons and ions behave differently due to their mass difference.

Rather than having a single velocity c, particles exhibit a distribution of velocities, determined by how the collision cross-section and energy loss depend on speed. At low velocities, elastic scattering dominates, whereas at higher velocities, inelastic collisions also contribute. These interactions are often characterized by an effective cross-section $\sigma(c)$ and an average energy loss per collision $\varepsilon(c)$, both of which vary with velocity.

In some cases, collision cross-sections σ have been measured directly. However, more commonly, both σ and the average energy loss $\varepsilon(c)$ must be inferred from measurements of the drift velocity $u(E)$—that is, how the drift velocity varies with the electric field E—as well as from diffusion data, using certain assumptions about the excitation behavior during collisions.

Drift of Electrons

Due to their low mass, electrons scatter in all directions during collisions [28]. Their drift velocity u is determined by the acceleration eE/m multiplied by the average time τ between successive collisions.

$$u = \frac{eE\tau}{m} \tag{2.5}$$

While charged particles move over the drift distance, they gain and lose energy due to collisions. The concept of mobility, denoted by μ, refers to the balance between this energy gain

and loss.

$$\frac{x}{u} \cdot \frac{1}{\mu} \Delta\varepsilon E = eEx \tag{2.6}$$

Here, ε_E is the energy gained between collisions. Δ is the average fraction of energy lost in a collision. $\frac{x}{u} \cdot \frac{1}{\mu}$ is the number of collisions over a distance x.

Then, the total energy ε of the electron is given by

$$\frac{m}{2}c^2 = \varepsilon = \varepsilon_E + \frac{3}{2}kT \tag{2.7}$$

Here, $\frac{3}{2}kT$ represents the thermal energy. For gas mixtures with number densities n_i ($N = \sum_i n_i$), the effective σ and ε are given by

$$\sigma = \frac{\sum_i n_i \sigma_i}{N} \tag{2.8}$$

$$\Delta\sigma = \frac{\sum_i n_i \sigma_i \Delta_i}{N} \tag{2.9}$$

At low electric fields E, drift velocities increase with the field. For some gases (e.g., CH_4 and Ar–CH_4 mixtures), the drift velocity reaches a maximum, then decreases, and may increase again at higher fields.

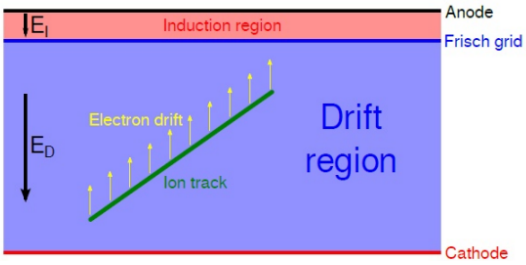

Figure 2.5: Schematic diagram of a basic TPC. Ionization electrons in the drift region move toward the signal anode under the influence of the drift field E_D. In the induction region, their movement is governed by the induction field E_I. [5]

Drift time

The primary sources of error in determining the drift time are electronic noise, electron clustering, δ-ray production, and diffusion effects. Electronic noise introduces a consistent level of error. Close to the anode wire, the grouping of primary charges significantly increases the error. Further from the anode, diffusion becomes more influential, with its contribution to the error increasing proportionally to the square root of the distance. Figure 2.5 shows an example of the drift time for a stable beam of in a gas mixture and how electron drift toward to hit the μ-RWELL .

Ion-Pair production

When a charged particle passes through the gas target the trail of the electron-ion pair produced as a form of ionization. The free electrons drift toward positively biased electrodes, where they are topically multiplied through an avalanche process. [29]

Chapter 3

TACTIC

TRIUMF is Canada's particle accelerator centre which was established in Vancouver Canada in 1986 and operates as one of the leading physics laboratories in the world [30],TACTIC is part of this Canadian particle accelerator centre . The figure 3.1 shows the technical drawing of ISAC I experimental hall where OLIS (an off-line ion source)supplies beams from stable isotopes to various experiments. The ISAC II experimental hall is not shown in the picture. During the in-beam experiments, TACTIC was positioned at the HEBT3 beam line in place of TUDA [5].

TACTIC is an active target time-projection chamber with radial field geometry [31, 6, 32, 14, 33]. the Geant4 geometry for the TACTIC's shape shows 3.3 the main parts of the detector. Tactic has constructed to let the beam passes into the free gas target thought the window (which is basically aluminised Mylar) and located at the upstream end.

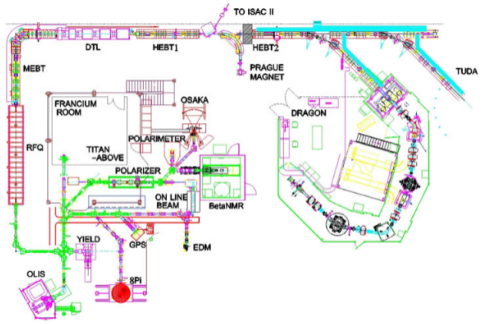

Figure 3.1: Model Technical drawing of ISAC I experimental hall where OLIS supplies beams from stable isotopes to various experiments. The ISAC II experimental hall is not shown in the picture. During the in-beam experiments, TACTIC was positioned at the HEBT3 beamline in place of TUDA [6].

A simulation for this experiment have been done as a part of the comparison study to obtain a detailed understanding of the detector performance and particle identification see figure 3.2. The simulation section done by Julien Bordes [7]

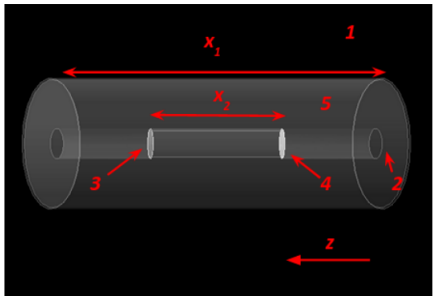

(a) The previous Geant4 of TACTIC

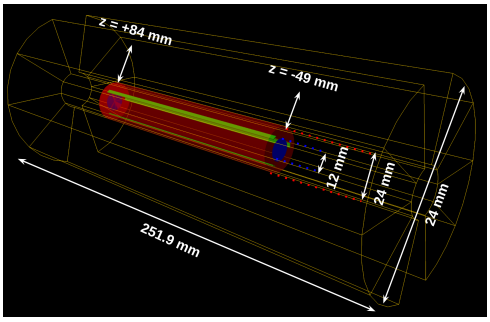

(b) The new Geant4 of TACTIC

Figure 3.2: Comparison between (a) the previous and (b) the new Geant4 geometry of TACTIC and corresponding simulation results. The Geant4 geometry consists of: (1) vacuum region, (2) hole with circular cross-section in the cylinder between the window and vacuum region, (3) and (4) exit and entrance windows, (5) gas-filled copper cylinder. X_1 denotes the length of the detection region, and X_2 denotes the length of the target region. [7, 5]

3.0.1 Operation of the TACTIC Detector

The figure 3.3illustrates the reaction and detection regions of the system. The gas in Region 6, which serves as the target gas, can be controlled in both length and thickness by adjusting the window position indicated as number 4. When the beam passes through the target gas, nuclear interactions take place, producing new particles and nuclei, including recoils and ejectiles. These reaction products escape from the target region and enter the detection region (the yellow region, labeled as number 2) through the cathode cage assembly. In this region, the particles can be tracked and identified. The reaction occurs within the region 6 (the field-free target) area and located in the cathode cage. The resulting particles and nuclei exit through the cathode and ionize the gas active detection region, then the generated ionization electrons drift outward radially due to electric field application to the μ-RWELL which serves as the readout and charge-amplification structure of the detector. In this region, the electrons undergo avalanche multiplication, allowing the signals to be collected and the particles to be identified. The field ring beyond the active region maintain a highly uniform electric field within it, and this study was done by Kirchner [5]. The drifted and multiplied electrons hold enough information (amplitude, time, energy...) as signal to the anode pads which show as black dashed in the figure 3.3. For the TACTIC the deposited energy into the pads by the charged particles and can exhibit a wide range of energies various from KeV to a few MeV. The drifted electrons are responsible to generate the signals at the anode pads, which are then amplified by charge sensitive preamplifier

and sent to the data acquisition system for recording and further analysis.

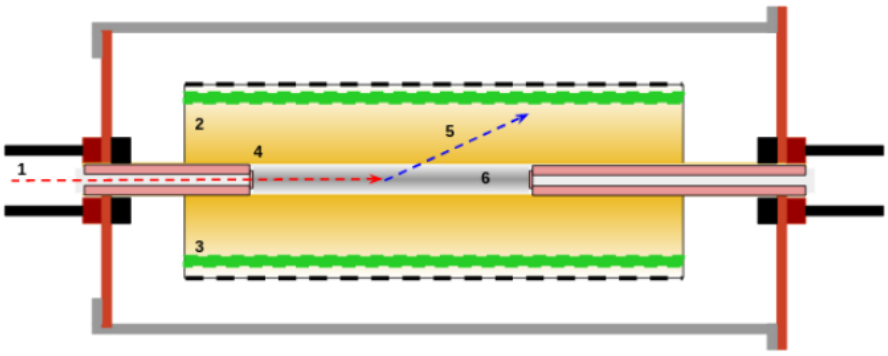

Figure 3.3: Diagram of TACTIC. The identified regions are: 1- ion beam, 2- detection region, 3- μ-RWELL, 4- entrance window, 5- scattered products, 6- target region. The two important parts of the TACTIC are cathode cage and μ-RWELL which play an essential role in electron drift electrons [5]

3.0.2 Cathode Cage

To prevent ionization electrons produced in the beam region from entering the drift region and disturbing the uniform drift field, the target area was shielded using two concentric, annular arrays of 32 gold-plated tungsten wires, each with a thickness of approximately 20 μm. These wires extend along the full length of the detection region, parallel to the central beam axis.

The inner set of wires acts as an electron cage, while the outer set helps establish the drift field in conjunction with the μ-RWELL. The two wire arrays are connected through a resistor, ensuring that the inner wires are held at a slightly higher positive potential than the outer ones. This configuration creates a potential gradient that effectively confines the electrons ionized by the beam within the target region, preventing them from entering the drift volume.

The cathode cage assembly was designed to enable TACTIC to operate under high beam intensities by suppressing beam-induced ionization. However, this design also causes the initial segment of the ion track—including the interaction vertex—to be undetectable within the target region. Consequently, the measured energy corresponds only to a fraction of the ion's total energy. The amount of undetected energy depends on the ion's track angle, track length, and its energy-loss rate ($\mathrm{d}E/\mathrm{d}x$).

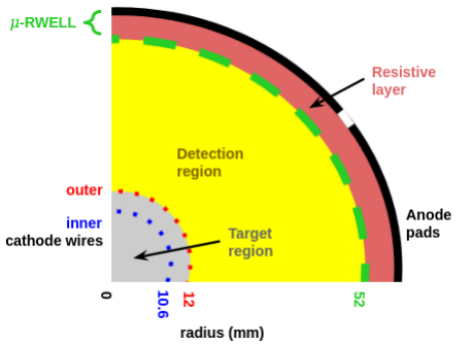

Figure 3.4: The cross section for TACTIC and cathode cage assembly [5, 8]

3.0.3 µ-RWELL

In TACTIC, the μ-RWELL structures were built using thin, flexible PCB boards capable of bending to a radius of approximately 50 mm. During assembly, two μ-RWELL structures were curved into a semi-cylindrical shape to match TACTIC's cylindrical geometry. Each structure featured 240 segmented copper anode pads arranged in 4 rows of 60 pads on the readout PCB, covering an active area of 139.0×251.9 mm^2 and incorporating a resistive layer with a sheet resistance of about 45 M$\Omega/\square$. The anode pads measured 4.1×34.7 mm with a 0.1 mm pitch. Altogether, the TACTIC readout comprises 480 anode pads organized into 8 rows (sectors), each containing 60 pads and labelled from 0 to 7 (see figure 3.5). Each sector is split into upstream and downstream regions relative to the beam direction. The anode pads are connected to the readout PCBs using standard 30-core flat flexible cables (FFC) with a 0.5 mm pitch [31].

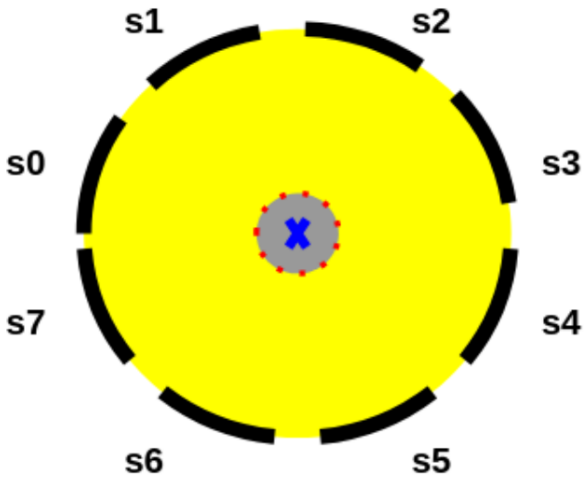

Figure 3.5: Schematic diagram of TACTIC cross section: each black segment of the outer boundary represents a sector. There are finite gaps between two consecutive sectors. The red dotted line and the blue cross in the middle represents the outer cathode wires and the beam axis, respectively. Eight sectors are divided among the two halves of TACTIC, i.e., group 1: s6, s7, s0, s1 and group 2: s2, s3, s4, s5

3.0.4 Detector's dimensions and acceptance region

Inside TACTIC, the tracking of charged particles is constrained by the size of the detection area. The detection area in a z-direction is limited by the width and pitch of 60 pads for each sector.

$$-126\,\text{mm} \leq z \leq 126\,\text{mm}$$

The limits of the detection region are defined by the outer cathode cages and the μ-RWELL boundaries, while the inner cathode boundaries are less clearly defined and vary with the horizontal angle θ

$$12\,\text{mm} \lesssim r \lesssim 50\,\text{mm}$$

The outer radius of the cathode cage was selected to be approximately 12 mm to prevent most of the beam from entering the detection region. The geometry of the detectable region determines the upstream (l_{us}), downstream (l_{ds}), and radial (l_{r}) dimensions, as shown in the following equations:

$$l_{\text{us}} = \frac{d}{2} + \frac{z_0}{\cos(180^\circ - \theta)}, \tag{3.1}$$

$$l_{\text{ds}} = \frac{d}{2} - \frac{z_0}{\cos\theta}, \tag{3.2}$$

$$l_{\text{r}} = \frac{r_{\text{max}}}{\sin\theta}. \tag{3.3}$$

The maximum radius is $r_{\text{max}} = 50\,\text{mm}$, the total length of the detection region along the z-axis is $d = 252\,\text{mm}$, and z_0 represents the vertex position relative to the center of the detection region.

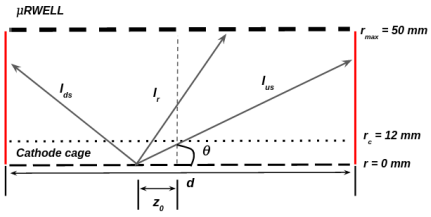

Figure 3.6: Geometric limitations to detectable track lengths in TACTIC:the maximum detectable track lengths are defined by the outer boundaries of the drift region (red solid lines) and the μ-RWELL. [5]

3.0.5 Physics Tools

Raw data were supplied by the experimental team at TRIUMF, Canada. The experiment was completed in November 2022 by Soham Chakraborty [5]. In this work, GEANT4 has been used to simulate the reaction in TACTIC. Although GEANT4 is typically used for high-energy physics, its accuracy decreases for low-energy reactions because these processes are strongly affected by nuclear structure details, resonance effects, and the limited availability of low-energy cross-section data.

On the other hand, NPTOOLS is an open-source framework designed for data analysis and Monte Carlo simulations in low-energy nuclear physics, mainly for radioactive beam experiments. NPTOOLS combines GEANT4 with the ROOT analysis framework in C++, which is extensively used in this work for data analysis and visualization while NPTOOLS and GEANT4 were carried out by Julien Bordes [7] and only experimental work done by me in this work.

3.0.6 Work process

The diagram below illustrates the workflow of the analysis process, showing how the work begins and how the final results are obtained. As mentioned earlier, the raw experimental data were stored on the NP11 machine at the University of York. These data included information such as energy, time, and amplitude, as shown in the diagram. The data were then processed using a code provided by Soham, which was subsequently modified and updated according to the experimental conditions. After applying the required adjustments, the analysis procedure was carried out and the corresponding results were obtained.

3.0.7 Beam production

In this experiment, the stable beam of ^{14}N has been used. These were produced using the ISAC (Isotope Separation and Acceleration) microwave ion source, which provides a stable beam from an underground setup for producing radioactive ion beams (RIBs). The radioactive ion beams are produced using of TRIUMF's main cyclotron which is able to produce a beam of 500 MeV [34]. The loss energy of the beam as it goes through the entrance and exit window is computed, and simulations are carried out to model nuclear reactions between the beam ^{14}N and mixture gas He:CO_2. These reactions produce particles and elements such as Rutherford scattered ^{4}He, ^{1}H and ^{17}O and even in the case of elastic scattering could produce ^{14}N all originating from the target gas. The Tactic Beam program tracks these reaction products, determining the endpoints and vertices of their trajectories.

Workflow analysis

The workflow below 3.7gives a complete explanation of the starting point and how the raw data from the detector signal from the collision between the beam and target are turned into real physical results and how the particles were produced.

Raw data When the beam interacts with the target gas, a large number of drift electrons, mixed with electronic noise, are produced and recorded as signals across the detectors. These signals are then reconstructed and corrected, providing three types of information: amplitude, time, and pad information

Amplitude The first type of information obtained is the amplitude, which is used to determine the total energy deposited in the detector pads (ΔE/pad). As charged particles pass through the detection region, they lose energy, which is deposited in the detector system. By measuring the amount of energy lost along a track and combining it with the time taken to reach the detector, it is possible to identify the type of particle. Once the particles are identified, for example protons,

the proton yield can be extracted. This information is then used to calculate the reaction cross section and to estimate the probability of the reaction.

Time and Pads Timing measurements (or electronic drift time) provide complementary information of the particle identification and led us to to measure track angle for the track particles. The time differences between particles detection and event start allows estimation of particle velocity as previously described in the track radius section. The charged particle multiplicity (pads) is defined as a number of reconstructed initial tracks per events within specific condition acceptance.

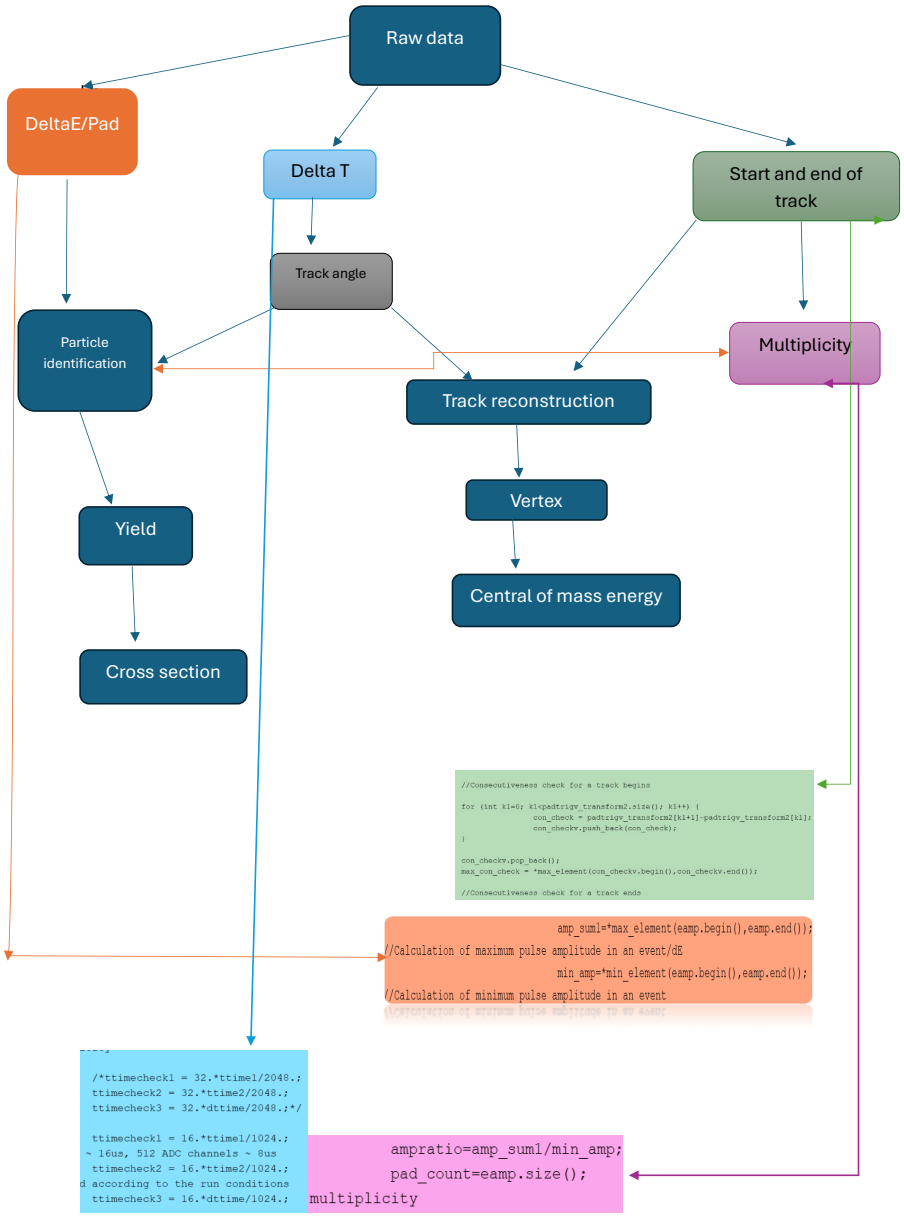

Figure 3.7: workflow of the simulation process and the type of data analyzed

Summary and outlook The above figure presents the workflow graph and analysis have presented a comprehensive description of the experimental analysis chain used to extract charged particle yields and production cross sections from raw data. By analysis the reconstruction and correction steps as showed above we can confidently say that the final results reflect to the real physics information behind the data. This framework provides a reliable starting point for high precision measurements and allows the results more meaningful and can employed to identify the particles and cross section as well as central of mass energy.

3.0.8 Simulation Event Creators

Event Creators specify different components of a simulation such as beam particles, reactions, and decay processes, even can be customized so the output of one serves as the input for another.

Beam

The beam event generator is used to define the beam emittance and energy, either by using a Gaussian parametrisation or by importing distribution files in standard ASCII or ROOT formats. For each simulated event, the beam energy, propagation direction, and impact position at the entrance of the target volume are defined. The primary beam particle then passes through the user-defined target and loses energy according to the Geant4 energy-loss tables until it reaches an interaction point. This interaction point is randomly selected from a uniform distribution within the target thickness. The figure below shows an example of the simulation code used to model the $^{14}\mathrm{N}(\alpha, p)^{17}\mathrm{O}$ reaction. In the simulations presented in this work, a square mono-energetic beam profile with zero angular divergence at the target entrance was used.

The two graphs in Figs. 3.9 and 3.8 show that the change in the beam transverse profile along the target length is mainly driven by multiple scattering and energy loss in the target gas, which together cause the beam to gradually broaden as it propagates downstream. As the beam travels through the target, its transverse size increases steadily due to these effects. The similar behaviour observed for both reaction channels demonstrates that the beam transport is modelled consistently throughout the simulations.

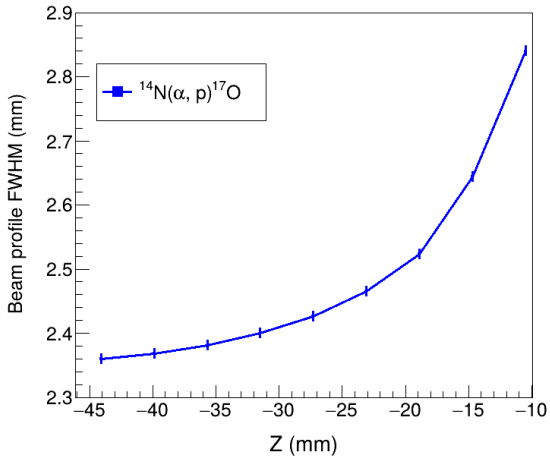

Figure 3.8: Evolution of the beam transverse profile (FWHM) along the beam direction within the target volume for the reaction $^{14}\mathrm{N}(\alpha, p)^{17}\mathrm{O}$. [7]

In contrast, the beam energy spread behaves differently: it first increases due to energy straggling and then decreases further downstream, as lower-energy particles are more likely to be absorbed in the target material. As a result, the energy distribution of the transmitted beam becomes narrower.

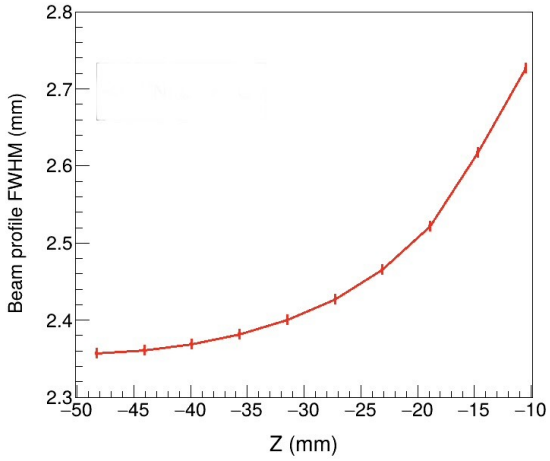

Figure 3.9: Evolution of the beam transverse profile (FWHM) along the beam direction within the target volume for the reaction $^{14}\mathrm{N}(\alpha,\alpha)^{14}\mathrm{N}$. [7]

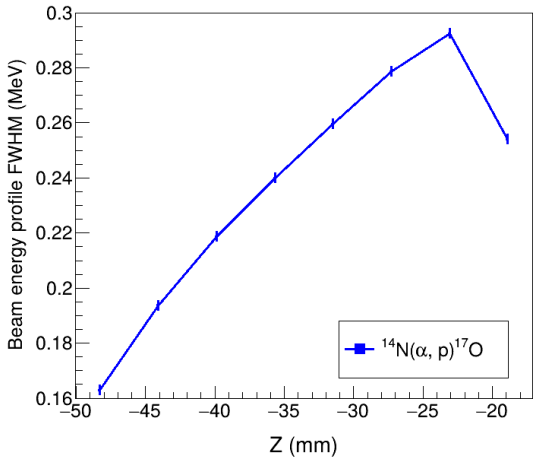

Figure 3.10: Beam energy profile for the reaction $^{14}\mathrm{N}(\alpha,p)^{17}\mathrm{O}$ [7].

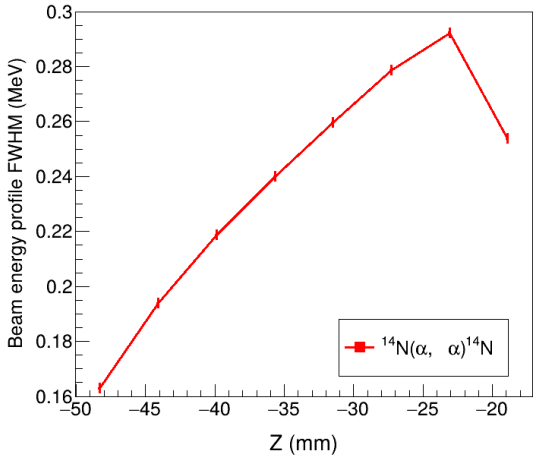

Figure 3.11: Beam energy profile for the reaction $^{14}\mathrm{N}(\alpha,\alpha)^{14}\mathrm{N}$ [7].

Two-Body Reactions

The Two Body Reaction event generator 3.12 models nuclear reactions between the primary beam particle (Beam), defined by the Beam event generator, and a target nucleus (Target), producing two nuclei in the exit channel (Light and Heavy), i.e., the reaction products.

```
static constexpr int beamProf_nBinsX = 60;
static constexpr double beamProf_minX = 1.;
static constexpr double beamProf_maxX = 61.; // = minX + nBi
static constexpr int beamProf_nBinsY = 200;
static constexpr double beamProf_minY = -10.;
static constexpr double beamProf_maxY = -beamProf_minY;

static constexpr int beamEProf_nBinsX = 60;
static constexpr double beamEProf_minX = 1.;
static constexpr double beamEProf_maxX = 61.; // = minX + nB
static constexpr int beamEProf_nBinsY = 2000;
static constexpr double beamEProf_minY = 0.;
static constexpr double beamEProf_maxY = 40.;
```

Figure 3.12: Simulation beam for one-body configuration [5].

Geometry

For a specific experiment, the detector's geometry can be specified in the Geant4 files located within the npsimulation utility, and inside the NPSimulation directory of the distribution. When the simulation runs, a specific detector geometry can be chosen and desired target composition such as the gas mixture used in TACTIC or the test chamber can be defined through the geometry file as showing the figure 3.2.

The final step must be mentioned is how the TACTIC simulation process and can record results. The main idea is charged particle tracking from the nuclear reaction or radioactive decay gives a simulated event in TACTIC and the test chamber. The track is propagated through the simulation in discrete steps of 0.1 mm. After every step, the simulation retrieves the current status of the track and associated data such as track length, track angle, energy loss, etc ... across the step is called as a script. The scripts divide outer copper cylinder of TACTIC into 60 horizontal segments to simulate the anode pads, but for simplicity, the simulation only models

one sector containing all 60 pads. As a particle moves through the detector, the script determines which pad it is passing through and keeps track of the energy loss at each step. The track length, z-position, and radius are updated continuously, while static information such as the vertex position and track angle is recorded once and applied to all pads.

Chapter 4

Results

In this part of the work, we present the experimental training phase that was initially carried out using a stable ^{23}Na beam. This part represented a crucial step toward gaining a deep and solid understanding of the detector response, the raw data workflow and the full chains analysis. Relying on ^{23}Na data, which are well characterized and relatively clean, provided a reliable framework for testing reconstruction techniques, developing particle-tracking algorithms, and validating particle-identification methods under well-controlled conditions.

The experience acquired during this training phase had a direct impact on the analysis strategy later applied to the raw data obtained with the stable ^{14}N beam. In particular, the knowledge gained from detector calibration, trigger-system behavior, pulse-shape analysis, and ΔE–E particle-identification techniques based on the ^{23}Na dataset contributed to refining selection criteria and improving the robustness of track reconstruction when dealing with the more complex ^{14}N data. This progression also allows for a meaningful comparison between the analysis methodology developed during my training period and the earlier work performed by Soham Chakraborty [5], thereby highlighting both methodological improvements and the evolution of the analysis pipeline.

In addition, this study benefited significantly from the simulation tools NPTOOL and GEANT4. Although these tools were not directly used in this work, the analysis benefited from simulation results obtained in previous studies, as discussed in Chapter **??**. These tools provided realistic modelling of the detector geometry, energy-loss mechanisms, and reaction kinematics, which were essential for interpreting the experimental signals. The combination of simulation results and experimental measurements enabled a more precise reconstruction of the $^{14}\mathrm{N}(\alpha, p)^{17}\mathrm{O}$ reaction and allowed for the reliable identification of the emitted particles, including protons, alpha particles, and other light fragments.

4.0.1 Experimental methods and important parameters

General views about the methods

In TACTIC, the reaction vertex cannot be detected directly because the detector does not record the differential energy loss$\left(-\frac{dE}{dx}\right)$ at the point where the nuclear reaction occurs while the chamber is shielded by cathode cage. Identifying these vertices is important for estimating the reaction energy. As mentioned in Chapter (TACTIC), the TACTIC reconstructs the unobserved reaction vertices by predicting the trajectories of the detected particles, then analyses these tracks to identify the particles and uses the resulting products as(the detected event counts) to

determine the excitation function.

Reconstruction of reaction vertex

Experimentally, the relative drift time of ionisation electrons produced by the interaction of charged particles with the target gas plays a crucial role in particle tracking and in the reconstruction of reaction vertices within the detection region. By calculating the electron drift time and identifying the signal deposited on the readout pads, the track radius r_d and the track base position z_d inside the active volume are determined. The track angle (θ) and the track endpoint z_f can also be extracted; however, their associated uncertainties increase with the anode pad width ($P_w = 4.2$ mm). As illustrated in Fig. 4.1, a portion of the track located inside the cathode cage ($r < 12$ mm) remains undetected. Consequently, the observed track segment is extrapolated to reconstruct the reaction vertex position (v_z).

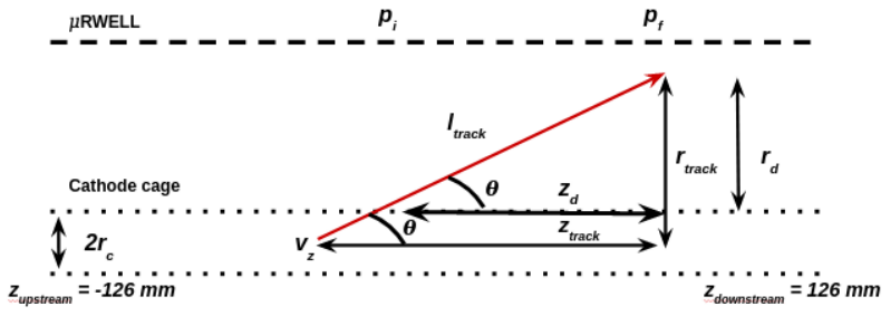

Figure 4.1: A schematic diagram of TACTIC illustrating a charged particle track [5]

Below are a list of the equations and important parameters which are useful for our work [5]

$$z_d = p_w \cdot m_{\text{track}} \tag{4.1}$$

$$\theta = \arctan\left(\frac{r_d}{z_d}\right) \tag{4.2}$$

$$r_{\text{track}} = r_c + r_d \tag{4.3}$$

$$z_{\text{track}} = \frac{r_{\text{track}}}{\tan\theta} \tag{4.4}$$

$$v_z = z_f \pm z_{\text{track}} \tag{4.5}$$

where : m_{track} is track multiplicity, defined as the number of pads with signals above the detection threshold. r_c is a radius of the cathode cage and equal to 12 mm. z_f is the z-coordinate of p_f. r_d can be calculated by estimating the trigger time difference between p_i and p_f. The drift time difference corresponds to the trigger time difference measured by the DAQ between the initial and final pads of a track.

Measuring track radius

Accurate calculation of the track radius is essential for reliable tracking within the detection region and for precise reconstruction of the reaction vertex. The drift times of ionization electrons collected by each individual pad after terminated at μ-RWELL are used to determine the track radii. Garfield [24] was used to simulate the electric field and calculate electron drift times in the cylindrical TACTIC setup. The drift time depends on the gas composition, electric field strength, and pressur

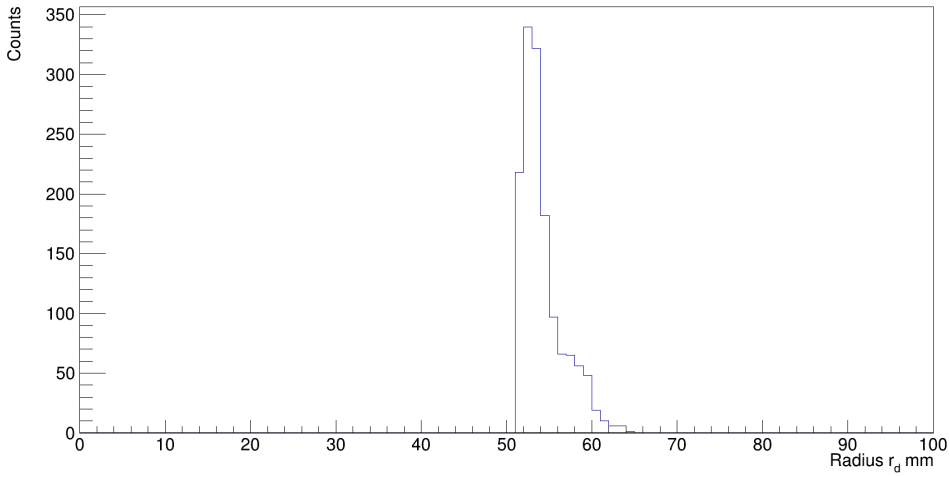

Figure 4.2: Calculated track radii for multiple events. Majority of the tracks in the data set terminate at the μ-RWELL ($r \approx 50$ mm). Gaussian fit of the peak yielded the maximum value of $r_{\text{track}} = 50.2 \pm 2.3$ mm

Garfield uses the Magboltz [25] program, which provides extensive electron gas interaction cross sections, to calculate electron drift velocities. The calculations assume uniform gas pressure and a homogeneous gas mixture, an assumption supported by the use of a constant gas flow during testing. With the pressure fixed, the drift time is mainly determined by variations in the electric field along the electron's path. By accurately measuring the drift time and knowing how the drift velocity changes with position due to the chamber geometry, the radius of origin of each electron can be determined. In TACTIC, each pad along a track therefore had a unique drift time and a corresponding radius value. The electric fields used in the Garfield calculations were selected to match the range of electrode voltages expected during operation. Calculating the field inside TACTIC is challenging because the chamber is not perfectly symmetric in ϕ. The pitch of the inner and outer cathode wires is not sufficiently fine to be treated as uniform, resulting in variations of the electric field within the cathode cage as a function of ϕ.

Field distortions also arise from the influence of neighboring wires in the gap between the inner and outer cages [35]. These asymmetries lead to small variations in drift time and can affect the reconstruction of the drift radius. To manage this, an approximation was adopted that adequately represents most drifting electrons [35]. Studies have shown that the drift-time variation with ϕ is small and is mainly confined to regions very close to the cathode wires ($r < 13$ mm) . As a result, a drift-time calibration from Garfield—assumed independent of ϕ—is sufficiently accurate.

Garfield was therefore used to simulate the electric field and drift times along a radial line midway between adjacent outer cathode wires (from $r \approx 12$ mm to $r \approx 50$ mm, the region

up to the μ-RWELL). The simulations used DRIFT_MICROSCOPIC_ELECTRON for single-electron transport and MICROSCOPIC_AVALANCHE for re-ionisation. These calculations incorporate the TACTIC geometry, gas mixture, pressure, and drift field.

Electrons were released from different radial positions within $12\,\text{mm} \lesssim r \lesssim 50\,\text{mm}$ in 100 steps (it is reasonable and for the accuracy approaches) , and the resulting drift times are shown in Fig. figs. 4.3 to 4.5 In principle, the fit function in this figure can be used to convert any drift time into a radius. However, because TACTIC is self-triggering, it records *relative* drift times rather than absolute ones. For each event, the initial pad that fire (the one closest to the μ-RWELL) defines $t_0 = 0$, and all other pad drift times t'_{di} are measured relative to this trigger time.

$$t'_{di} = t_i - t_0 \tag{4.6}$$

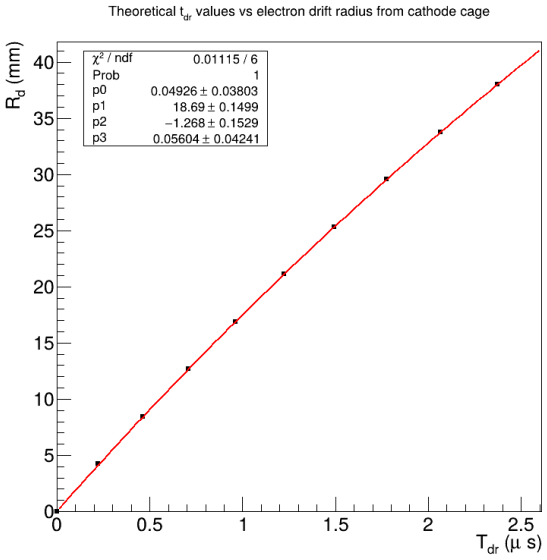

Figure 4.3: A plot showing the calculated drift times (t_{dr}) for electrons traveling from the outer cathode cage toward increasing radii, up to the radius of the μ-RWELL. The longest drift time, equal to $t_{\text{full}} = 2.6\ \mu$s, corresponds to a maximum drift radius of $r_{\text{d}} \approx 38$ mm, which represents the full drift region of the chamber. The simulation was performed using a He:CO_2 (90:10) gas mixture at 0.5 bar with a drift voltage of $V_{\text{drift}} = -1400$ V [9]

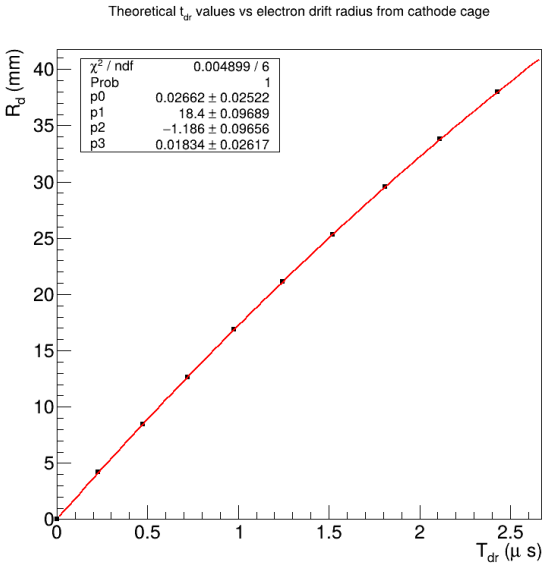

Figure 4.4: A plot showing the calculated drift times (t_{dr}) for electrons traveling from the outer cathode cage toward increasing radii, up to the radius of the μ-RWELL. The longest drift time, equal to $t_{\mathrm{full}} = 2.6\ \mu$s, corresponds to a maximum drift radius of $r_{\mathrm{d}} \approx 38$ mm, which represents the full drift region of the chamber. The simulation was performed using a He:CO_2 (90:10) gas mixture at 0.5 bar with a drift voltage of $V_{\mathrm{drift}} = -1300$ V [9]

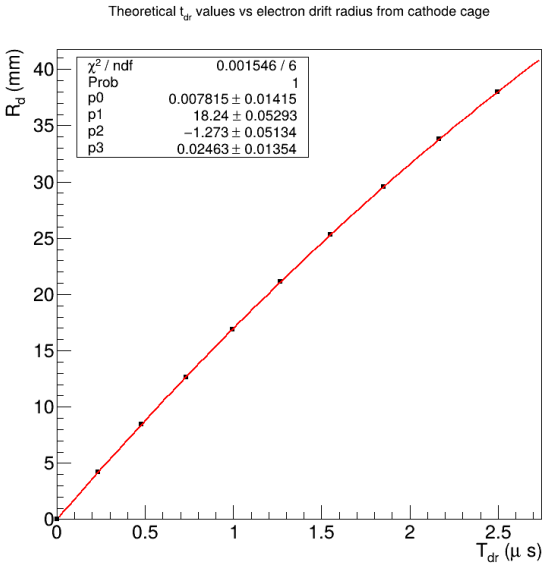

Figure 4.5: A plot showing the calculated drift times (t_{dr}) for electrons traveling from the outer cathode cage toward increasing radii, up to the radius of the μ-RWELL. The longest drift time, equal to $t_{\mathrm{full}} = 2.6\ \mu$s, corresponds to a maximum drift radius of $r_{\mathrm{d}} \approx 38$ mm, which represents the full drift region of the chamber. The simulation was performed using a He:CO_2 (90:10) gas mixture at 0.5 bar with a drift voltage of $V_{\mathrm{drift}} = -1200$ V [9]

where t_i denotes the trigger time recorded by each pad contributing to a given track. To extract the relative drift times, it was assumed that the largest measured time with respect to $t = 0$

represents the full drift time (t_{full}) for that run. This value depends on the operating conditions, namely the gas mixture, pressure, and applied drift voltage. The quantity t_{full}, obtained from Garfield simulations, corresponds to the electron drift time from the cathode cage to the μ-RWELL.

The data were then shifted by subtracting the absolute drift times (t_{d}) from t_{full}, and the associated radii were adjusted using Eqs. (4.7) and 6.16. This procedure produces a set of theoretical t_{dr} values for various drift radii (r_{d}), as shown in Fig. 4.3.

$$t_{\text{dr}} = t_{\text{full}} - t_{\text{d}}(r_i) \tag{4.7}$$

$$r_{\text{d}} = r_i - r_c \tag{4.8}$$

where $r_i > 12$ mm and $r_c = 12$ mm. The data shown in Fig. 4.3 were fitted using a polynomial function.

$$r_{\text{d}} = p_0 + p_1 t_{\text{dr}} + p_2 t_{\text{dr}}^2 + p_3 t_{\text{dr}}^3 \tag{4.9}$$

The above equations help us to calculate the trigger time and max time by using Garfield.

Consecutiveness

To calculate the track base (z_d) using Eq. 4.1, the track multiplicity (m_{track}) must be estimated accurately. When a track contains missing points, the determination of m_{track} becomes less reliable, which can introduce a systematic uncertainty (because the error introduced by missing points is not random from event to even) in the reconstructed vertex. To minimize this effect, a parameter referred to as *continuity* (or consecutiveness) was used in the analysis to identify tracks with gaps resulting from non-hit pads [5].Generally, to identify c_{track} in tactic we use the equation as expressed

$$c_i = p_{i+1} - p_i \quad ; \quad 1 \leq i \leq 60 \tag{4.10}$$

Here, c_i represents the consecutiveness parameter, while p_i denotes the pad position corresponding to signals that exceed a predefined threshold. Missing points along a track can arise from several factors, including electronic noise and the detection threshold applied at the digitiser. The figures 4.6 show examples of tracks with a continuity value of $C_{\text{track}} = 1$, which were selected for vertex reconstruction. In addition, a minimum track multiplicity requirement of $m_{\text{track}} \geq 4$ was applied for the ^{14}N beam in order to ensure a more reliable determination of the vertex position.

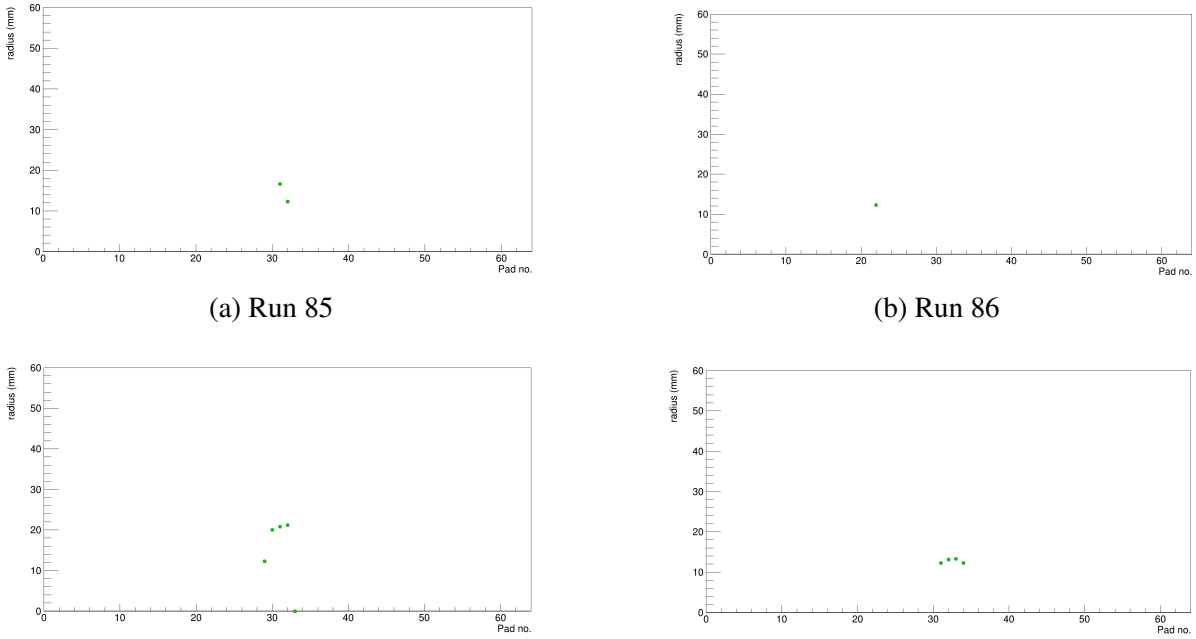

(a) Run 85

(b) Run 86

(c) Run 91

(d) Run 98

Figure 4.6: Comparison of Radius vs Pad number for four different runs (85, 86, 91, and 98).

those four figures can shows us more how the track begins at cathode cage (12 mm) and terminate at the μ-RWELL at (50 mm).

Pulse height

Due to the lack of reliability of the pulse generator for energy calibration, systematic variations were observed among the preamplifier channels. In the TACTIC, the preamplifiers were identical to those used in the test chamber. Therefore, an absolute energy calibration was not performed. To convert the measured pulse heights into energy, an alpha source ^{148}Gd isotope was employed. However, in TACTIC, the presence of the cathode cage complicates the energy calibration, as a fraction of lose energy. Consequently, simulations were used to investigate the effects of geometrical parameters on the energy response. A good agreement was obtained between the simulated results and the experimental data from alpha-source measurements, particularly in terms of trajectory parameters. As a result, the analysis was performed using the raw pulse-height values, PH_{raw}, defined as the peak amplitude of the negative signal, which typically measures around -150 ADC counts.

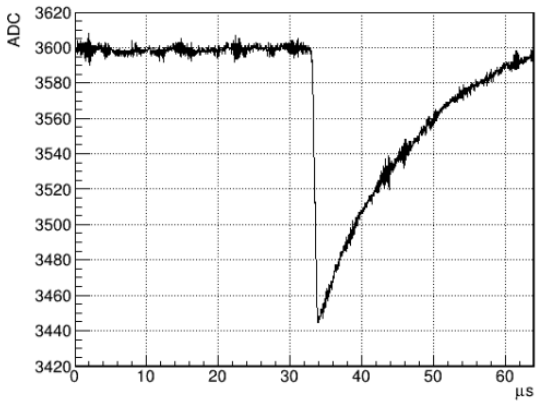

Figure 4.7: Trace of a single pulse from alpha run 02085 (event no. 45) from a CAEN V1740 digitiser channel corresponding to a specific anode pad. The digitiser range is set as follows: on the horizontal (time) axis, $0 \leq n \leq 4096$ ADC or $0 \leq t \leq 64$ μs; and on the vertical (amplitude) axis, $0 \leq y \leq 4000$ ADC [5]

$$x_i(\mu\text{s}) = \frac{x_i(\text{ADC})\,t}{n} \tag{4.11}$$

the above equation generally used to convert the x_i axis from ADC value to time μs and called conversion formula. Here, n represents the recorded length of the ADC channel in units of approximately μs, as set by the digitiser. To obtain a reliable estimate of the pulse height, the raw signal was first processed using the standard moving window deconvolution (MWD) method [36], and then analyzed further using the equation below:

$$PH(k) = \frac{\sum_{i=j}^{j+4} PH_{\text{raw}}(i)}{5}, \quad k = 1,2,3,\ldots, \quad j = 1,6,11,\ldots,n-4 \tag{4.12}$$

where $PH_{\text{raw}}(i)$ is the pulse amplitude at the i-th position on the time axis.

4.0.2 Stable beam ^{23}Na

The in-beam study of the ^{23}Na$(\alpha,p)^{26}$Mg reaction was carried out by Soham [5] in November 2022 within the astrophysically relevant center-of-mass energy range ($E_{\text{cm}} = 1.0$–5.1 MeV) using inverse kinematics. The objective of the experiment was to achieve accurate vertex reconstruction and particle identification within the TACTIC detector. A ^{23}Na beam with an energy of 1.7 MeV/u was delivered from the OLIS facility into the ^{4}He : CO_2 (90:10) target gas described in Chapter 3. The beam entered the detector through a 2.5 µm-thick aluminized-Mylar entrance window. During the experiment, the entrance and exit windows were positioned at -49 mm and 84 mm, respectively, with an uncertainty of ± 3 mm.

As the beam passes through the detector, it gradually loses energy through interactions with the entrance window and the target gas. Figure 4.8 shows the energy loss calculated using TRIM as a function of target depth(z mm). The sharp decrease at small target depths is associated with the beam passing through the aluminized-Mylar entrance window, where the stopping power is considerably higher than in the gas. Once the beam enters the ^{4}He : CO_2 gas region, the

stopping power decreases due to the lower gas density, resulting in a minimum in the energy-loss curve at approximately 0.5 MeV. This minimum indicates the transition from the entrance window to the active gas volume. Beyond this point, the beam continues to lose energy steadily as it travels through the gas target until it eventually comes to rest.

The TRIM simulation results were used to determine the beam energy at different positions along the beam axis. The detector coordinate (z) is defined with respect to the centre of the active target volume, where (z=0) corresponds to the central position of the detector. Negative values of (z) represent positions closer to the entrance window, whereas positive values correspond to positions closer to the exit side of the detector. The beam energies extracted from the TRIM simulation at various positions are listed in Table 4.9. These values show the continuous decrease of the beam energy from approximately 34 MeV at (z=-45) mm to about 1 MeV at (z=30) mm as the beam propagates through the gas target. The data in Table 4.9 were subsequently fitted using a linear approximation over the energy interval

$$6 \leq E_b(\text{MeV}) \leq 35. \tag{4.13}$$

The resulting relation between beam energy and position is given by

$$E_b(z) = 12.4 - 0.5z, \tag{4.14}$$

where E_b is the beam energy in the laboratory frame and z denotes the position along the beam axis in millimetres. For vertex reconstruction, z is replaced by the measured vertex position, $v_{z,m}$, enabling the beam energy at the reaction point to be determined directly. Consequently, Equation (4.14) provides a reliable method for estimating the beam energy at any reconstructed reaction vertex within the active target volume.

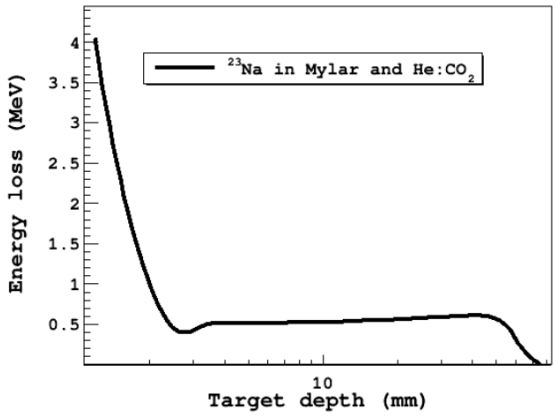

Figure 4.8: TRIM predicted energy loss of the ^{23}Na beam with ^{4}He : CO_2 90:10 gas mixture at P = 1 bar, after passing through the entrance window from Soham [5]

The extracted values are summarized in Table 4.9, showing the variation of beam energy from approximately 34 MeV at $z = -45$ mm to about 1 MeV at $z = 30$ mm. Based on these points, a linear approximation was performed in the energy range presented in Eq 4.13.

The resulting empirical relation between beam energy and position is given by Eq. 4.14

and the estimated beam-energy uncertainty associated with the vertex-position uncertainty is given by

$$\Delta E_b = 0.5\,\Delta z \tag{4.15}$$

where ΔE_b is the uncertainty in the beam energy and Δz is the uncertainty in the vertex position.

To determine the beam energy at a specific reaction vertex, z is replaced by $v_{z,m}$. The linear relation is valid for the beam-energy range $6 \leq E_b(\mathrm{MeV}) \leq 35$. Table 4.9 lists the beam-energy values as a function of target depth (z mm).

Eb (Mev)	Z (MM)
34	-45
33	-41
31.1	-38
29.5	-32
27.5	-30
25	-26
23	-21
21	-17
19	-11
17	-8
14.9	0
13	5
10	9
8	11
5.2	16
3.5	20
1.9	27
1	30

Figure 4.9: A table shows the values of the losing beam energy in verses of depth

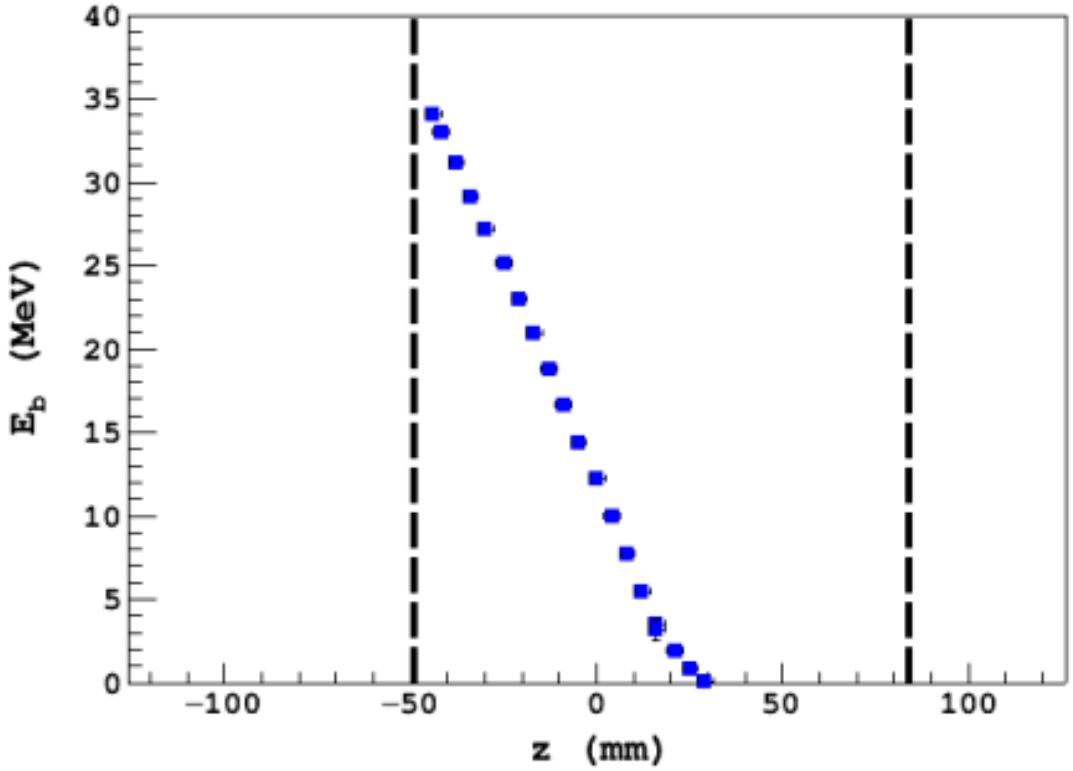

(a) This plot produced by Soham for the reaction $^{23}\mathrm{Na}(\alpha, p)^{26}\mathrm{Mg}$ [5]

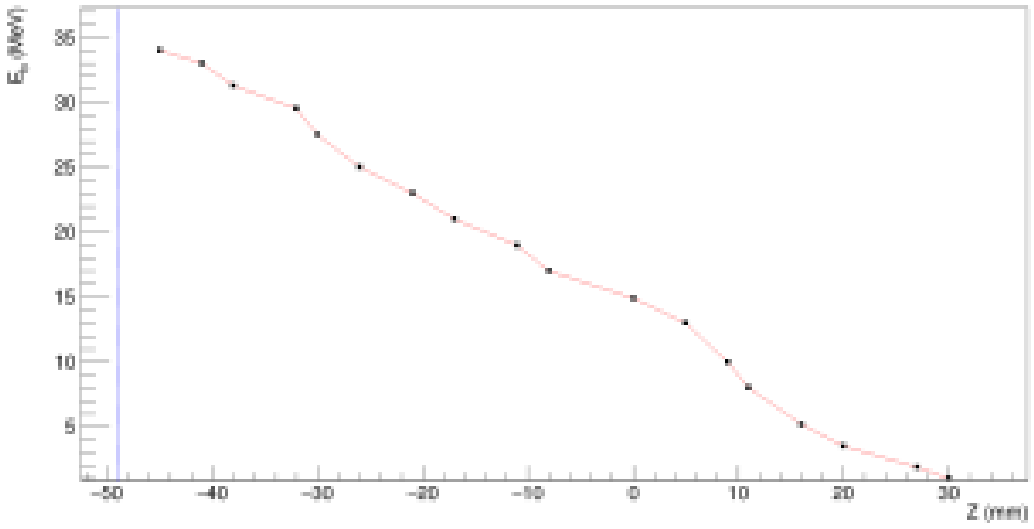

(b) The plot shows the energy lose from experimental data which we got it during the traning period

Figure 4.10: Both figures shows the simulation on left and experimental on right (from the training)

4.0.3 Particle identification

The essential step in TACTIC is to identify the reaction products, as process called particle identification (PID). The elastic scattering occurs between the beam ions and both target gas as

well as the entrance window. In the vertex position distribution, the region outside the Gaussian distribution corresponding to 4σ approximately -38 mm is considered for the identification. The high peak 4.11 in this distribution arises from elastic scattering of the beam at the entrance window, and the region extends up to the μ-RWELL. After the peak point, the track intensity decreases sharply due to energy loss in the target gas. A second sharp drop occurs at approximately $Z = 0$, corresponding to the center-of-mass energy. This reduction in track intensity leads to a corresponding decrease in the yield, which can be attributed to a step-like drop in the (α, p) reaction cross section. For a 1.7 MeV/u ^{23}Na beam was sent during the TACTIC and the entrance window was positioned at -49 mm with using pressure 1 bar for $He : CO_2$ 90:10 has mixture, the reaction cross section was artificially inflated producing different kinds of channels such as :

1. $\alpha(^{23}\text{Na}, p)^{26}\text{Mg}$
2. $\alpha(^{23}\text{Na}, \alpha)^{23}\text{Na}$
3. $^{12}\text{C}(^{23}\text{Na}, ^{12}\text{C})^{23}\text{Na}$
4. $^{16}\text{O}(^{23}\text{Na}, ^{16}\text{O})^{23}\text{Na}$

the following graphs showing the results and training results with compression .

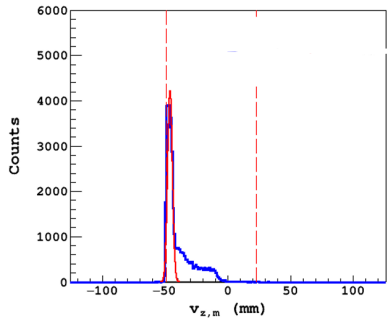

(a) Vertex distribution from the main work [5]

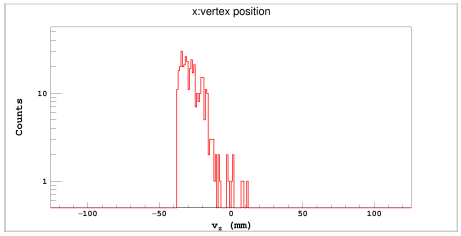

(b) A vertex distribution for a training work

Figure 4.11: The figures show a comparison between the main work carried out by Soham and the training study

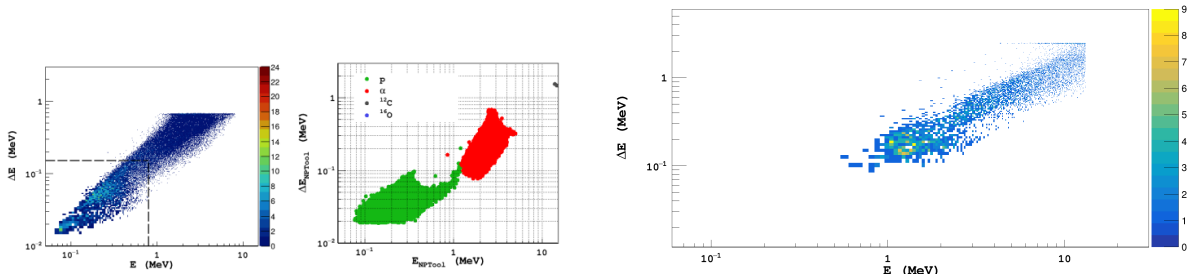

(a) Experimental data (b) Training

Figure 4.12: ΔE versus E from stable beam runs 61, 64, and 65 (sector 1). The following data cuts were applied: $0 < t_i' \leq 7.5$ μs, $r_d > 5$ mm, $m_{\text{track}} \geq 5$, $c_{\text{track}} = 1$, $\Delta v_z < 2.4$ mm, $\Delta\theta < 6.1°$, $\text{PH}_{\text{sum}} < 8 \times 10^4$ ADC, $v_{z,m} > -38$ mm. The black dashed lines indicate the energy cuts used to identify reaction protons, based on simulations. [Right]: a training work with the same conditions.

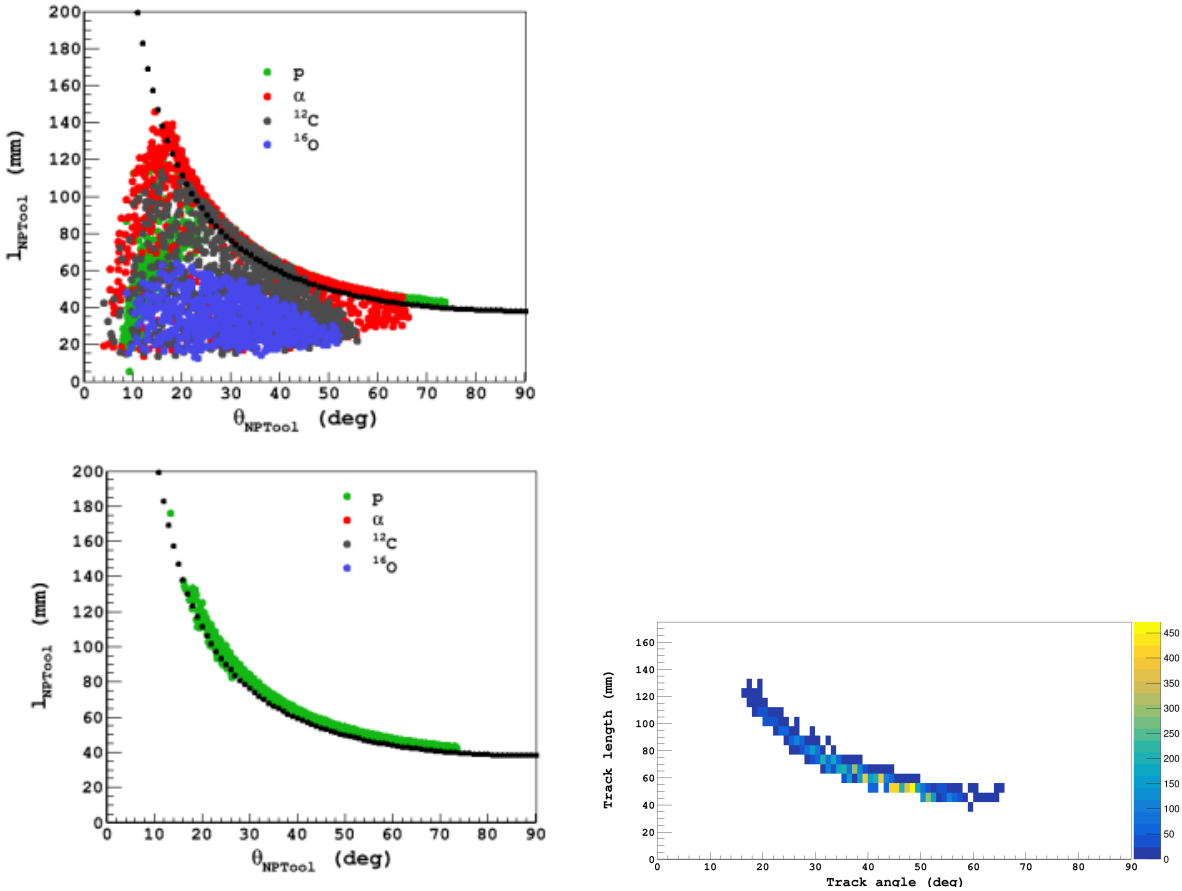

(a) Experimental data (b) Experimental training

Figure 4.13: Comparison of experiment and simulation with my training, the figures show the track length as a function of track angle

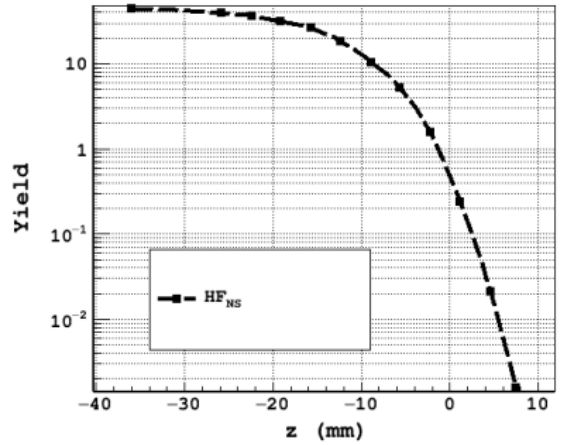

(a) Experimental data, yield

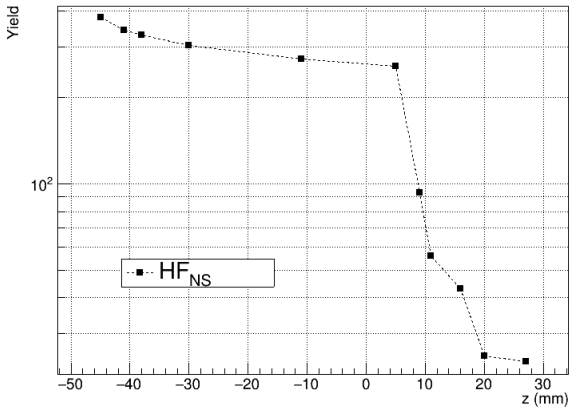

(b) yield training

Figure 4.14: Comparison of experimental and training results for ^{23}Na.

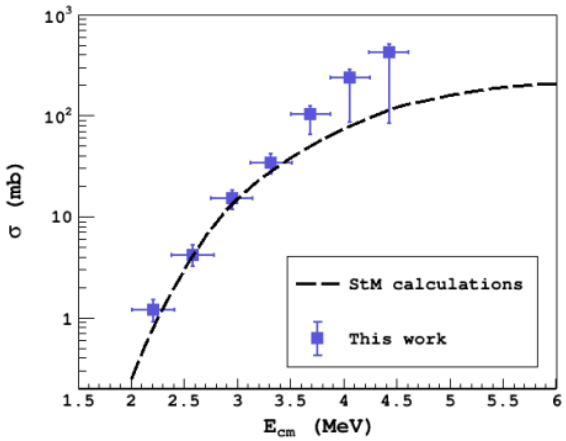

(a) Experimental data

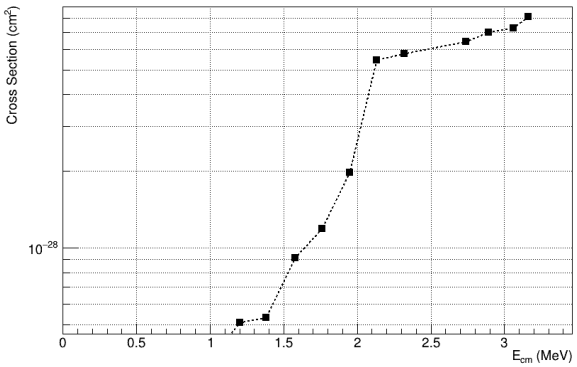

(b) Training

Figure 4.15: Comparison of experimental and training results.

4.0.4 Stable beam ^{14}N

The ^{14}N beam used in this experiment had an energy of 1 MeV/u and was delivered to the TACTIC detector. The beam entered the active volume through a 2.5 μm aluminized-mylar window. As mentioned earlier, the entrance window was located at $z = -49 \pm 3$ mm and exit at $z = 84 \pm 3$ mm. According to the simulation, the in beam loses energy when pass through the window and was calculated (3.5 MeV), while the rest (10.5 MeV) for ^{14}N reacted with the target. A linear equation for the figure 4.16 expressed down as an energy lose as a function of target depth in TACTIC's geometry

$$-126 \leq z(\text{mm}) \leq 126$$

$$E_b = -4.1497 - 0.3074Z \tag{4.16}$$

and

$$\Delta E_b = -0.3074\,\Delta Z \tag{4.17}$$

The linear equation above is valid for beam energies in the range $0.4 \leq E_b\ (\mathrm{MeV}) \leq 10.5$. For the analysis, only energies above 0.4 MeV were considered, since simulations and GEANT4 become inaccurate outside this range. This energy interval also corresponds to the region of interest for the $^{14}\mathrm{N}(\alpha, p)^{17}\mathrm{O}$ reaction.

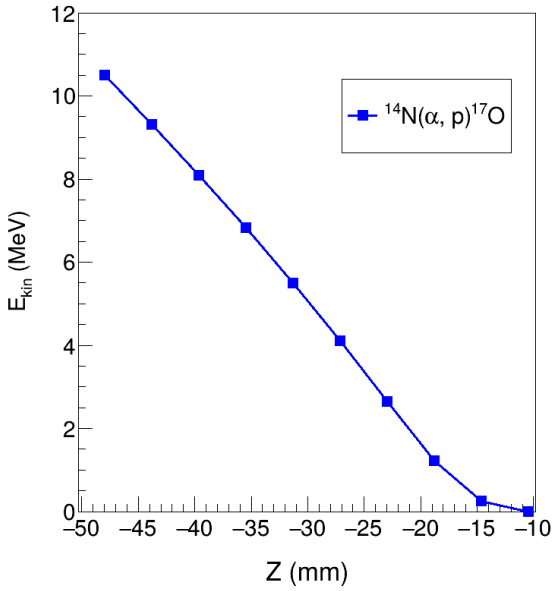

Figure 4.16: The figure shows the beam energy in the lab frame as a function of the target depth in the He : CO_2 (90:10) gas at $P = 1$ bar, in TACTIC coordinates, for simulated ^{14}N.

4.0.5 Vertex energy resolution

In TACTIC, when the beam enters the target region, multiple reactions occur at different locations and at different energies. Consequently, the reaction energy at the interaction vertex, along with the corresponding energy resolution, is a crucial quantity that must be determined as a function of the reaction position. Therefore, evaluating the accuracy with which these reaction vertices can be reconstructed constitutes the primary focus of the in-beam test.

Parameters	^{4}He : CO_2 90:10
Pressure	1 bar
Drift voltage	-1600 volt

Table 4.1: Experimental details for stable beam run75

Figure 4.17 shows the end-point distribution for run 75. Most tracks terminate at the μ-RWELL, while a smaller fraction escape downstream. These escaping tracks primarily correspond to light-particle scattering channels (α–p and p–p), whereas heavier reaction products are absorbed by the cathode cage. Applying strict track-quality cuts and selecting only tracks

that terminate at the μ-RWELL reduces elastic-scattering backgrounds and improves vertex reconstruction, but also decreases the detection efficiency for (α, p) reaction protons.

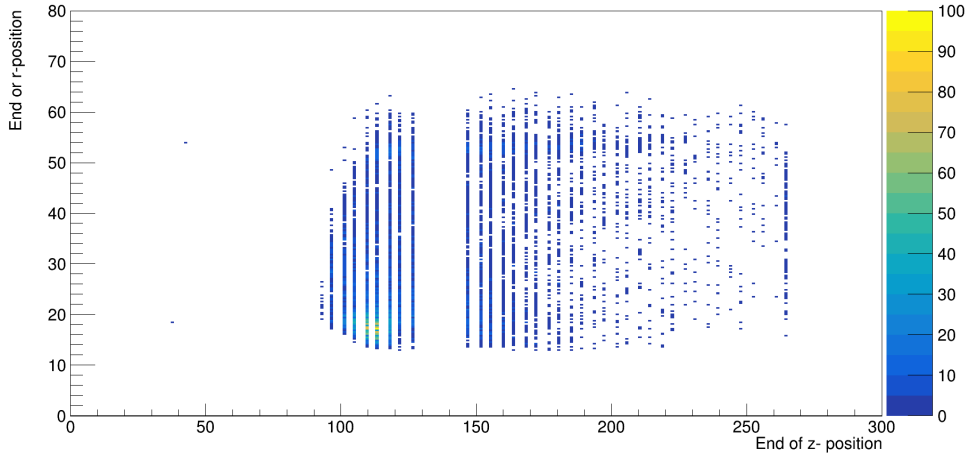

Figure 4.17: End points of tracks from the stable-beam run 75. The entrance window was positioned at $z = -49\,\text{mm}$. Data cuts applied: $0 < t \leq 7.9\,\mu\text{s}$, $m_{\text{track}} \geq 4$, $c_{\text{track}} = 1$.

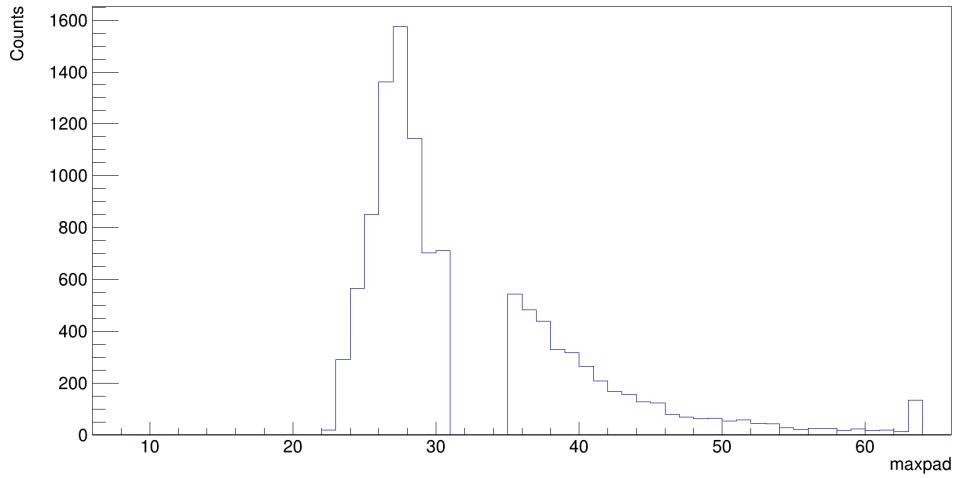

Figure 4.18: Shows the max pad distribution, the gap exactly shows why the gap and that because the channels 31-35 are 4 preamps channels that are not connected to the detector. They can be ignored

Since interactions between the in ^{14}N beam and the target gas occur at multiple positions within the target volume, the interaction vertex must be determined individually for each event. As mentioned previously, the vertex position is not calculated using only the initial and final pads of a track. Instead, the vertex is reconstructed for each pad along the track, referenced to the final pad, as the signal on the last pad (P_f) generates the event trigger.

A peak in the distribution was seen near the position of the entrance window, after which the yield gradually decreased deeper into the gas target. The Mylar window has a density of 9.6×10^{22} atoms cm^{-3}, so with a thickness of 2.5 μm, its effective target thickness is about 2.4×10^{19} atoms cm^{-2}. Using the same approach, the effective thickness of the gas mixture across the full beam path—approximately 72 mm was calculated to be 2.8×10^{20} atoms cm^{-2}.

This means the gas target provides roughly an order of magnitude greater effective thickness than the entrance window. Still, because the atoms in the window are much more densely packed, the reconstructed elastic-scattering vertices originating from the window are expected to be tightly clustered, producing a peak with steep declines on both sides. Another reason for examining the vertex distribution is the second sharp decrease, which corresponds to the centre-of-mass energy. This sharp reduction in yield is caused by the rapid decline of the (α, p) reaction cross section.

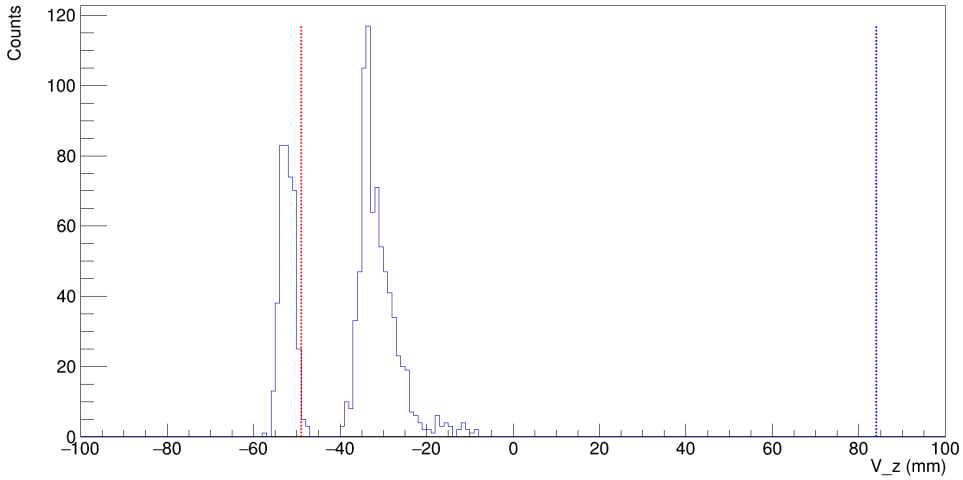

Figure 4.19: Reconstructed vertices for the stable beam run 75. The red and blue dashed lines represent the window entrance and exit. The cuts applied are: time calibration value > 5.5 and < 7.5 μs, $m_{\text{track}} \geq 4$, and $C_{\text{track}} = 1$.

4.0.6 Particle identification

The essential step in TACTIC is the identification of reaction products, a process known as particle identification (PID). The main background in this experiment originates from elastic scattering of the beam ions with the target gas and the entrance window. This scattering produces a clear peak in the reconstructed vertex-position distribution. The peak is caused by elastic scattering at the entrance window and extends up to the μ-RWELL detector.

For particle identification, only tracks with vertex positions inside the target gas are selected. Events associated with the entrance window scattering peak are rejected by applying a cut at approximately 4σ, corresponding to $V_z \approx -18$ mm, in the vertex-position distribution. As a result, the contribution from elastic scattering at the entrance window is effectively removed, leaving only reaction products originating from the target gas region.

After entrance window the vertex distribution expected as mentioned early to reach a peak then decreased down sharply down because of packed atoms in target gas , and another feature of decreasing shown at $Z = -24$ mm, which correspond to the centre of mass energy $E_{\text{cm}} \approx 1.2$ MeV which deduced using Eq. 4.16 and thereafter converted to the beam of mass energy frame. This reduction in vertex distribution leads to a corresponding decrease in the yield, which can be attributed to a step-like drop in the (α, p) reaction cross section.

During the TACTIC experiment, a 1 MeV/u ^{14}N beam was delivered through an entrance window located at $z = -49$ mm. The target consisted of a ^{4}He : CO_2 (90:10) gas mixture at

1 bar. Under these conditions, the reaction cross section was increased to generate a comparable numbers of scattering channels, such as:

1. $^{14}\mathrm{N}(\alpha, p)^{17}\mathrm{O}$
2. $^{14}\mathrm{N}(\alpha, \alpha)^{14}\mathrm{N}$

Figure 4.20 shows the track length as a function of the track angle for different reaction and scattered products. Lighter particles, such as protons and alpha particles, are expected to travel farther, resulting in longer track lengths, with the majority reaching the μ-RWELL. Even after selecting only tracks that reach the μ-RWELL, it remains challenging to kinematically distinguish protons from alpha particles under the given experimental conditions. Recoil nuclei (^{17}O) and scattered beam particles (^{14}N) are not shown, as the heavier nuclei are either shielded by the cathode cage, stopped within the detection region, or produce saturated digitiser signals due to their large energy loss in the gas target.

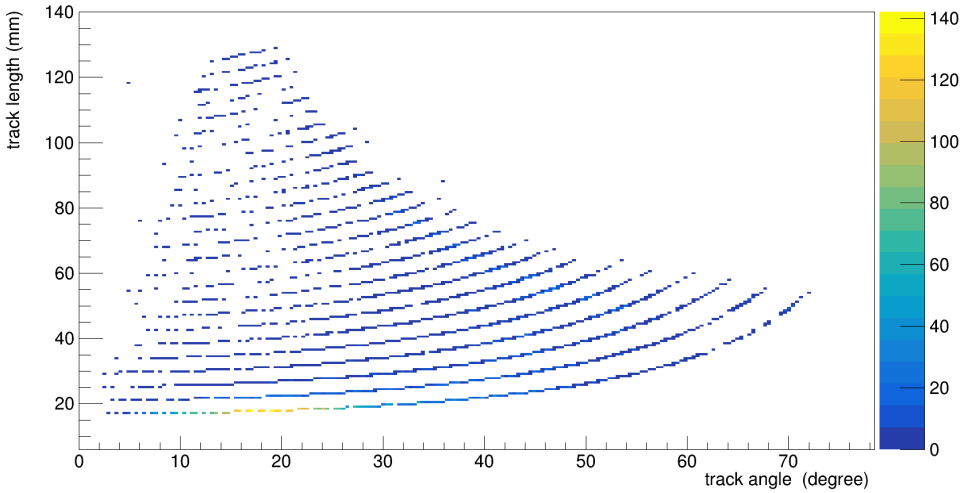

Figure 4.20: Experimental track length versus track angle for the run 75 and for the particles produced. Data cuts used `pad_count >= 4 && ttimecheck3 >= 5.5 && ttimecheck3 < 7.5 && max_con_check == 1`

the reaction products and elastically scattered particles have different charges, which lead to different differential energy losses in the gas. Since the energy loss depends strongly on the ion charge, these differences can be used to investigate and identify particles in TACTIC. The figure 4.21 shows the mean total energy deposited in the gas and shows how can effectively to distinguish between protons , alpha and the other scattered products. The mean energy has been calculated from the equation

$$E_{\mathrm{mean}} = \frac{E_{\mathrm{max}}}{\mathrm{m}} \tag{4.18}$$

Here, E_{max} is the total energy deposited in the detection volume, and m is the track multiplicity. Heavy elements can be easily eliminated based on their energy deposition, as they deposit significantly more energy compared to protons and alpha particles in the detection volume.

The remaining alpha particles and protons are well separated, as shown in 4.21. Reaction protons can be identified as tracks with $E_{\mathrm{max}} < 1$ MeV and a maximum energy deposited per pad

of $\Delta E > 0.3$ MeV. In this selection, the majority of events (approximately 98%) are retained, with only a minor long-tail overlap between alpha and proton events.

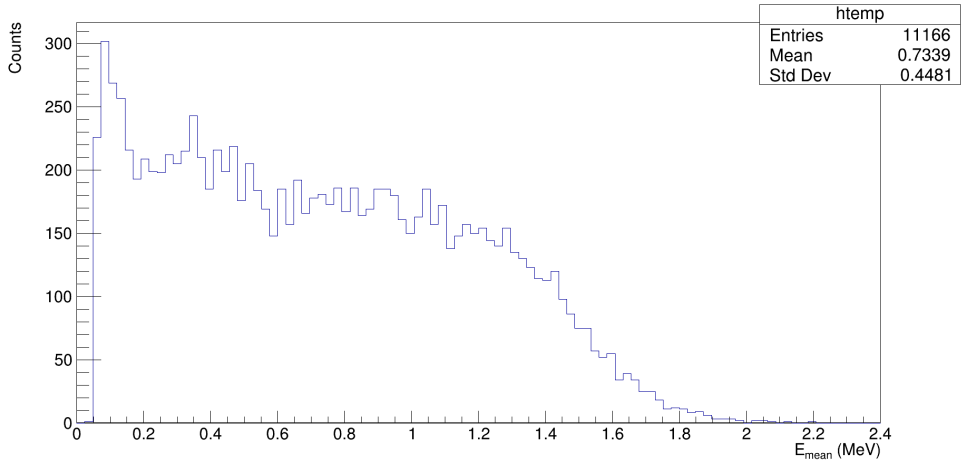

Figure 4.21: Experimental distribution of the mean energy deposited in a track. cuts applied are $m > 4$, energy threshold 50 kev per pad was used in analysis

Figure 4.22b shows the maximum and summed pulse height of the particle tracks from the stable beam run. As it shows the signal saturation at the digitizer channels was fund for the maximum pulse height in the output channels, $\mathrm{PH_{max}} > 3700$ ADC. The uncalibrated quantities $\mathrm{PH_{max}}$ and $\mathrm{PH_{sum}}$ can be viewed as counterparts to ΔE and E, representing the maximum and total energy deposited by a particle track within the detector volume. While certain characteristics—such as the distribution of events in the $\mathrm{PH_{max}}$–$\mathrm{PH_{sum}}$ plane and saturation behaviour—could already be observed, proper energy calibration was necessary to establish a robust particle-identification method based on these parameters.

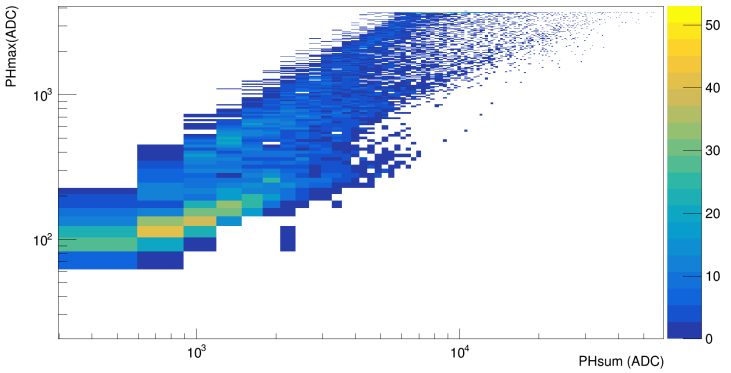

(a) PHmax vs PHsum from stable beam run 75. Cuts applied: `pad_count >= 4 && ttimecheck3 >= 5.5 && ttimecheck3 < 7.5 && max_con_check == 1`.

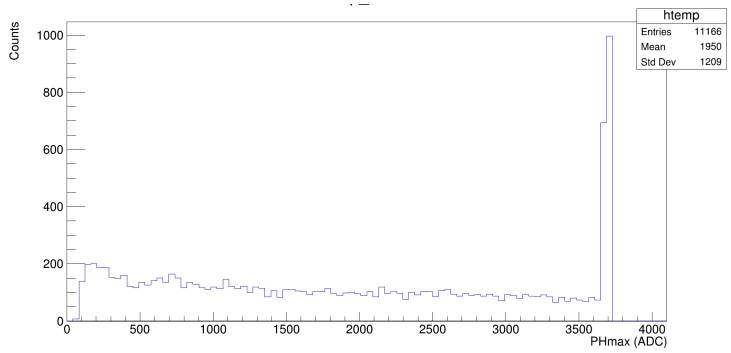

(b) Count versus the PHsum for the same stable beam 75

Figure 4.22: Both show the PHmax versus PHsum and counts versus PHmax for the stablem beam 75. Data cuts used $5.5 < t_{\text{timeck3}} < 7.5$, $m_{\text{track}} \geq 4$, $\text{PH}_{\text{sum}} < 4000$ ADC, $C_{\text{track}} = 1$

The comparison between simulation and experimental data showed that the most saturated at the DAQ channels was observed for the rate $\Delta E > 1.3$ MeV. simulation showed some of the alphas and most of ^{14}N and ^{17}O will cause the signal saturation at the DAQ channels. The simulation suggest that a small numbers of ^{14}N and ^{17}O will be detected as a result of data cuts. in the other hand, the figure 1.14 shows the distribution of the PHmax for a stable beam run 75 that a large numbers of the events saturated. these mainly comes from the blasting scattered products. The figure 4.23 shows the most saturated events in the detection area with $\Delta E > 1.3$ MeV and $(r_{\text{track}} < 50$ mm$)$. The figure shows the energy cuts applied for the reaction proton and scattered alphas.

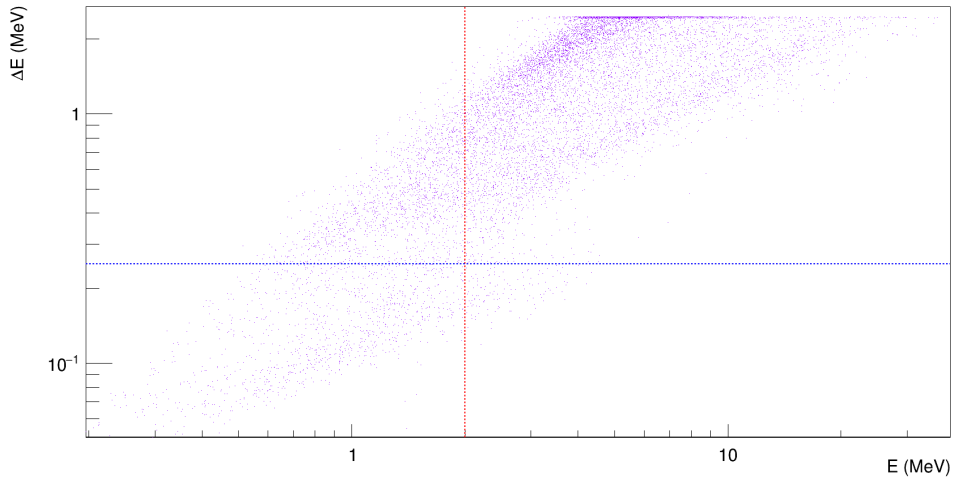

Figure 4.23: ($\Delta E > 1.3$ MeV) versus E for the stable beam run75 and data cuts $5.5 < t_{\text{timeck3}} < 7.5$, $m_{\text{track}} \geq 4$, $\text{PH}_{\text{sum}} < 4000$ ADC, $C_{\text{track}} = 1$. The blue and red lines dashes represent the energy cuts for the identification between reaction proton by using the simulation as the reference

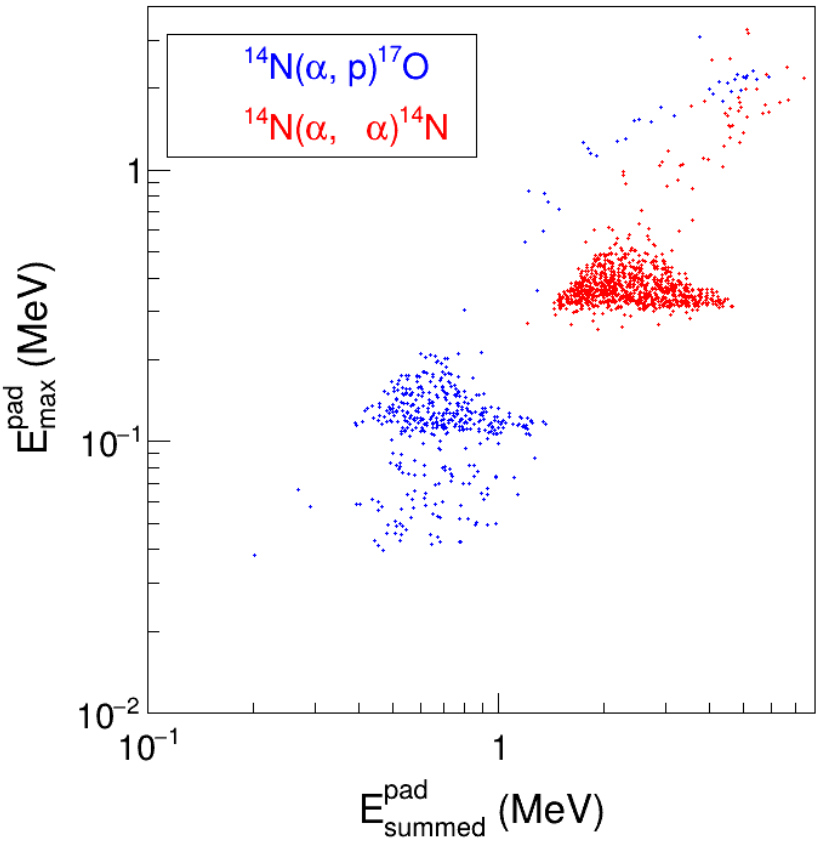

Figure 4.24: Simulated maximum energy versus total energy deposited in a track. Data cut used $5.5 < t_{\text{timeck3}} < 7.5$, $m_{\text{track}} \geq 4$, $\text{PH}_{\text{sum}} < 4000$ ADC, $C_{\text{track}} = 1$. A 50 kev energy threshold been applied per pad in for the analysis

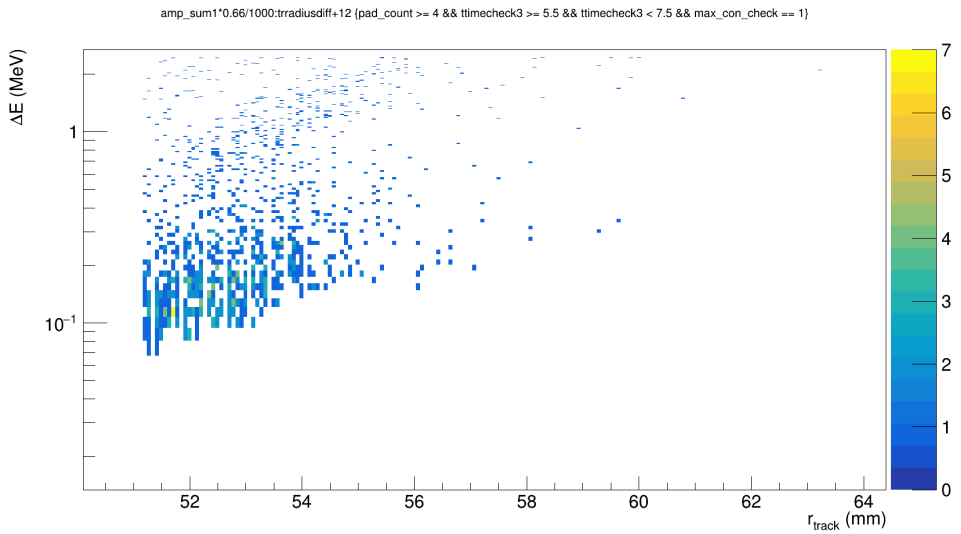

Figure 4.25: ΔE versus track radius from the stable beam run 75. Data cuts used: $5.5 < t_{\text{ttimecheck}\,i} \leq 7.5\ \mu$s, $m_{\text{track}} \geq 4$, $c_{\text{track}} = 1$, $\text{PH}_{\text{sum}} < 4 \times 10^4$ ADC.

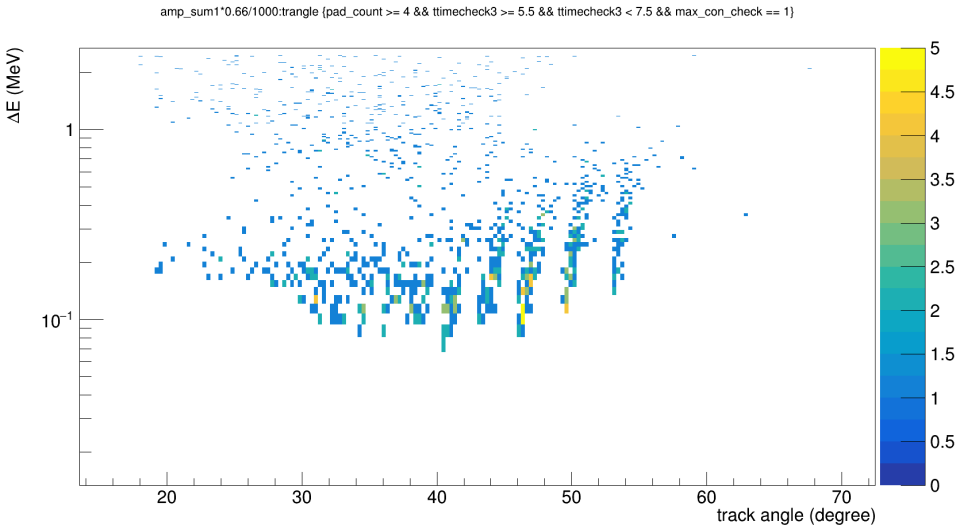

Figure 4.26: ΔE versus track angle from the stable beam run 75. Data cuts used: $5.5 < t_{\text{ttimecheck}\,i} \leq 7.5\ \mu$s, $m_{\text{track}} \geq 4$, $c_{\text{track}} = 1$, $\text{PH}_{\text{sum}} < 4 \times 10^4$ ADC.

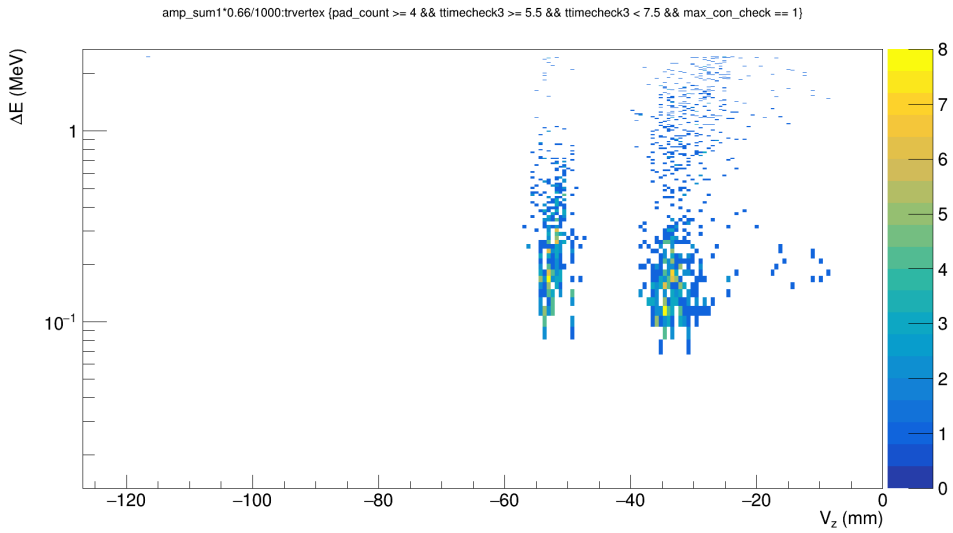

Figure 4.27: ΔE versus vertex position from the stable beam run 75. Data cuts used: $5.5 < t_{\text{ttimecheck}\,i} \leq 7.5\ \mu$s, $m_{\text{track}} \geq 4$, $c_{\text{track}} = 1$, $\text{PH}_{\text{sum}} < 4 \times 10^4$ ADC.

4.0.7 $^{14}\text{N}(\alpha, p)^{17}\text{O}$ Reaction cross section measurements

The particle identification method discussed in the previous section was employed to identify reaction protons and determine the cross section for the $^{14}\text{N}(\alpha, p)^{17}\text{O}$ reaction at different vertex energies. Background arises from elastic scattering of ^{14}N and can also result from fusion-evaporation reactions. As mentioned previously, heavy recoils such as ^{17}O are either absorbed by the cathode cage or cause saturation in the digitiser channels.

The reaction cross section depends directly on the detection efficiency of the reaction protons. Figure 4.28 shows the vertex distribution of reaction protons ($E < 1.3$ MeV) and scattered products ($E > 1.3$ MeV). The proton yield decreases sharply with increasing vertex position, which corresponds to decreasing ^{14}N beam energy.

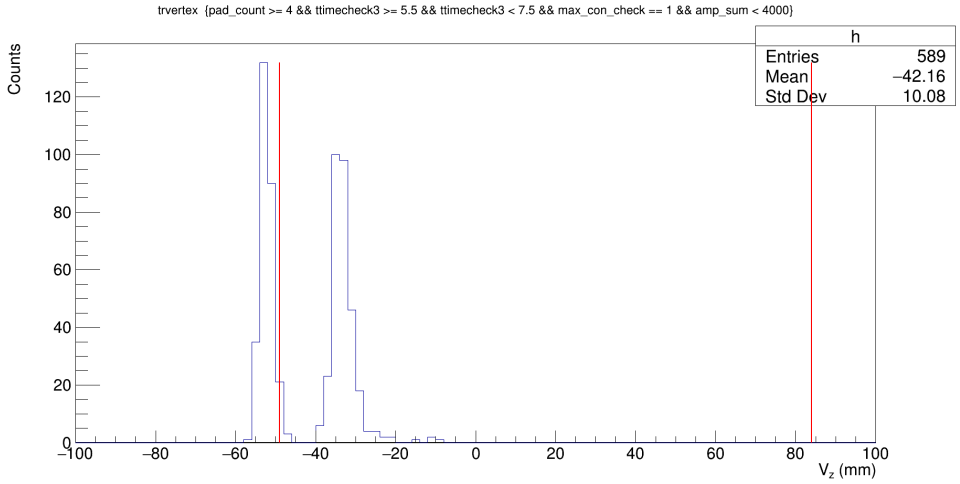

Figure 4.28: Reconstructed vertices from stable beam run 75. The distributions of the reaction proton and scattered particles. The red lines represent the position of the enterence window and range of ^{14}N beam in He:CO_2 90:10. Data cuts used : $5.5 < t_{\text{ttimecheck}\,i} \leq 7.5$ μs, $m_{\text{track}} \geq 4$, $c_{\text{track}} = 1$, $\text{PH}_{\text{sum}} < 4 \times 10^4$ ADC.

Table 4.2 shows that the background from the elastic scattering arises from 4He only.

Parameter	Value
Beam intensity	5×10^5 pps
Run time	1 hour 19 min
Target thickness	0.5 cm
Target density	3.5×10^{19} atoms cm^{-3}
Target composition	He:CO_2 90:10
Proton detection efficiency	1.6%

Table 4.2: Experimental details for stable beam run 75 the simulated proton detection efficiency listed here was taken from the simulation's calculated by Julien, taking into consideration, an energy threshold of 50 keV per pad.

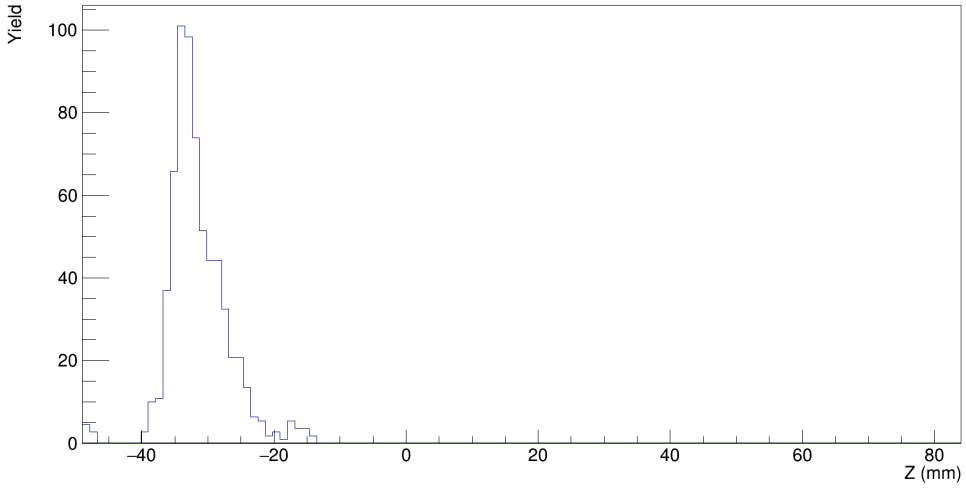

Figure 4.29: Calculated proton yields at different vertex positions using Hauser–Feshbach cross sections and experimental parameters. The parameter z corresponds to the experimentally reconstructed vertex position.

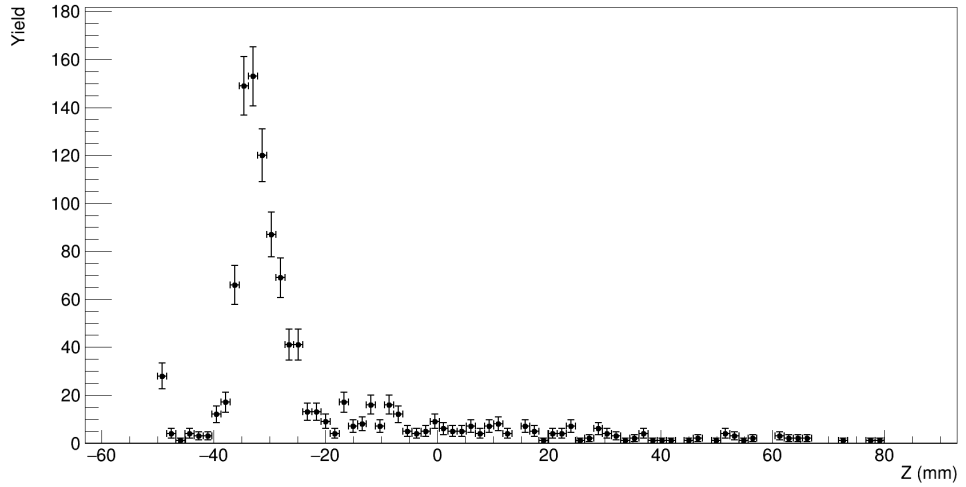

Figure 4.30: The yield distribution was represented using a TGraphErrors, where vertical error bars correspond to statistical uncertainties and horizontal error bars reflect the finite vertex bin width.

4.0.8 Beam normalization

The beam intensity listed in Table 4.2 represents only an approximate estimate. Throughout the full data-taking period, the beam current remained stable. Since the reaction cross-section calculation depends directly on the beam intensity, any changes in the beam conditions must be taken into consideration.

Although the beam-line Faraday cup located upstream of TACTIC provided measurements before and after run 75, it did not capture fluctuations that may have occurred during the run 75. To address this limitation, the yield of elastically scattered alpha particles was used as a more reliable measure for beam normalization. The corresponding alpha yields are expected

to agree within the associated uncertainty, which is dominated by the transmission-efficiency uncertainty. For this suggestion, a dimensionless normalization parameter, ξ, was introduced.

$$\xi = \frac{Y_\alpha}{t \cdot N_b} \tag{4.19}$$

Here, Y_α is the alpha-scattering yield, t is the run time, and N_b is the measured beam intensity before the start of the run. Figure 4.31 shows $\mathrm{PH_{sum}}$ as a function of the track vertex. This plot clearly indicates the conditions under which the alpha raw yield can be extracted, which is then used to determine the alpha-scattering yield and the corresponding experimental efficiency.

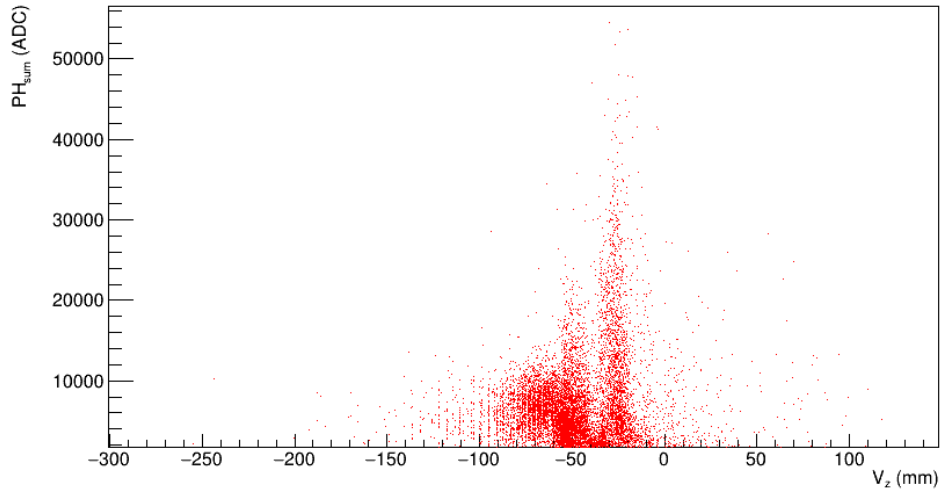

Figure 4.31: $\mathrm{PH_{max}}$ versus V_z. Selection cuts: $5.5 < t_{\mathrm{ttimecheck}\,i} \leq 7.5$ μs, $m_{\mathrm{track}} \geq 4$, $c_{\mathrm{track}} = 1$, $\mathrm{PH_{sum}} < 4 \times 10^4$ ADC, and $-100 < V_z < 100$.

The detection efficiency of the TACTIC TPC was evaluated for both the elastic $^{14}\mathrm{N}(\alpha,\alpha)^{14}\mathrm{N}$ channel and the $^{14}\mathrm{N}(\alpha,p)^{17}\mathrm{O}$ reaction as a function of the applied pad multiplicity cut. The elastic α particles produce long, highly ionizing tracks that typically span many pads, resulting in a high intrinsic detection efficiency of approximately 60–80% when no multiplicity requirement is imposed. As the multiplicity threshold is increased, the efficiency decreases gradually, reflecting the loss of events whose tracks terminate near the detector boundaries or suffer partial reconstruction. In contrast, the efficiency for detecting protons from the (α,p) channel is significantly lower, at the level of 10^{-4}–10^{-3}, because proton tracks are short and deposit relatively little energy, often falling below the track-building and pad-threshold requirements. The efficiency curves therefore highlight the fundamentally different tracking signatures of α and proton events, and demonstrate that multiplicity cuts can strongly bias the relative acceptance of the two reaction channels.

The normalization method used in this analysis should be regarded as an approximate approach, as it relies on the consistency and stability of the normalization parameter ξ obtained from run 75. Ideally, the Rutherford elastic–scattering yield would be calculated independently and used as a more reliable reference for beam normalization. However, due to the large effective target thickness (approximately 72 mm) and the non isotropic distribution of track angles observed in TACTIC, an analytical determination of the elastic scattering cross section is not straightforward. A more robust solution would be to implement the Rutherford scattering cross

section within the existing simulation framework, replacing the isotropic distribution currently assumed.

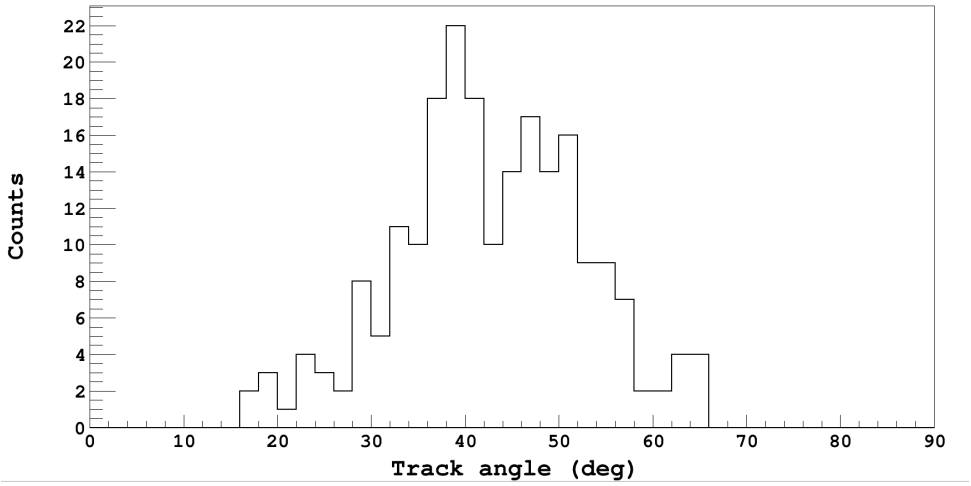

Figure 4.32: Track angle distribution for the stable beam run75. Data cuts used :$5.5 < t_{\text{ttimecheck}\,i} \leq 7.5$ μs, $m_{\text{track}} \geq 4$, $c_{\text{track}} = 1$, $\text{PH}_{\text{sum}} < 4 \times 10^4$ ADC, and $-100 < V_z < 100$.

The plots -4.33 and 4.34 shows how efficiency reaction with the multiplicity. The efficiency been calculated regarding to the equation 4.20 for the proton reaction and elastic scattering.

$$\varepsilon = \frac{N_{\text{detected (after cuts)}}}{N_{\text{generated (total)}}}. \tag{4.20}$$

Figure 4.33 illustrates the dependence of the proton detection efficiency of the TACTIC time-projection chamber (TPC) for the $^{14}\text{N}(\alpha, p)^{17}\text{O}$ reaction on the applied pad-multiplicity cut. For the loosest selection, corresponding to a low multiplicity threshold, the efficiency reaches its maximum value of a few percent (approximately 4%). As the multiplicity requirement is increased, the efficiency decreases rapidly, falling below 1% for multiplicity cuts around six pads and approaching zero for thresholds above roughly ten pads.

This strong dependence is not governed by the geometrical length of the proton tracks. Although protons are light particles and can traverse relatively long distances in the gas, they are characterized by a low specific ionization (dE/dx). Consequently, protons deposit only a small amount of energy per unit length, often producing signals that activate only a limited number of readout pads. Applying a stringent multiplicity cut therefore preferentially suppresses genuine proton events. In contrast, heavier recoil nuclei generate short but densely ionizing tracks that trigger a large number of pads, resulting in significantly higher detection efficiency under the same selection criteria.

Overall, the steep decline of the efficiency curve emphasizes the intrinsic challenge of detecting lightly ionizing particles such as protons in a gas TPC when event selection relies on pad-multiplicity requirements.

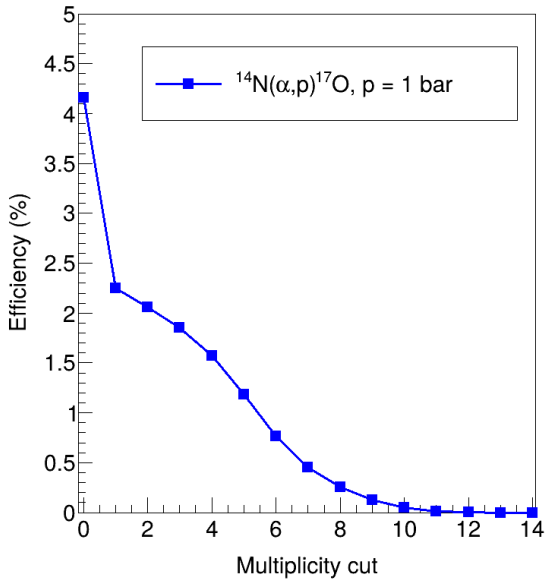

Figure 4.33: The figure illustrate to the detection efficiency of the TACTIC time projection chamber (TPC) for protons from the $^{14}\mathrm{N}(\alpha, p)^{17}\mathrm{O}$

the figure 4.34 shows the efficiency versus multiplicity for elastic scattered. The detection efficiency for elastic α-particles in the $^{14}\mathrm{N}(\alpha, \alpha)^{14}\mathrm{N}$ channel is naturally high, primarily because α-particles produce dense ionization and long tracks that span many detector pads. Unlike protons, their tracks consistently exceed the pad thresholds, meaning that most α-particle events are successfully recorded even when strict multiplicity cuts are applied. The combination of favorable geometry, strong energy deposition, and widespread pad activation results in detection efficiencies typically ranging from 60% to 80%. This behavior clearly illustrates the fundamental difference in detection signatures between heavier, highly ionizing particles and lighter, weakly ionizing ones, emphasizing why α-particle tracks are much easier to detect in a gas TPC.

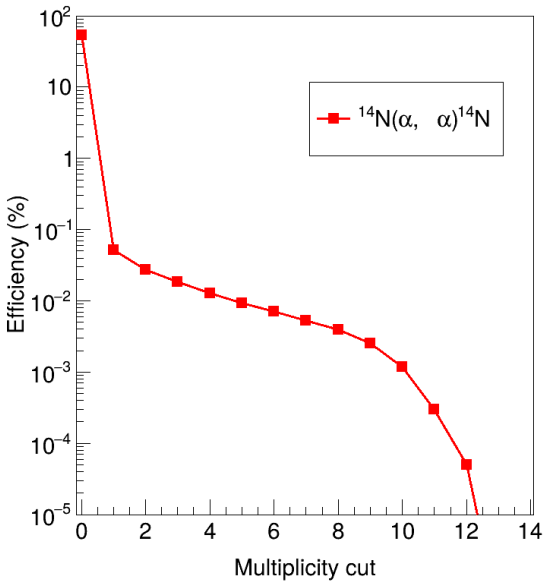

Figure 4.34: The figure shows the efficiency versus multiplicity for elastic scattered. The detection efficiency for elastic α-particles in the $^{14}\mathrm{N}(\alpha,\alpha)^{14}\mathrm{N}$ channel is naturally high

In order to calculate the reaction cross section for the reaction $^{14}\mathrm{N}(\alpha,p)^{17}\mathrm{O}$, the cross section represents as

$$Y = N_b N_t \, \sigma \, \varepsilon \tag{4.21}$$

Here, N_b represents the beam intensity, Y is the proton yield within a specific vertex position (z) range, ε is the detection efficiency, σ is the cross section, and N_t is the target density. The target density was assumed constant during the experimental period, as the gas flow remained stable throughout the run.

The vertex positions are considered here, corresponding to depth points obtained from the simulation, with evenly spaced ranges between consecutive points. The cross section for run 75 was calculated using (1.1) and the values in Table 4.2. Simultaneously, the centre-of-mass energy was determined by converting the beam energy from the laboratory frame using the appropriate kinematic equations.

$$E_{\mathrm{cm}} = E_b \cdot \frac{m_t}{m_t + m_p} \tag{4.22}$$

where : m_t is mass for the target, m_p mas for the projectile in amu. E_{cm} is the vertex energy in the center of mass farm.

The value of E_{cm} from the equation above 4.22 listed in table down in table 4.3, and need to identify the energy threshold for the reaction reliability.

Table 4.3: Conversion of beam energy E_b to center-of-mass energy E_{cm}.

E_b (MeV)	E_{cm} (MeV)
10.54	2.342222
9.25	2.055556
7.99	1.775556
6.69	1.486667
5.40	1.200000
4.11	0.913333
2.83	0.628889
1.53	0.340000
0.45	0.100000
0.00	0.000000

The energy threshold is closely related to the point at which the experimental data become reliable. A sensible choice of the threshold requires removing the near-zero energy region, where the measurements are dominated by noise and detector limitations, while retaining the higher-energy region where the reaction is clearly observable. As shown in Fig. 4.36, two distinct energy regions can be identified.

In the low-energy region, $E_{\mathrm{cm}} \lesssim 0.34$ MeV, corresponding to energies close to the reaction threshold, the available kinetic energy is comparable to or smaller than the experimental resolution. In this regime, the reaction yield is strongly suppressed and highly sensitive to background contributions. Consequently, measurements in this energy range are not considered reliable. This region corresponds to a beam energy of approximately $E_b \approx 1.53$ MeV.

Above this value, $E_{\mathrm{cm}} > 0.34$ MeV (or equivalently $E_b \approx 1.53$ MeV), the reaction becomes kinematically allowed and the data exhibit a more stable and approximately linear behavior. This region represents the onset of physically meaningful measurements.

At higher energies, a further data separation is observed for $E_{\mathrm{cm}} > 1.2$ MeV, corresponding to a beam energy of $E_b \approx 5.40$ MeV. In this range, low-energy systematic effects are significantly reduced, making it particularly suitable for quantitative analysis.

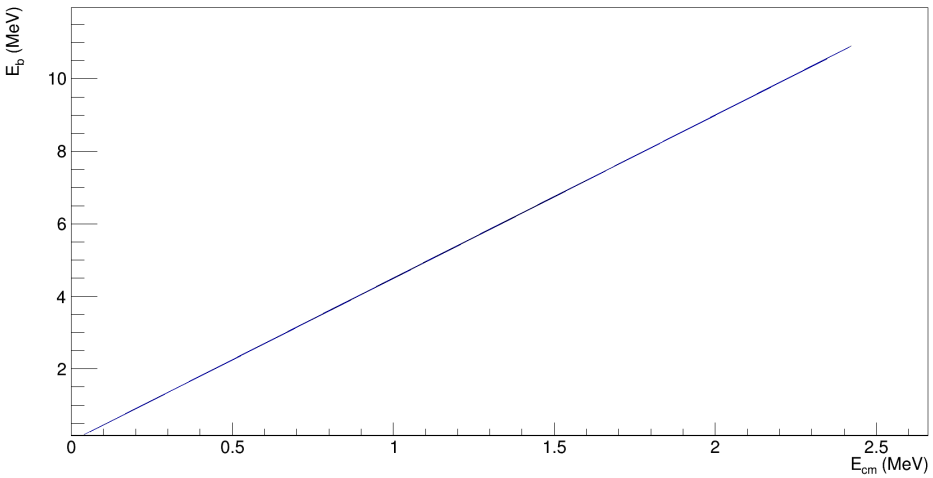

Figure 4.35: The figure shows the Beam energy as a function of centre of mass energy

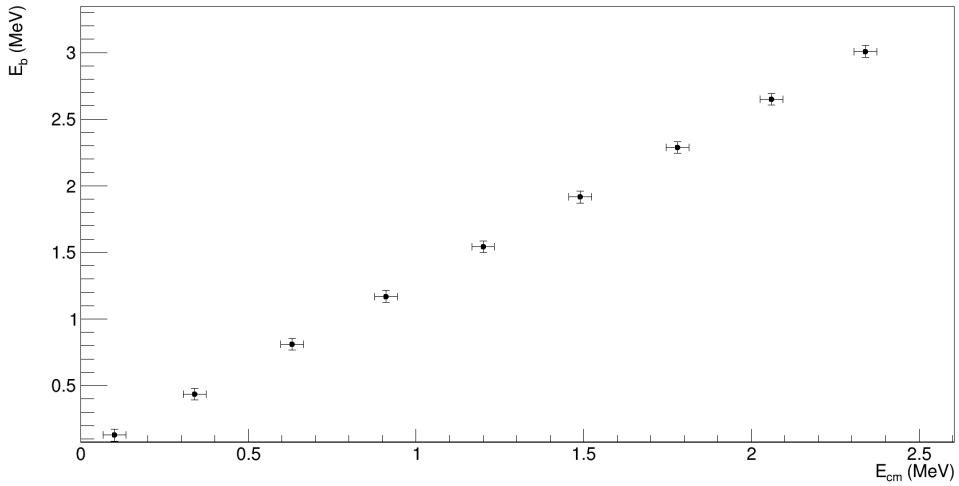

Figure 4.36: The figure shows the Beam energy as a function of center of mass energy error bars

Since the measured yield corresponds to detected protons, the observed reaction channel is $^{14}\mathrm{N}(\alpha,p)^{17}\mathrm{O}$. The yield is approximately constant at low centre-of-mass energies E_{cm}, indicating a background or baseline level, and begins to increase significantly around $E_{\mathrm{cm}} \approx 1.5$ MeV, marking the onset of a strong (α,p) contribution as showing the figure below 4.38. The figure 4.37 shows the uncertainties of yield and proving that the reaction occurs but not just kinematic.

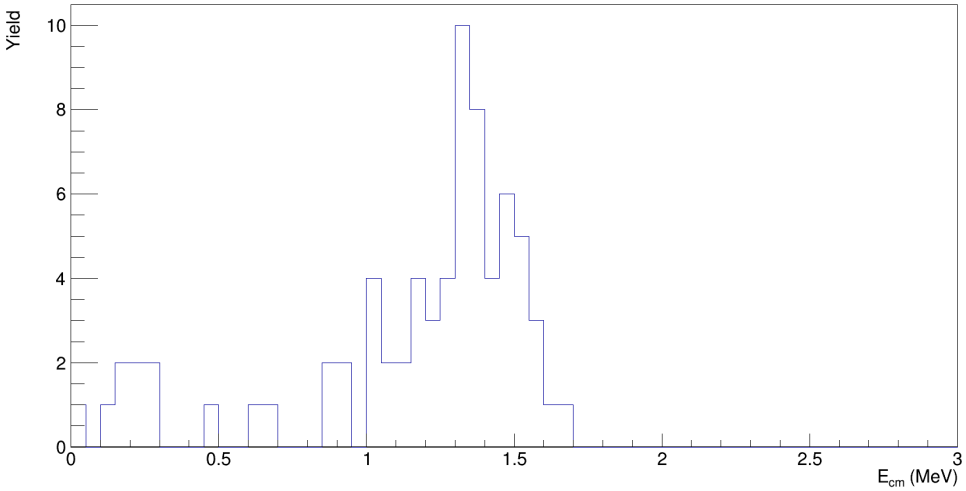

Figure 4.37: The figure shows the yield as a function of centre of mass energy

However, below 1.5 Mev the points overlap with uncertainties and yield consistent with a constant baseline . A real increase in reaction probability begins at $E_{\mathrm{cm}} \approx 1.5$ MeV and this refers to strong energy dependence of cross section and the yield refer to the proton yield. For the calculation of Error bar we use Poisson counting statistics, and the statistical uncertainty is expressed as

$$\sigma \approx \sqrt{N} \tag{4.23}$$

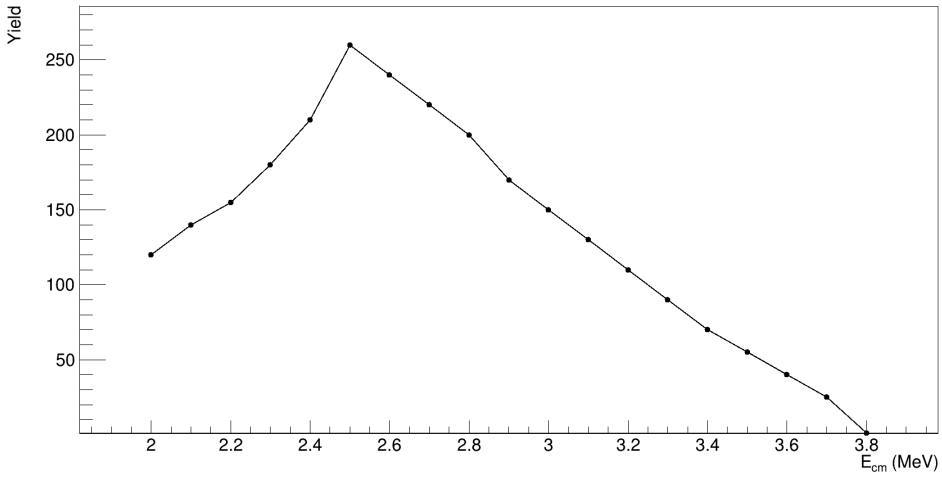

Figure 4.38: The figure shows the yield as a function of centre of mass energy

At center-of-mass energies below 1.5 MeV, the number of detected protons remains constant within the measurement uncertainties. This indicates that there is no clear evidence of the reaction in this energy range. Above approximately 1.5 MeV, the proton yield increases noticeably, showing that the reaction becomes significant in the $^{14}\mathrm{N} + \alpha$ system.

The figure down 4.39 show the relation between yield and selected vertex position by using Hauser - Feshbach cross section, Every center of mass energy calculated by determined beam energy and different and selected depth z in the target, and the corresponding Hauser–Feshbach cross section is used to identify the reaction probability. However, yield correspond to different vertex position due to the combined effects of energy loss in the target, the energy dependence of the theoretical cross section, and the vertex-dependent detector acceptance.

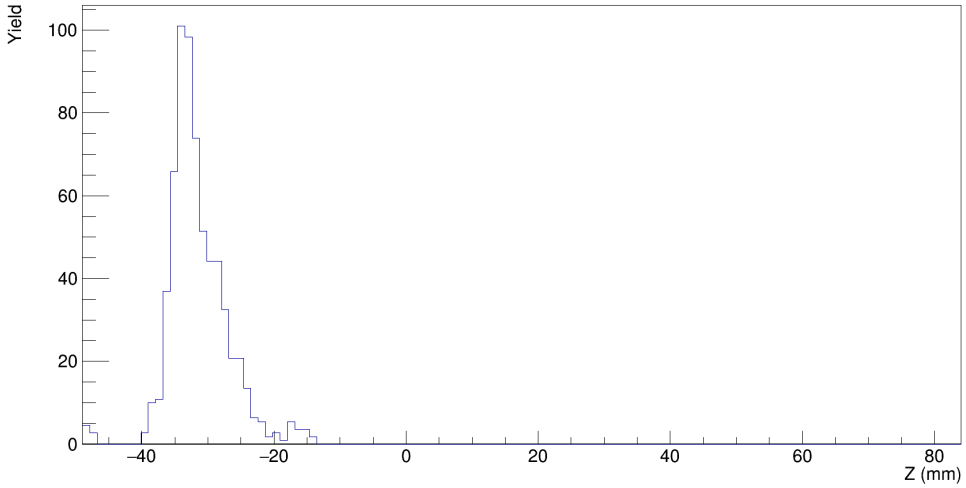

Figure 4.39: The figure shows the calculated proton yield at different selected vertex position by using Hauser - Feshbach cross section and experimental parameters from the table 4.2

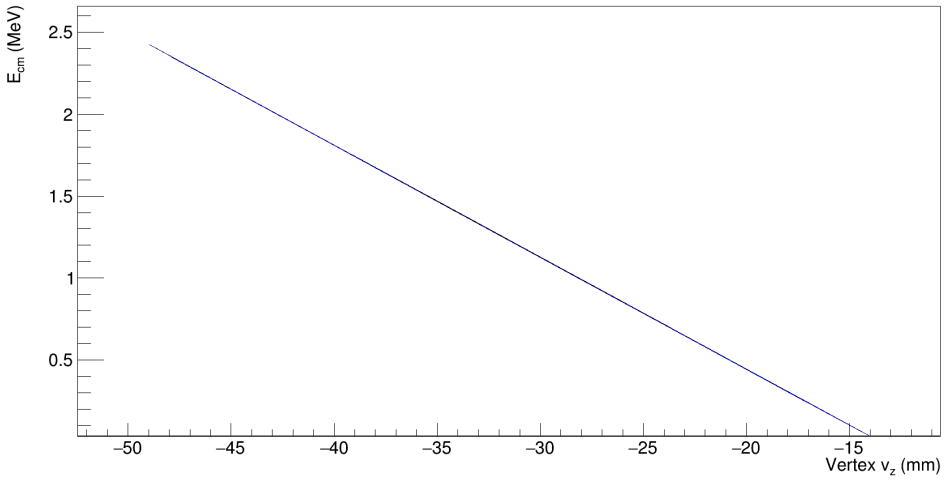

Figure 4.40: This figure shows the relation between the center-of-mass energy and the selected vertex position for the reaction $^{14}\mathrm{N}(\alpha,p)^{17}\mathrm{O}$.

From the figures 4.38, 4.37, 4.39 shows The proton yield as a function of centre-of-mass energy indicates that the $^{14}\mathrm{N}(\alpha,p)$ reaction exhibits a pronounced increase above $E_{\mathrm{cm}} \approx 1.5$ MeV. When expressed as a function of vertex position, the yield shows the same trend projected onto the target geometry, since variations in the vertex location correspond to changes in the effective centre-of-mass energy caused by beam energy loss in the target. Consequently, vertex regions with higher yield correspond to energies where the reaction cross section is enhanced.

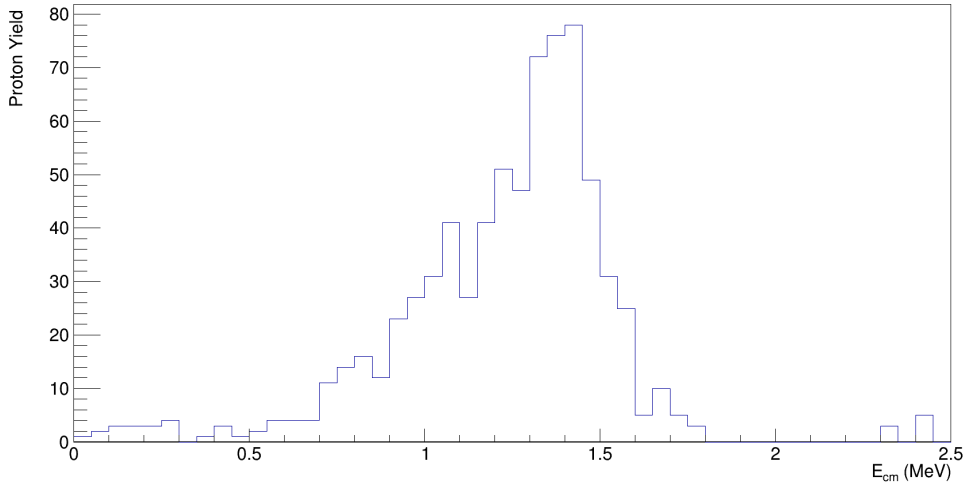

Figure 4.41: This figure shows the proton cross section versus center-of-mass energy for the reaction $^{14}\mathrm{N}(\alpha,p)^{17}\mathrm{O}$ for run 75.

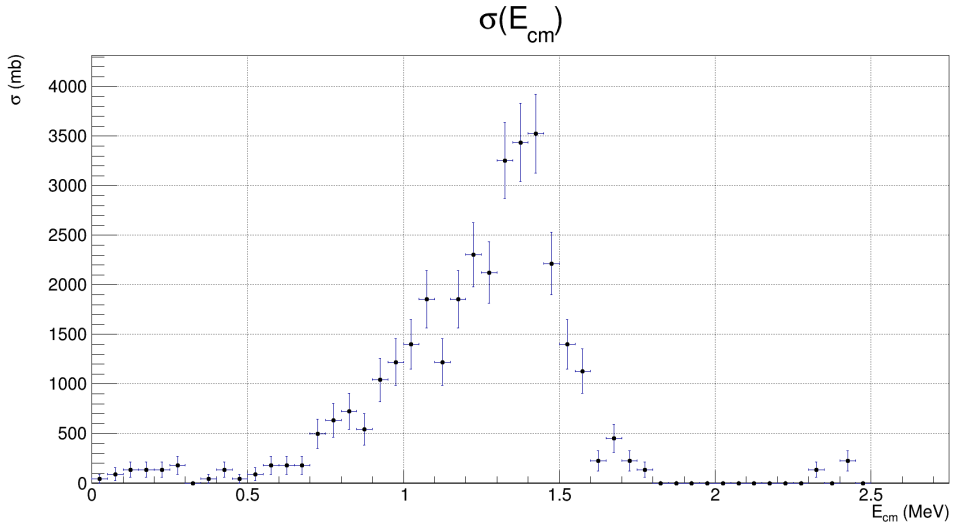

Figure 4.42: The figure shows the errors cross section as a function of centre of mass energy

The proton cross section extracted as a function of centre-of-mass energy provides a clear interpretation of the measured yield behavior. At low E_{cm}, the cross section remains small and, within uncertainties, shows no significant variation, indicating that the observed proton yield in this region is largely dominated by background contributions rather than the reaction of interest. As the centre-of-mass energy increases beyond approximately 1.5 MeV, the cross section rises noticeably, demonstrating that the corresponding increase in proton yield is driven by a genuine enhancement of the $^{14}\mathrm{N}(\alpha,p)^{17}\mathrm{O}$ reaction probability. This energy dependence naturally explains the vertex-dependent yield distribution, since vertex positions associated with higher effective centre-of-mass energies sample regions where the reaction cross section is larger.

4.0.9 Results for runs(84 to 90)

Following the previous analysis and results, with different conditions applied in pressure and voltage as shown in the table down 4.4, The reconstructed track radius in a gas detector depends strongly on the operating pressure and the applied high voltage, since these parameters control the electron drift velocity, diffusion, and gas amplification. Variations in the reduced electric field E/P can modify the drift and amplification properties of the gas, leading to systematic shifts in the reconstructed hit positions. As a consequence, the measured track curvature may change.

Parameters	^{4}He : CO_2 90:10
Pressure	0.5 bar
Drift voltage	-1400 volt

Table 4.4: Experimental details for stable beam group runs 84 to 94

According to the simulation, the in beam loses energy when pass through the window and was calculated (3.1 MeV), while the rest (10.9 MeV) for ^{14}N reacted with the target. A linear equation for the figure 4.24 expressed down as an energy lose as a function of target depth in

TACTIC's geometry

$$-126 \leq z(\text{mm}) \leq 126$$

$$E_b = 25.218 - 6.4637\,Z \tag{4.24}$$

and

$$\Delta E_b = -6.4637\,\Delta Z \tag{4.25}$$

The linear equation above is valid for beam energies in the range $0.2 \leq E_b\ (\text{MeV}) \leq 10.9$. For the analysis, only energies above 0.2 MeV were considered, since simulations and GEANT4 become inaccurate outside this range. This energy interval also corresponds to the region of interest for the $^{14}\text{N}(\alpha, p)^{17}\text{O}$ reaction.

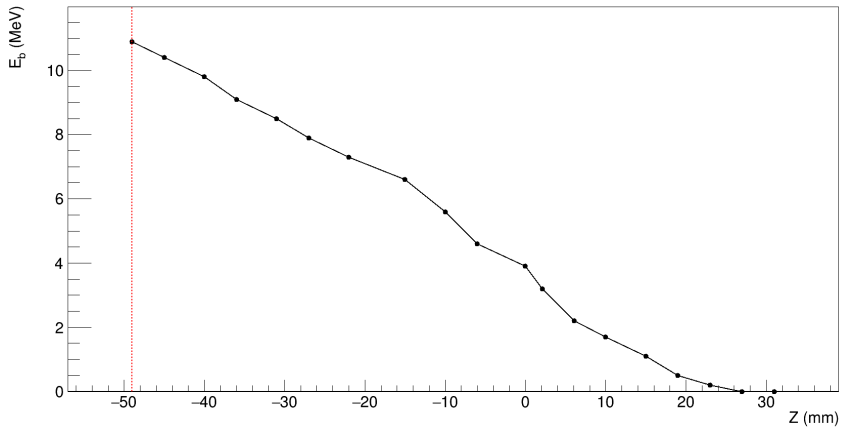

Figure 4.43: The beam energy loss in the gas target as a function of vertex (depth), data from simulation

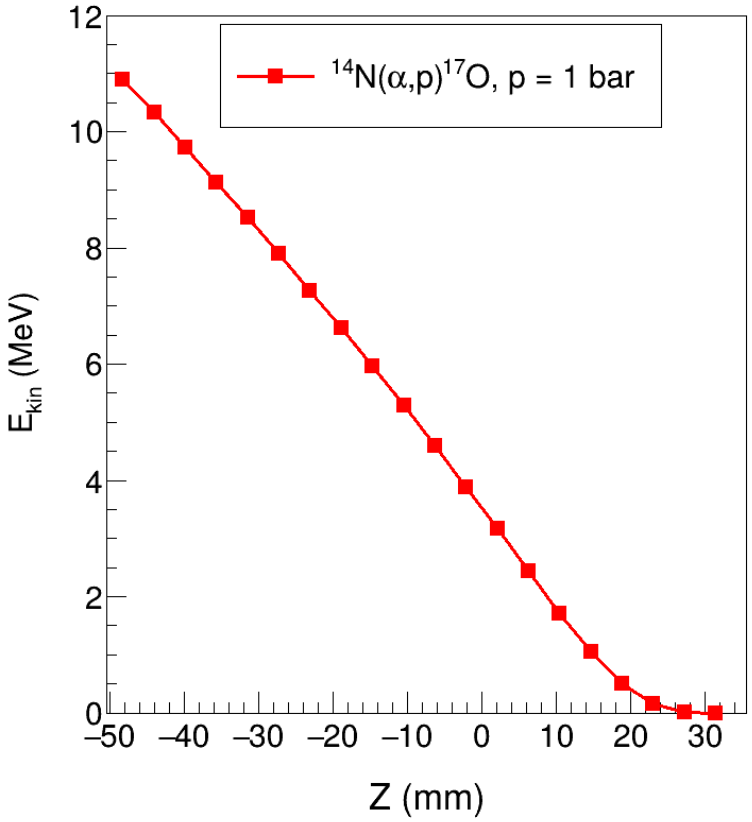

Figure 4.44: The beam energy loss in the gas target as a function of vertex (depth), simulation. Note the 1 bar in the plot is 0.5bar it is made by mistake [7]

Since the beam energy varies linearly with the reconstructed vertex position, its uncertainty was estimated using standard error propagation,

$$\sigma_{E_b} = \left|\frac{dE_b}{dZ}\right| \sigma_Z = 6.4637\,\sigma_Z, \tag{4.26}$$

where σ_Z is the uncertainty associated with the reconstructed vertex position. The statistical uncertainty of the mean vertex position was determined to be approximately 0.427 mm.

The beam energy, E_b, was determined from the reconstructed interaction vertex position, Z, obtained from the detector tracking information along the beam axis. After applying the standard event selection criteria, the distribution of the reconstructed vertex positions was examined.

The mean vertex position was found to be

$$\langle Z \rangle = -19.42 \pm 0.43 \text{ mm},$$

where the quoted uncertainty represents the statistical uncertainty of the mean, calculated from the RMS of the distribution divided by the square root of the number of selected events.

The reconstructed vertex position was then converted to the corresponding beam energy using the linear calibration

$$E_b\ [\mathrm{MeV}] = 25.218 - 6.4637\,Z\ [\mathrm{mm}],$$

where the calibration coefficients were obtained independently. This calibration was applied on an event-by-event basis to determine the beam energy at the reaction vertex while accounting for the energy loss of the beam in the target gas. The reconstructed beam energies were subsequently used throughout the analysis.

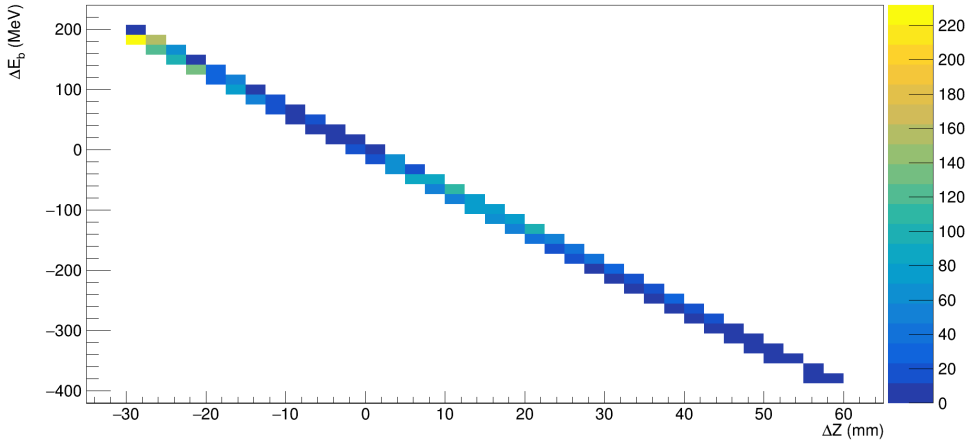

Figure 4.45: The uncertainty of the beam energy loss in the gas target as a function of vertex (depth)

The figure 4.47 shows the end track for particles terminated at μ-Rwell for the stable beam group runs 84 to 90. The figure shows all the shallower stopped in the detection area in a downstream (z= 30 mm) or been shielded by cathode cage, while the majority of the track terminated at μ-Rwell ($r \approx 50\,\mathrm{mm}$). Those tracks correspond to the (α,α) and (α,p) scattering and reaction channels. The (α,α) channel represents ^{4}He is a scattered particle at the window due to interactions with the beam. The heavier products like ^{14}N and ^{17}O stop completely in the detection area or can be shielded totally by the cathode cage at ($r \approx 50\,\mathrm{mm}$). With the conditions been selected as $m_{\mathrm{track}} \geq 4$, $c_{\mathrm{track}} = 1$ so the only elements terminated at μ-Rwell will be selected further to eliminate the majority of the elastic scattering products from the target gas and entrance window, as well as to improve the quality of vertex reconstruction, while in the same time this will reduce the detection efficiency for the (α,p) reaction channel. The above uncertainties in the beam energy led us to one of the important parameter which is called the energy resolution which comes from vertex as following, the beam energy is not measured directly on an event-by-event basis but is instead inferred from the reconstructed interaction vertex position along the beam axis. Owing to the extended nature of the gas target, the beam loses energy continuously as it traverses the target, resulting in a well-defined correlation between the interaction vertex position Z and the beam energy at the reaction point. This correlation is described by a linear calibration, from which the corresponding center-of-mass energy can be derived.

To study the impact of energy smearing near the reaction threshold in a controlled manner, the analysis was performed locally by selecting narrow slices of the reconstructed vertex position. For a given slice centered at Z_0, all events with reconstructed vertices in the interval $Z_0 \pm w$ were selected, where w denotes the half-width of the slice. Within such a narrow region, the variation of the beam energy with Z can be accurately approximated as linear.

For each selected event, the deviation of its center-of-mass energy from the mean energy at the slice center was defined as

$$\Delta E_{\mathrm{cm}} = \left(\frac{dE_{\mathrm{cm}}}{dZ} \right) (Z - Z_0), \tag{4.27}$$

where $\frac{dE_{\mathrm{cm}}}{dZ}$ is obtained from the vertex–energy calibration. By construction, $\Delta E_{\mathrm{cm}} = 0$ corresponds to the center-of-mass energy at the reference position Z_0, while positive or negative values indicate events reconstructed at higher or lower effective energies, respectively.

The resulting ΔE_{cm} distribution therefore represents the local energy spread of events within the selected vertex slice. In an idealized scenario with perfect vertex reconstruction and no energy straggling, this distribution would collapse to a delta function. In practice, however, several experimental effects contribute to a finite width, including the intrinsic vertex reconstruction uncertainty, the finite spatial extent of the selected slice, and energy straggling of the beam in the gas target.

The ΔE_{cm} spectrum obtained for the slice centered at $Z_0 = -27$ mm exhibits a localized peak at positive ΔE_{cm}, which is identified as the signal component. This peak is well described by a Gaussian function, whose width provides a quantitative measure of the effective energy smearing in the vicinity of the threshold. The extracted full width at half maximum of 1.44 MeV (corresponding to $\sigma = 0.61$ MeV) reflects the combined effect of vertex reconstruction and target-related broadening.

In addition to the signal peak, the distribution also contains a broader population extending toward negative ΔE_{cm} values. These events arise from a combination of residual background, vertex mis-reconstruction, and non-Gaussian tails associated with energy straggling and reconstruction imperfections. Since these events do not follow the same energy–vertex correlation as the signal, they are not interpreted as part of the physical signal and are excluded from the determination of the energy resolution.

The measured width of the signal peak directly quantifies the effective center-of-mass energy resolution relevant for threshold studies. This finite resolution implies that events with true energies above the reaction threshold can be reconstructed at energies slightly below threshold, leading to a non-zero observed yield in that region. Consequently, the presence of yield close to or slightly below the nominal threshold can be fully explained by experimental energy-smearing effects and does not indicate the existence of a physical reaction below threshold.

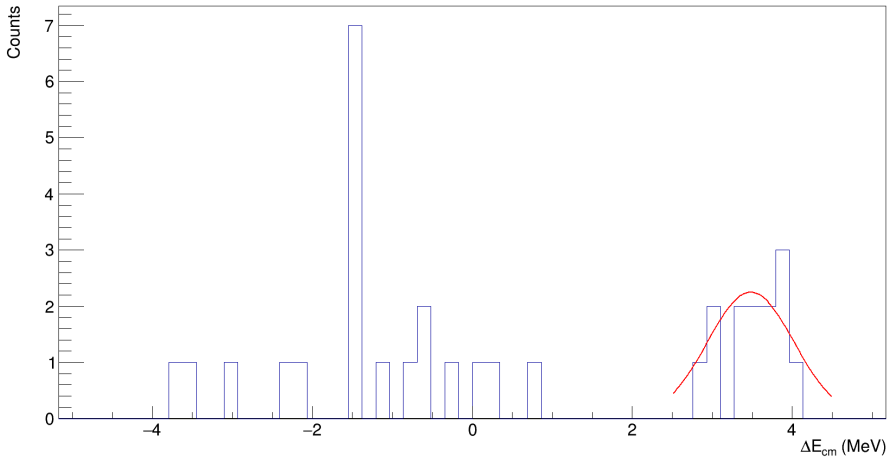

Figure 4.46: Distribution of the reconstructed center-of-mass energy deviation ΔE_{cm} for events selected within the vertex slice $Z_0 \pm 3$ mm centered at $Z_0 = -27$ mm. The quantity ΔE_{cm} is defined relative to the center-of-mass energy at the reference vertex position Z_0 using the linear vertex–energy calibration. The localized peak at positive ΔE_{cm} corresponds to the signal component and is fitted with a Gaussian function (red curve). The extracted width of the peak, FWHM $= 1.44$ MeV ($\sigma = 0.61$ MeV), quantifies the effective center-of-mass energy smearing arising from vertex reconstruction, the finite spatial extent of the target, and energy straggling in the gas. The broader population at negative ΔE_{cm} originates from residual background and reconstruction effects and is not included in the determination of the energy resolution.

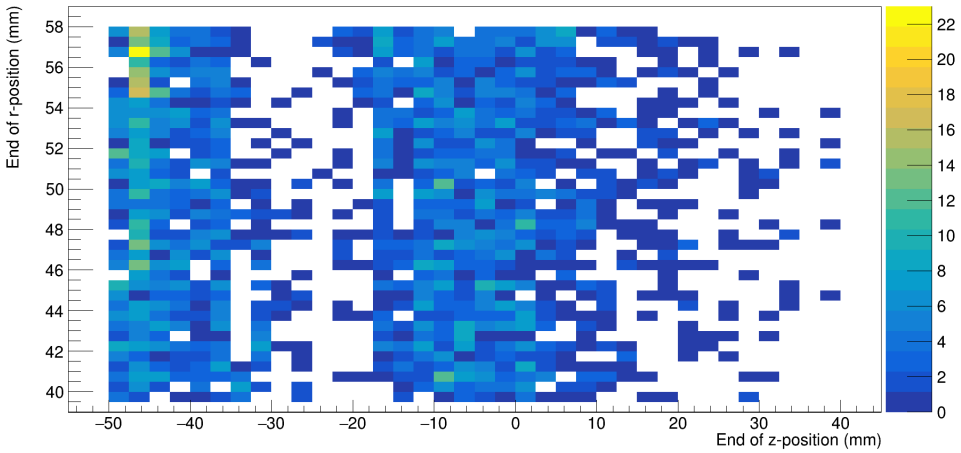

Figure 4.47: The end points of tracks from stable beam runs 84,85,86,87,88,89,90. The entrance window was positioned at z= -49 mm , and data cuts Data cuts used: $2.5 < ttimecheck3 \leq 4$ μs, $r_d > 5$ mm, $m_{\mathrm{track}} \geq 4$, $c_{\mathrm{track}} = 1$.

Figure 4.48 shows the reconstructed vertex distribution along the beam axis. The first increase shows the distribution of the beam at the entrance window position which followed by the decrease of the yield till to reach (-20 mm), this decrease reflect to two reasons : the first one correspond to the centre of mass energy, $E_{\mathrm{cm}} \approx 2.5\,\mathrm{MeV}$, which was calculated from the equation 4.22. The significant decrease in yield refers to a steep drop in the reaction cross section (α, p) in the point $E_{\mathrm{cm}} \approx 1.2\,\mathrm{MeV}$ as well as a lower energy of the elastic scattering

interactions, leading to a decrease in the efficiency of the proton.

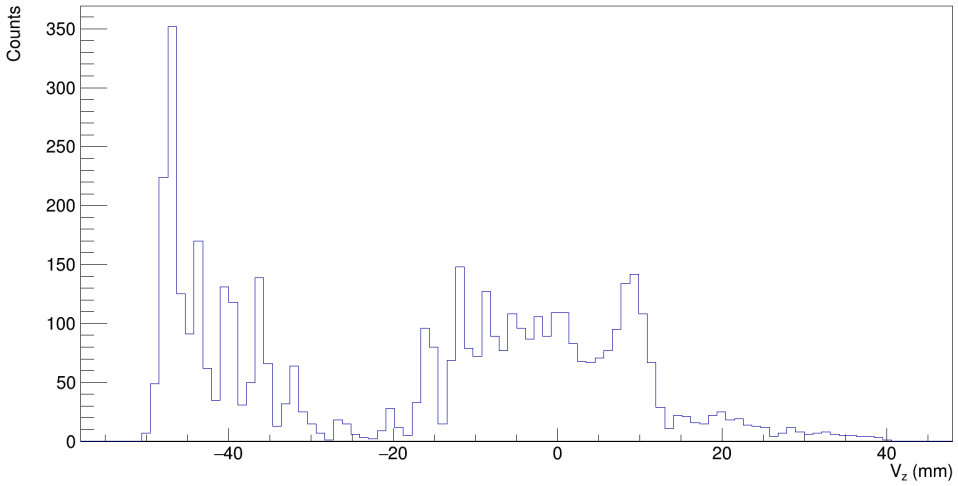

Figure 4.48: The reconstructed vertices for the stable beam runs 84,85,86,87,88,89,90. The entrance window was positioned at z= -49 mm , and data cuts Data cuts used: $2.5 < ttimecheck3 \leq 4$ μs, $r_d > 5$ mm, $m_{\text{track}} \geq 4$, $c_{\text{track}} = 1$.

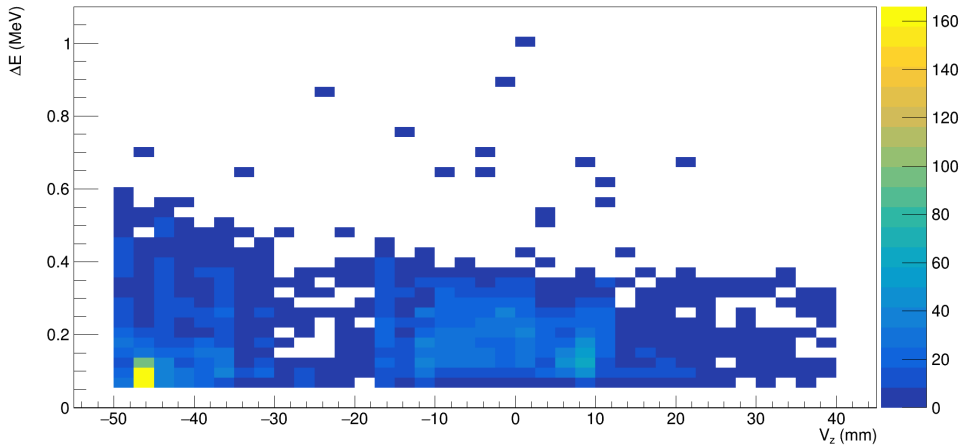

Figure 4.49: The figure shows the deposited energy as a function of vertex at selected cuts z= -49 mm , and data cuts Data cuts used: $2.5 < ttimecheck3 \leq 4$ μs, $r_d > 5$ mm, $m_{\text{track}} \geq 4$, $c_{\text{track}} = 1$.

Figure 4.49 shows the maximum energy deposited as a function of the vertex position. It provides a clear explanation for the second increase and the higher peak observed in Figure 4.48. The region between $V_z = -20$mm and $V_z = 40$mm shows the elements with higher energy terminated at μRwell those elements which are heavier then proton could refer to alpha particles as they have higher energy.

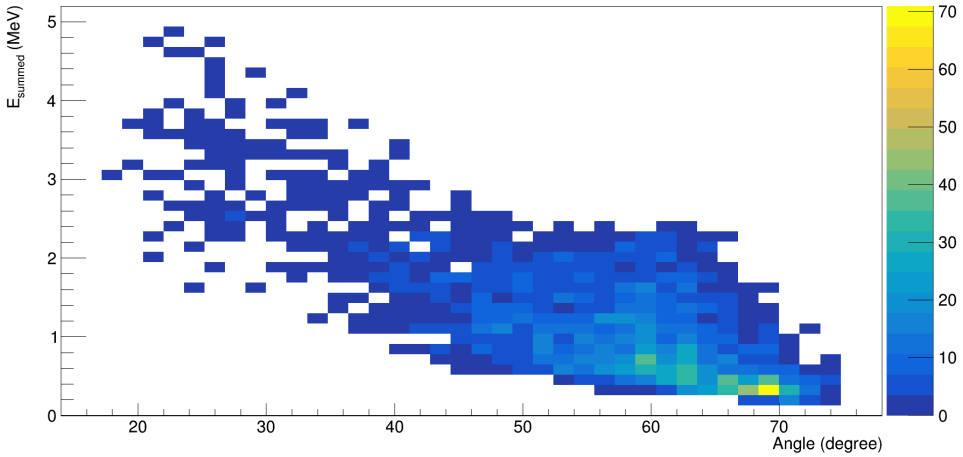

Figure 4.50: The figure shows the total energy versus track angle at the selected cuts $z = -49$ mm. Data cuts used: $2.5 <$ ttimecheck3 ≤ 4 μs, $r_d > 5$ mm, $m_{\text{track}} \geq 4$, $c_{\text{track}} = 1$.

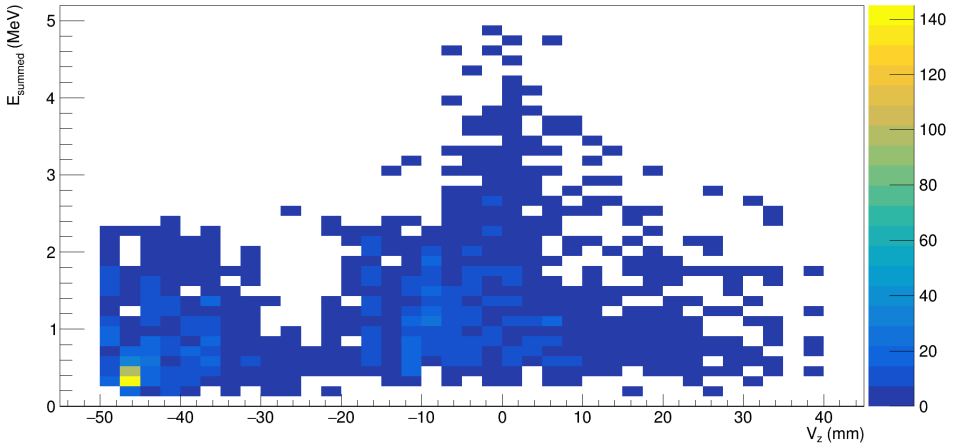

Figure 4.51: The figure shows the distribution of the total energy versus vertex at the selected cuts $z = -49$ mm. Data cuts used: $2.5 <$ ttimecheck3 ≤ 4 μs, $r_d > 5$ mm, $m_{\text{track}} \geq 4$, $c_{\text{track}} = 1$.

The figures above 4.51and 4.50 show the range of the total energy distribution over track angles and vertices. The figure shows more elements hits the μ-Rwell focused between 60°–70° which is in agreement with the vertices and deposited energies at the same range.

To identify the nature of those elements and particle we followed the standard way depends on the distribution of ΔE–E as shown in the figure 4.52 down and with getting benefits from the simulation 4.54 noticed that from the experimental data, a detectable energy range of 0.25-1 Mev per pad was identified. Otherwise, a comparison between the simulation and experimental figures and results revealed that most of the above this range events could refereed either protons or scattered alphas.

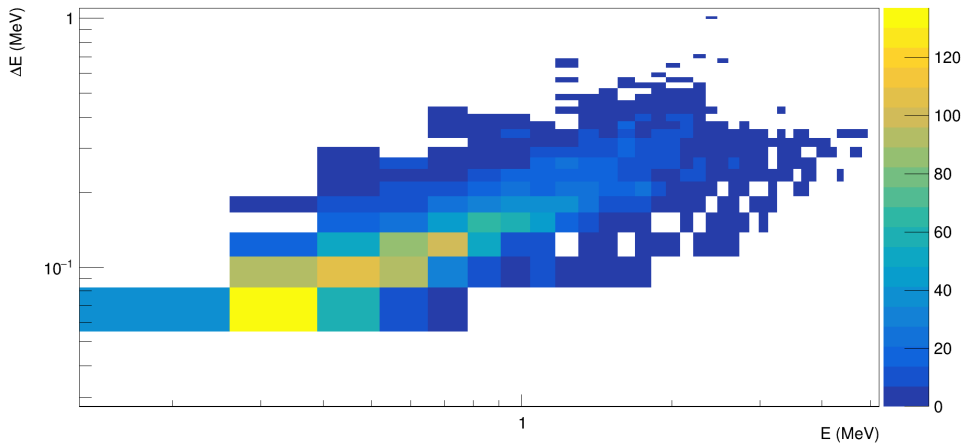

Figure 4.52: The figure shows the total deposited energy in each pad versus total energy at the same cuts applied, z= -49 mm , and data cuts Data cuts used: $2.5 < ttimecheck3 \leq 4$ μs, $r_d > 5$ mm, $m_{\text{track}} \geq 4$, $c_{\text{track}} = 1$.

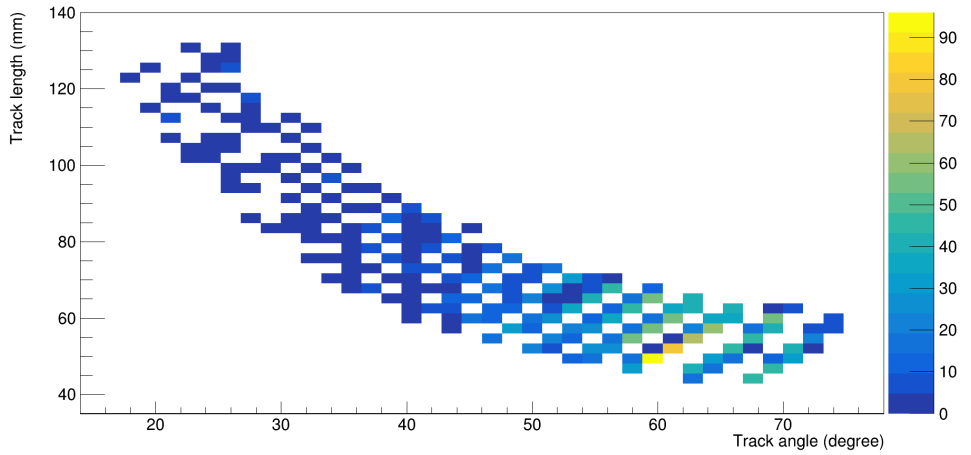

Figure 4.53: The figure shows the relation of the track length vs track angle with the same conditions applied, z= -49 mm , and data cuts Data cuts used: $2.5 < ttimecheck3 \leq 4$ μs, $r_d > 5$ mm, $m_{\text{track}} \geq 4$, $c_{\text{track}} = 1$.

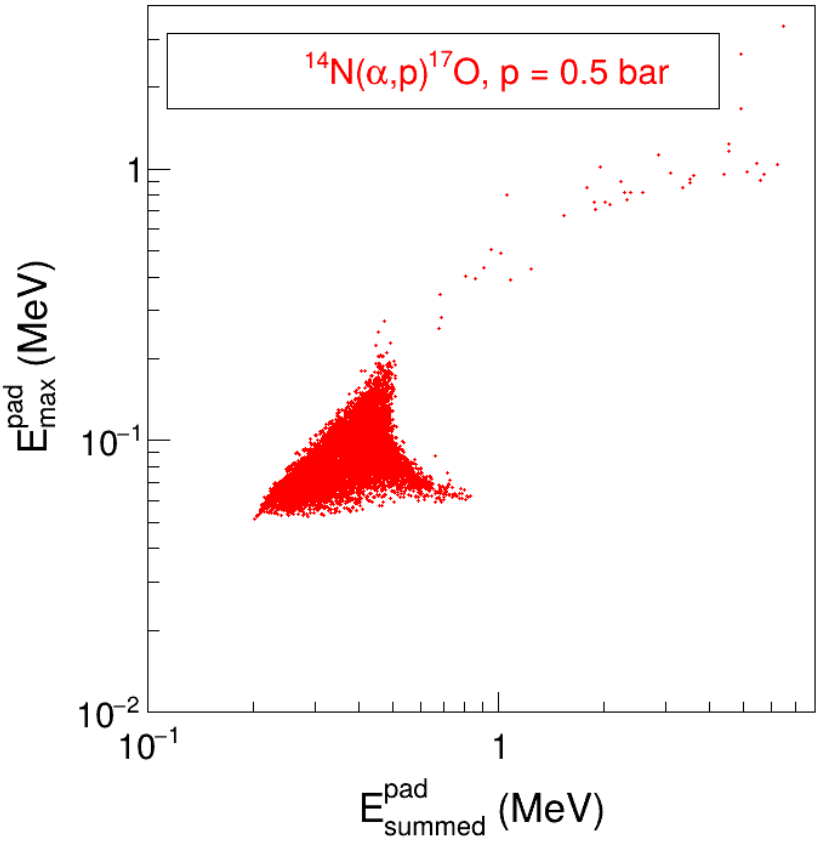

Figure 4.54: The figure Emax vs Esummed shows the simulated and clear proton energy cuts in the reaction $^{14}\mathrm{N}(\alpha, p)^{17}\mathrm{O}$ at 0.5 bar

The figure 4.53 above shows the distribution between the track length as a function of the track angle for different reaction and scattering products. As noticed and shown in the figure, the protons and alphas were predicted to have a long track lengths comparing to the heavier products and the majority of them to reach the μ-Rwell. Additionally, distinguishing proton from alphas is kinematically variable under the conditions applied and after the selection of tracks that reach the μ-Rwell. The heavy recoils such as ^{17}O from the reaction scattered beam particles ^{14}N was not included in this plot as it will be fully shielded by the cathode cage or be stopped inside the detection area or even caused saturation at the digitiser as a result of high differential energy loss in the gas.

The proton reaction for the distribution ΔE–E in the range 0.25 KeV - 1 MeV shows no and sub-distribution as it shown clearly in the figures down 4.55 and 4.56. While showing no any electronic noise. The steeper proton track ($\Delta E < 0.25\,\mathrm{MeV}, \quad \theta > 64^{\circ}$) that terminate at μ-Rwell were found to deposit higher energy per pad.

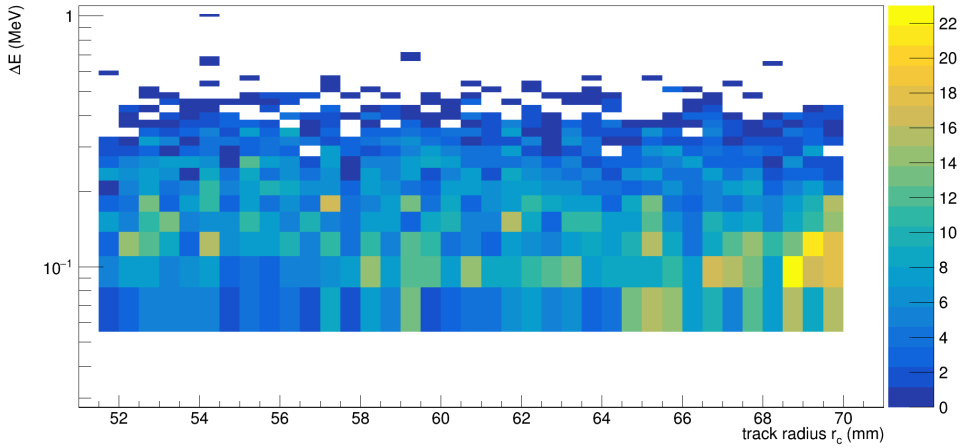

Figure 4.55: The figure shows the relation between total energy deposited in each track as a function of the track radius with the same conditions and cuts z= -49 mm , and data cuts Data cuts used: $2.5 < ttimecheck3 \leq 4$ μs, $r_d > 5$ mm, $m_{\text{track}} \geq 4$, $c_{\text{track}} = 1$.

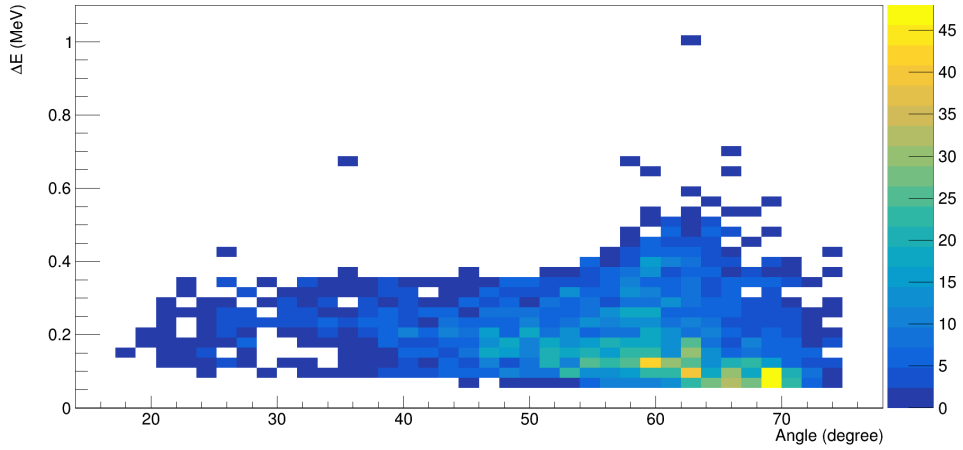

Figure 4.56: the figure shows the total energy deposited in track as a function of the track angle with the same conditions z= -49 mm , and data cuts Data cuts used: $2.5 < ttimecheck3 \leq 4$ μs, $r_d > 5$ mm, $m_{\text{track}} \geq 4$, $c_{\text{track}} = 1$.

4.0.10 $^{14}\text{N}(\alpha, p)^{17}\text{O}$ Reaction cross section measurements for group runs 84-90

The above discussion for the particle identification was used to identify the proton cross section for the reaction $^{14}\text{N}(\alpha, p)^{17}\text{O}$ at different and selected vertices as shown the figure 4.43. The table 4.5 shows the the parameters from the inelastic scattering arises for ^{1}H only. Moreover, it could be noticed that the heavy element could be shielded for the cathode cage or stopped in the detection aria. The measurement of the proton cross section is strongly depend on the detection efficiency of the reaction proton itself. The proton yield was calculate by using the theoretical Hauser -Feshbach cross section. In comparison with the previous total vertex distribution , the proton yield observed in the distribution corresponding to the proton reaction in the region Z < -20 (mm) as the region after -20 (mm) refers to the other particles distribution.

Parameter	Value
Beam intensity	9.5×10^5 pps
Run time	23 min
Target thickness	0.5 cm
Target density	5.55×10^{18} atoms cm^{-3}
Target composition	He:CO_2 90:10
Proton detection efficiency	0.8%

Table 4.5: Experimental details for stable beam run 84 to 90 the simulated proton detection efficiency listed here was taken from the simulation's calculated by Julien, taking into consideration, an energy threshold of 50 keV per pad.

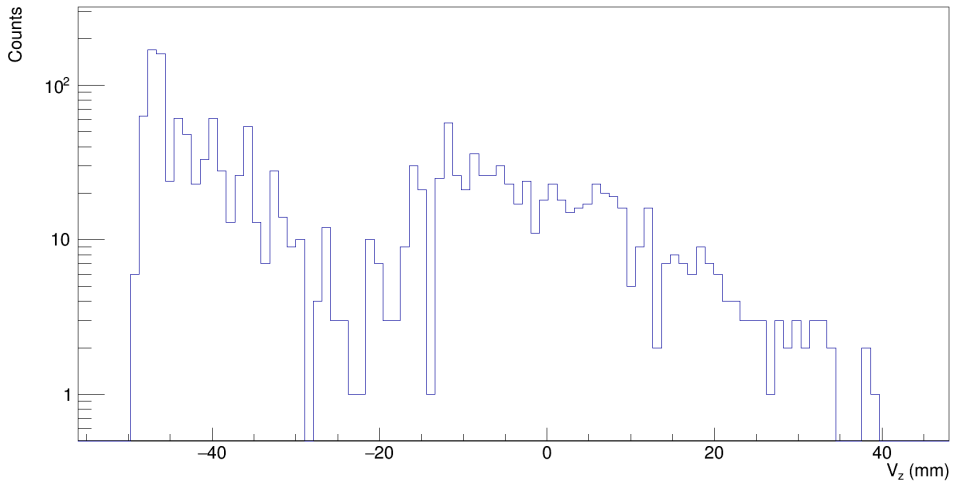

Figure 4.57: The proton yield distribution as a function of vertex for the above cuts z= -49 mm , and data cuts Data cuts used: $2.5 < ttimecheck3 \leq 4$ μs, $r_d > 5$ mm, $m_{\text{track}} \geq 4$, $c_{\text{track}} = 1$, E < 1 Mev

In order to obtain the proton cross section, the total proton detection efficiency need to be calculated and that happens by simulation [7] and It was found to be 0.8%, decreasing from 1.6%, which is attributed to the reduction in pressure and voltage.

The figure 4.57 gives a clear information about the distribution of the proton yield over vertices, while the tables 4.5 and 4.6 are giving us the full information about the paraments and values of the cross section at selected points (selected points comes from the simulated beam energy). Since the interaction probability depends on the reaction cross section at the local beam energy, the measured yield as a function of the interaction vertex position can be expressed as

$$Y(z) = N_t N_p \varepsilon \sigma(z), \tag{4.28}$$

where N_t is the target areal density, N_p is the integrated beam flux, ε is the proton detection efficiency, and $\sigma(z)$ is the reaction cross section corresponding to the beam energy at position z. The figure 4.58 shows the observed trend in the cross section as a function of vertex position reflects how the probability of the $^{14}\text{N}(\alpha, p)^{17}\text{O}$ reaction changes with energy.

- Negative z values correspond to higher beam energies and higher E_{cm}.

Table 4.6: Proton yield and cross section as a function of vertex position and center-of-mass energy.

V_z (mm)	E_{cm} (MeV)	Yield (counts)	σ (mb)	E_{b} (MeV)
-49.00	2.42	120	4123.12	10.9
-45.00	2.31	140	4810.30	10.4
-40.00	2.17	155	5325.69	9.8
-36.00	2.02	180	6184.67	9.1
-31.00	1.88	210	7215.45	8.5
-27.00	1.75	260	8933.42	7.9
-22.00	1.60	240	8246.23	7.2
-15.00	1.46	220	7559.05	6.6
-10.00	1.31	200	6871.86	5.9
-6.00	1.17	170	5841.08	5.3
0.00	1.02	150	5153.90	4.6
2.10	0.86	130	4466.71	3.9
6.10	0.71	110	3779.52	3.2
10.00	0.55	90	3092.34	2.5
15.00	0.40	70	2405.15	1.8
19.00	0.24	55	1889.76	1.1
23.00	0.11	40	1374.37	0.5
27.00	0.04	25	858.98	0.2
31.00	0.02	1	34.36	0.1

- Positive z values correspond to lower beam energies and lower E_{cm}.

In the region between -49 mm $\leq z \leq -30$ mm, the cross section increase steady till to reach the peak at z = -30 mm as the vertex moves downstream that refers to the Coulomb barrier penetration becomes more reliable and reaction phase can be more efficiently. In the region $z \approx -30$ to -25 mm, the cross section reaches a maximum corresponding to $E_{\mathrm{cm}} \approx 2.4$–$2.6$ MeV as we will see late in the next graphs, and in the last region the cross section keep decreasing as vertex goes downstream and that refers to some reasons such as decreasing reaction probability as well as reduced available kinetic energy in the exit channel. In the range $z \gtrsim 23$ mm the behaviour represent the consistent with the expected suppression of the (α, p) channel at low energies and does not imply unphysical sub-threshold reactions.

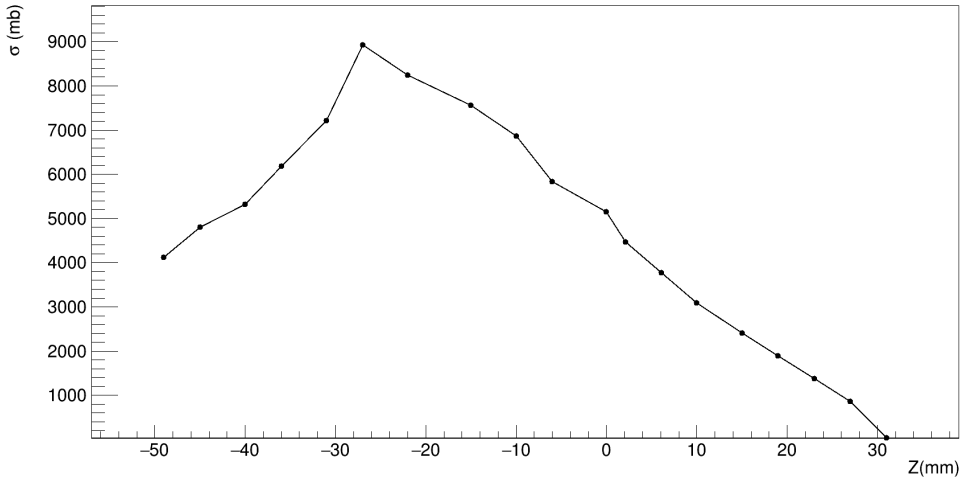

Figure 4.58: The figure shows the proton cross section for the reaction $^{14}\mathrm{N}(\alpha, p)^{17}\mathrm{O}$ as a function of vertex.

The inclusion of statistical uncertainties supports the reliability of the extracted cross section. As expected from Poisson counting statistics, the error bars increase in regions where the yield is low, while the overall shape of the excitation function remains unchanged.

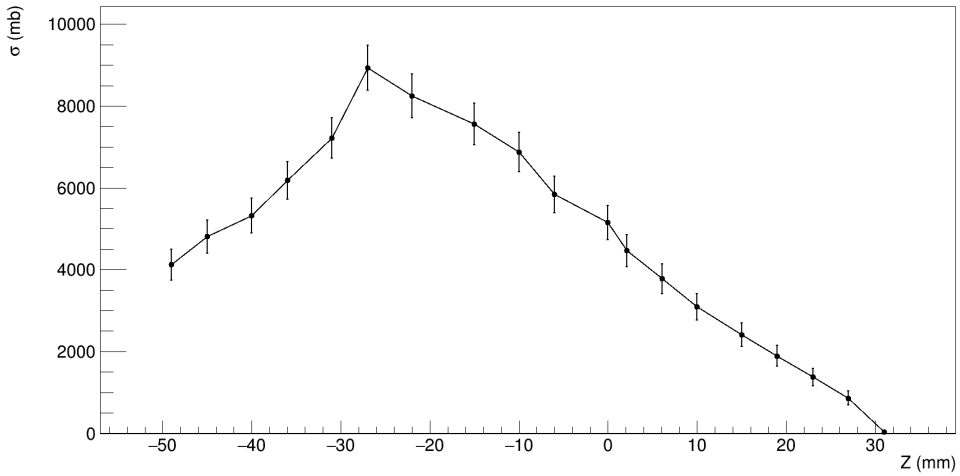

Figure 4.59: The figure shows the uncertainty of the cross section versus vertex

The measured proton yield was converted into an absolute cross section by relating the reconstructed interaction vertex to the corresponding center-of-mass energy 4.60, allowing the results to be presented as an excitation function. The extracted $\sigma(E_{\mathrm{cm}})$ distribution shows a smooth increase with energy and exhibits a maximum in the region of $E_{\mathrm{cm}} \approx 2.5$–$2.6$ MeV, followed by a gradual decrease at higher energies within the experimentally accessible range. When statistical uncertainties are included 4.61, the error bars increase in regions of low yield, as expected from Poisson counting statistics, while the overall shape of the excitation function remains unchanged. This behaviour suggests that the main features of the excitation function are stable against statistical fluctuations.

The observed correlation between the beam energy E_b and the center-of-mass energy E_{cm} is consistent with expectations for inverse kinematics, in which a $^{14}\mathrm{N}$ beam interacts with a

stationary helium target. In this case, the relation

$$E_{\mathrm{cm}} = \frac{m_t}{m_p + m_t} E_b$$

applies, leading to $E_b \approx 4.5\, E_{\mathrm{cm}}$. The physical threshold for the $^{14}\mathrm{N}(\alpha, p)^{17}\mathrm{O}$ reaction is determined by its negative Q-value ($Q \approx -1.19$ MeV), corresponding to a center-of-mass threshold energy of $E_{\mathrm{cm}}^{\mathrm{th}} \approx 1.19$ MeV. In inverse kinematics, this translates to a beam-energy threshold of approximately $E_b^{\mathrm{th}} \approx 5.36$ MeV as shown in 4.62.

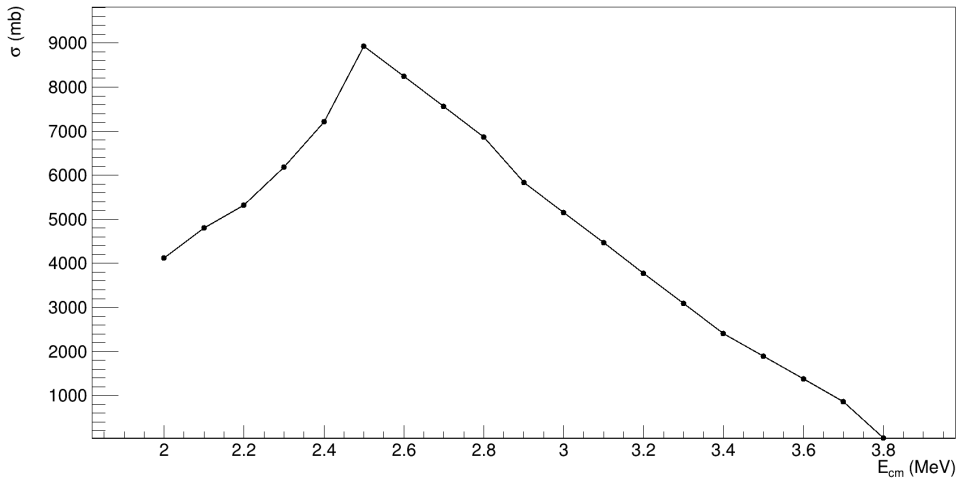

Figure 4.60: The figure shows the proton cross section as a function of centre of mass energy

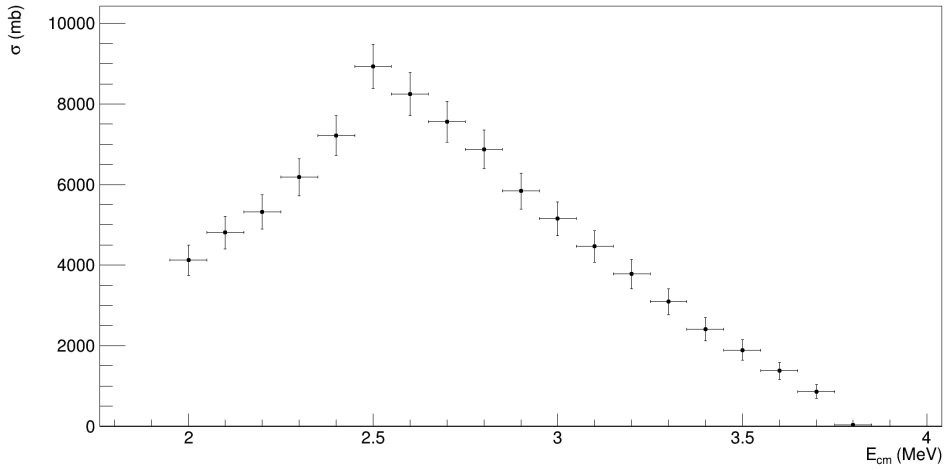

Figure 4.61: The figure shows the uncertainty of the proton cross section vs Ecm for the same cuts

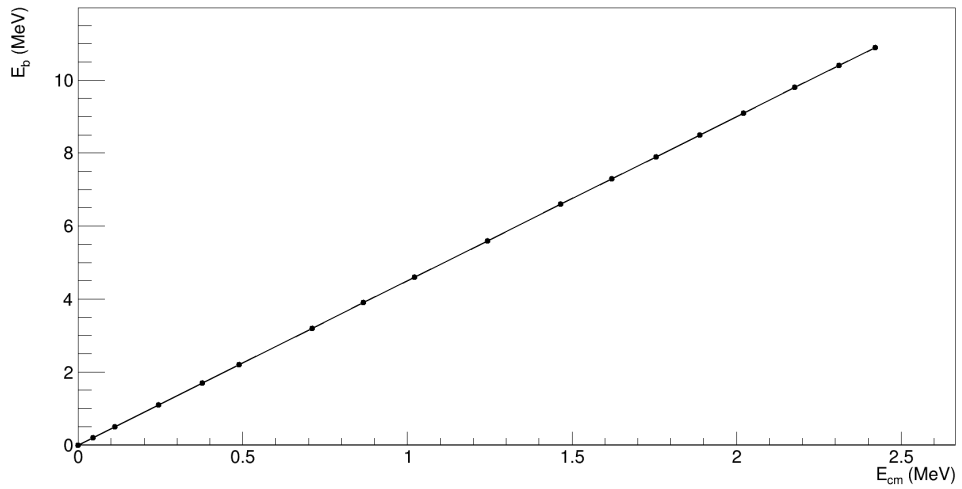

Figure 4.62: The figure shows the beam energy as a function of centre of mass energy which allow us to select the the reaction energy 1.2 MeV.

This figure 4.63 shows a clear and systematic relationship between the centre-of-mass energy and the reconstructed interaction vertex . The observed trend decrease from the gradual loss of beam energy as it passes through the gas target. The smooth and consistent behaviour supports the use of the vertex position as a reliable indicator of the reaction energy and underpins the extraction of the excitation function.

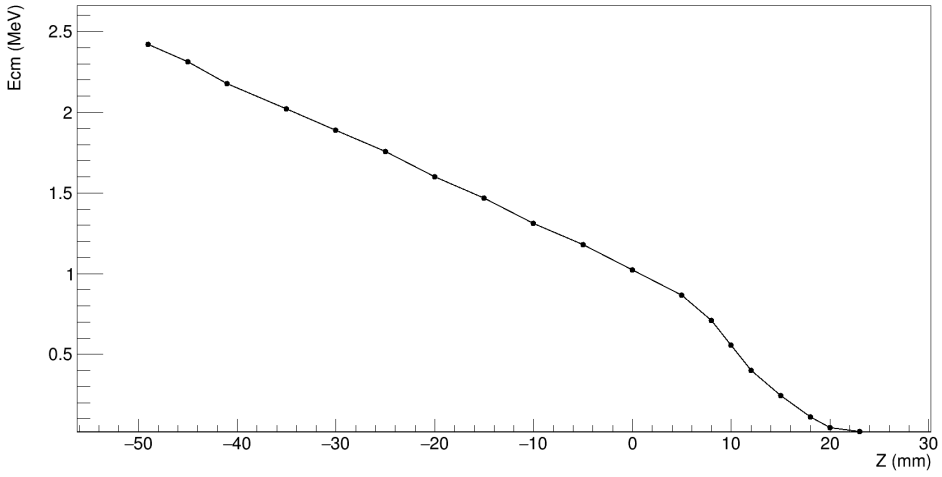

Figure 4.63: The figure shows the relation of the centre of the mass energy versus vertex with the same conditions

Chapter 5

Conclusion

This work represents the full experimental analysis for the reaction ^{14}N(α, p)^{17}O. The ^{14}N(α, p)^{17}O reaction was selected for this study because ^{14}N is a stable beam and provides an excellent test case for the TACTIC detector, particularly for investigations of alpha-induced reactions. Nuclear reactions are fundamental to understanding how stars generate energy and synthesize chemical elements. They are also important in experimental nuclear physics, where they are used to study nuclear structure, reaction mechanisms, and detector performance [37].

A stable beam of ^{14}N with energy 1 MeV/amu has been used in TACTIC helium-based gas mixtures (for 1 bar and 0.5 bar) for the runs 75 and group runs 84-91 respectively, which function as the target gas used to determine cross sections for alpha-induced reactions in TACTIC.

in this work we focused on :

1. Particle identification is performed using established methods, including analysis of the initial and final pads. Because of their energy-loss behaviour, particles deposit more energy in the final pad than in the initial pad within the detection volume. In this work, the ΔE–E technique is used to identify particles and heavier elements. An energy threshold of 50 keV is applied, and the energy resolution is obtained by normalizing the readout channels across all detector sectors.

   The stable beam analysis showed that elastic scattering at the entrance window are the main calibrated to background. Once the window position was identified, vertex-based cuts were applied to remove these events. Although this background increases the readout signals. At higher beam rates ($N_b > 10^5$ pps), however, window induced background can produce significant dead time and reduce the proton-detection efficiency.

2. The runs between 76 till 84 not been analysed for the zero dead time; stopped due to HV , and off accidentally.

3. The simulation was employed in order to get a clear particle identification between protons and alphas in TACTIC for the reaction ^{14}N(α, p)^{17}O, the cross section been calculated for both pressure (1 bar and 0.5 bar).

4. For run 75 with the main condition : -50 mm <vertex < 40 mm, 4 < multiplicity < 30, 5.5 μs $< t_{\text{trigger}} <$ 7.5 μs, it found out the results obtained under this experimental condition show that the beam energy loss in the gas target is well known and the reaction vertex is reconstructed with sufficient precision, the position of the interaction uniquely and accurately determines the centre-of-mass energy at which the reaction occurred. This

relationship allows the measured proton yield to be consistently converted into an absolute excitation function. The extracted cross section, $\sigma(E_{\mathrm{cm}})$, displays a clear dependence on energy: it rises from low values at the lowest measured energies, reaches a well-defined maximum around $E_{\mathrm{cm}} \sim 1.3$–1.5 MeV, and then decreases toward higher energies. The associated statistical uncertainties follow the expected behavior for counting statistics and do not alter the overall shape of the excitation function. Near the physical threshold of the $^{14}\mathrm{N}(\alpha, p)^{17}\mathrm{O}$ reaction ($E_{\mathrm{cm}}^{\mathrm{th}} \approx 1.19$ MeV), any non-zero cross section values observed below threshold should be treated with caution,In an extended gas target, the reaction energy depends on the position of the interaction, so the reconstructed interaction vertex is used to determine the centre-of-mass energy E_{cm}. Due to the finite vertex and energy resolution, some events may be reconstructed at energies slightly different from their true values, particularly near sharp features such as the reaction threshold. This can lead to a small apparent yield below the physical threshold, $E_{\mathrm{cm}}^{\mathrm{th}} \approx 1.2$ MeV. In the yield spectrum, these sub-threshold points correspond to only a few counts with large statistical uncertainties and are consistent with zero, indicating that they most likely arise from finite energy resolution or residual background rather than from genuine sub-threshold reaction yield.

5. The proton yield been calculated regarding to the specific cuts for both conditions for run 75 and group 84-91 with different conditions 1 bar and 0.5 respectively.

6. For group runs 84 to 91 with the specific condition : -50 mm <vertex < 40 mm, 4 < multiplicity < 30, 2.5 μs $< t_{\mathrm{trigger}} <$ 4 μs.

7. From the vertex-resolved proton yields, together with a validated mapping between the reaction vertex and the centre-of-mass energy, $E_{\mathrm{cm}}(z)$, an absolute excitation function, $\sigma(E_{\mathrm{cm}})$, was extracted for the reaction $^{14}\mathrm{N}(\alpha, p)^{17}\mathrm{O}$. The measurements cover the centre-of-mass energy range $E_{\mathrm{cm}} \approx 2.0$–$3.8$ MeV. The resulting cross section shows a pronounced maximum around $E_{\mathrm{cm}} \approx 2.5$–$2.6$ MeV, followed by a smooth decrease at higher energies. The statistical uncertainties are mainly driven by counting statistics. This is supported by the smooth behavior of the excitation function and the lack of unusually large bin-to-bin fluctuations beyond what is expected for Poisson statistics. In addition, the normalized yields show no time-dependent variations or excess scatter that would indicate detector instabilities or problems with event reconstruction. Overall, this points to stable detector operation and reliable event reconstruction throughout the measurement.

   The relation $E_b \approx 4.5\,E_{\mathrm{cm}}$ is not an independently extracted experimental result, but follows directly from the expected kinematic scaling for the present beam–target mass combination in inverse kinematics. Because the conversion from beam energy to centre-of-mass energy already assumes this relation, it cannot be used as an independent validation of the analysis. Instead, the observed proportionality serves only as a consistency check, indicating that the reconstructed energies behave as expected.

   All extracted data points lie above the physical reaction threshold at $E_{\mathrm{cm}}^{\mathrm{th}} \approx 1.2$ MeV, indicating that the observed yield originates from energetically allowed reaction processes.

   The He–CO_2 (90:10) gas mixture mainly affects the overall normalization and background contributions but does not influence the shape or interpretation of the excitation function.

8. Based on conclusions 4 and 5, different types of reaction products were identified using specific proton cuts, particularly from the (α, p) and (α, α) reaction channels. Protons and alpha particles can travel farther than heavier ions, such as ^{14}N and ^{17}O, and therefore reach the μ-RWELL detector, whereas the heavier ions are stopped in the digitizer or shielded by the cathode cage.

9. The observed yield close to the reaction threshold can be attributed to the finite energy resolution and energy straggling in the extended gas target. This behavior does not imply the presence of a physical reaction occurring below the threshold energy. To quantify the impact of energy smearing near the reaction threshold, the effective center-of-mass energy distribution was examined locally by selecting narrow vertex slices of $Z_0 \pm 3$ mm along the extended gas target. For the slice centered at $Z_0 = -27$ mm, where the mean center-of-mass energy lies close to the threshold, the ΔE_{cm} distribution of the signal component is well described by a Gaussian with a full width at half maximum of 1.44 MeV (corresponding to $\sigma = 0.61$ MeV). This width reflects the combined effects of vertex reconstruction, the finite spatial extent of the target, and energy straggling in the gas. Such an energy spread naturally leads to a non-zero reconstructed yield below the nominal threshold due to events with true energies above threshold being smeared to lower reconstructed energies. The observed yield near threshold can therefore be fully explained by experimental energy-smearing effects and does not require the presence of a physical reaction occurring below the threshold energy.

   A more comprehensive uncertainty analysis should incorporate systematic effects arising from the target density, beam normalization, proton detection efficiency, and the $E_{\mathrm{cm}}(z)$ calibration. Further background investigations, including cut-stability checks and dedicated runs to quantify contributions from the CO_2 component and from misidentified elastic-scattering events, would help to strengthen the interpretation of the results. Finally, comparisons with theoretical models, such as Breit–Wigner or *R*-matrix analyses, could link the observed excitation-function features to resonant states in ^{18}F and provide deeper insight into the underlying reaction mechanism.

Bibliography

[1] K. S. Krane. *Introductory Nuclear Physics*. Wiley, 1988.

[2] Reiner Mühle, Lukas Wacker, and Niklas Bogensperger. Rutherford scattering. Technical report, Physics Lab 3+4, ETH Zürich, 2021. Original version: Sep. 1999; Revision 1: Jan. 2007; Revision 2: Feb. 2021.

[3] G. F. Knoll. *Radiation Detection and Measurement*. Wiley, 2000.

[4] G. Charpak et al. The use of multiwire proportional counters to select and localize charged particles. *Nuclear Instruments and Methods*, 62:262, 1968.

[5] S. Chakraborty et al. Performance study of novel micro-resistive well (μ-rwell) detector in different gas mixtures. *Journal of Instrumentation*, 18:C06006, 2023.

[6] TUDA. Technical university of darmstadt (tu darmstadt). Available at https://www.tuda.de. Accessed: 27 July 2023.

[7] Root Simulation. Courses. *ROOT Documentation*, 2024.

[8] L. martin. *TACTIC: The TRIUMF Annular Chamber for Tracking and Identification of Charged Particles*. Phd thesis, University og York, 2015.

[9] CERN. Garfield++: Simulation of gaseous detectors. `https://garfieldpp.web.cern.ch/garfieldpp/`, 2025. Accessed: 2025-10-04.

[10] Garfield website.

[11] T. Mayer-Kuckuk. *Kernphysik*. Vieweg+Teubner Verlag, Wiesbaden, 1992.

[12] L. C. Feldman and J. W. Mayer. *Fundamentals of Surface and Thin Film Analysis*. North-Holland, New York, 1986.

[13] T. Rauscher. Astrophysical reaction rates as a challenge for nuclear reaction theory. *International Journal of Modern Physics E*, 20:1071–1169, 2011.

[14] C. Iliadis. *Nuclear Physics of Stars*. Wiley-VCH, 2007.

[15] Claus E. Rolfs and William S. Rodney. *Cauldrons in the Cosmos*. University of Chicago Press, Chicago, 1986.

[16] T. Rauscher. Astrophysical reaction rates and nuclear physics. *Physical Review C*, 81:045807, 2010.

[17] H. Utsunomiya, P. Mohr, A. Zilges, and M. Rayet. Photon strength functions and nuclear astrophysics. *Nuclear Physics A*, 777:459–481, 2006.

[18] T. Rauscher and Friedrich-Karl Thielemann. Astrophysical reaction rates from statistical model calculations. *Atomic Data and Nuclear Data Tables*, 75:1–351, 2000.

[19] E. Rutherford and H. Geiger. *Proceedings of the Royal Society of London A*, 81:141, 1908.

[20] J. Hilke and W. Riegler. Gaseous detectors. In C. W. Fabjan and H. Schopper, editors, *Particle Detection with Drift Chambers*, chapter X. Springer, 2020.

[21] H. Geiger and W. Mueller. *Physikalische Zeitschrift*, 29:839, 1928.

[22] T. Bressani, G. Charpak, D. Rahm, and C. Zupancic. Track localization by means of a drift chamber. In *Proc. Int. Seminar Filmless Spark and Streamer Chambers*, page 275, Dubna, USSR, 1969.

[23] A.H. Walenta, J. Heintze, and B. Schürlein. The multiwire drift chamber – a novel type of proportional wire chamber. *Nuclear Instruments and Methods*, 92:373, 1971.

[24] Garfield++. Garfield++ simulation toolkit for gaseous detectors. Available at https://garfieldpp.web.cern.ch. Accessed: 30 November 2023.

[25] Magboltz website. Magboltz. `http://magboltz.web.cern.ch/`. Accessed: 30/11/2023.

[26] W. H. Bragg and R. Kleeman. On the α particles of radium, and their loss of range in passing through various atoms and molecules. *The London, Edinburgh, and Dublin Philosophical Magazine and Journal of Science*, 10:318–340, 1905.

[27] J. F. Ziegler and J. F. Manoyan. The stopping of ions in compounds. *Nuclear Instruments and Methods B*, 35:215, 1988.

[28] TACTIC. Tactic — triumf annular chamber for tracking and identification of charged particles. Available at https://tactic.triumf.ca. Accessed: 30 November 2023.

[29] W. Blum, W. Riegler, and L. Rolandi. *Particle Detection with Drift Chambers*. Springer-Verlag, 2 edition, 2008.

[30] TRIUMF. About triumf. `https://triumf.ca/about/`, 2026. Accessed: 2026-01-30.

[31] TRIUMF. Triumf — canada's particle accelerator centre. Available at https://www.triumf.ca. Accessed: 30 November 2023.

[32] S. Engel et al. Development of detection systems for low-energy heavy ions at dragon. *Nuclear Physics A*, 701, 2002.

[33] L. Martin, G. Ruprecht, U. Hager, P.-A. Amaudruz, L. Buchmann, S. P. Fox, A. M. Laird, and E. Martin. Tactic: The triumf annular chamber for tracking and identification of charged particles. *Nuclear Instruments and Methods in Physics Research Section A*, 386:547–554, 1997.

[34] K. Jayamanna et al. Off-line ion source terminal for isac at triumf. *Review of Scientific Instruments*, 79, 2008.

[35] P. Mumby-Croft. *TACTIC: A New Detector for Nuclear Astrophysics*. Phd thesis, TRIUMF, 2009.

[36] A. Georgiev et al. An analog-to-digital conversion based on a moving window deconvolution. *IEEE Transactions on Nuclear Science*, 41, 1994.

[37] K. Langanke and M. Wiescher. Nuclear reactions and stellar processes. *Reports on Progress in Physics*, 64(12):1657–1701, 2001.